2022-06

COMPUTATIONAL MULTICOPTER MODELING AND DESIGN

Ceroli, Zachary A.

Monterey, CA; Naval Postgraduate School

NAVAL POSTGRADUATE SCHOOL

MONTEREY, CALIFORNIA

THESIS

COMPUTATIONAL MULTICOPTER MODELING AND DESIGN

by

Zachary A. Ceroli

June 2022

Thesis Advisor: Anthony J. Gannon
Co-Advisors: Kevin D. Jones
Christopher S. Clay

THIS PAGE INTENTIONALLY LEFT BLANK

REPORT DOCUMENTATION PAGE			*Form Approved OMB No. 0704-0188*

1. AGENCY USE ONLY *(Leave blank)*	**2. REPORT DATE** June 2022	**3. REPORT TYPE AND DATES COVERED** Master's thesis

4. TITLE AND SUBTITLE
COMPUTATIONAL MULTICOPTER MODELING AND DESIGN

5. FUNDING NUMBERS
RMQ80

6. AUTHOR(S) Zachary A. Ceroli

7. PERFORMING ORGANIZATION NAME(S) AND ADDRESS(ES)
Naval Postgraduate School
Monterey, CA 93943-5000

8. PERFORMING ORGANIZATION REPORT NUMBER

9. SPONSORING / MONITORING AGENCY NAME(S) AND ADDRESS(ES)
Office of Naval Research, Arlington, VA 22217

10. SPONSORING / MONITORING AGENCY REPORT NUMBER

11. SUPPLEMENTARY NOTES The views expressed in this thesis are those of the author and do not reflect the official policy or position of the Department of Defense or the U.S. Government.

12a. DISTRIBUTION / AVAILABILITY STATEMENT
Approved for public release. Distribution is unlimited.

12b. DISTRIBUTION CODE
A

13. ABSTRACT (maximum 200 words)

This thesis utilizes a modified version of Axial Momentum Theory (AMT) and computational fluid dynamics (CFD) to model multiple propellers with similar, simplified flows for estimates of aerodynamic constant force on small unmanned aerial vehicles (UAVs). Utilizing the modified version of AMT, a comparison of a commercial-off-the-shelf (COTS) vertical take-off and landing (VTOL) platform and a new design optimized for forward flight is conducted.

14. SUBJECT TERMS
hydrogen, flight, unmanned, fuel cell, aerial, vehicle, drone, design, intelligence, surveillance, reconnaissance, Axial Momentum Theory, AMT, computational fluid dynamics, CFD, unmanned aerial vehicles, UAV, commercial-off-the-shelf, COTS, vertical take-off and landing, VTOL

15. NUMBER OF PAGES
147

16. PRICE CODE

17. SECURITY CLASSIFICATION OF REPORT	**18. SECURITY CLASSIFICATION OF THIS PAGE**	**19. SECURITY CLASSIFICATION OF ABSTRACT**	**20. LIMITATION OF ABSTRACT**
Unclassified	Unclassified	Unclassified	UU

NSN 7540-01-280-5500

Standard Form 298 (Rev. 2-89)
Prescribed by ANSI Std. 239-18

THIS PAGE INTENTIONALLY LEFT BLANK

Approved for public release. Distribution is unlimited.

COMPUTATIONAL MULTICOPTER MODELING AND DESIGN

Zachary A. Ceroli
Lieutenant, United States Navy
BS, United States Naval Academy, 2016

Submitted in partial fulfillment of the
requirements for the degree of

MASTER OF SCIENCE IN MECHANICAL ENGINEERING

from the

NAVAL POSTGRADUATE SCHOOL
June 2022

Approved by: Anthony J. Gannon
Advisor

Kevin D. Jones
Co-Advisor

Christopher S. Clay
Co-Advisor

Garth V. Hobson
Chair, Department of Mechanical and Aerospace Engineering

THIS PAGE INTENTIONALLY LEFT BLANK

ABSTRACT

This thesis utilizes a modified version of Axial Momentum Theory (AMT) and computational fluid dynamics (CFD) to model multiple propellers with similar, simplified flows for estimates of aerodynamic constant force on small unmanned aerial vehicles (UAVs). Utilizing the modified version of AMT, a comparison of a commercial-off-the-shelf (COTS) vertical take-off and landing (VTOL) platform and a new design optimized for forward flight is conducted.

THIS PAGE INTENTIONALLY LEFT BLANK

TABLE OF CONTENTS

LIST OF FIGURES

THIS PAGE INTENTIONALLY LEFT BLANK

LIST OF TABLES

THIS PAGE INTENTIONALLY LEFT BLANK

LIST OF ACRONYMS AND ABBREVIATIONS

AMT	axial momentum theory
CAD	computer aided design
C5ISR	command, control, communication, computer, cyber, intelligence, surveillance, and reconnaissance
CFD	computational fluid dynamics
COTS	commercial off-the-shelf
DOD	Department of Defense
MTOW	maximum take-off weight
NACA	National Advisory Committee for Aeronautics
UAV	unmanned aerial vehicle
USV	unmanned surface vessel
UUV	unmanned underwater vehicle
VTOL	vertical take-off and landing

THIS PAGE INTENTIONALLY LEFT BLANK

ACKNOWLEDGMENTS

I would like to thank my thesis advisors, Dr. Anthony Gannon, Dr. Kevin Jones, and RA Christopher Clay, for the continual support, troubleshooting, and review. Without their knowledge and input, this thesis would not have had any success.

I would also like to thank Dr. Hobson and CDR Arledge for their assistance and input throughout my compressed time at the Naval Postgraduate School. As considerate and patient sounding boards, they provided continual guidance and direction.

I would also like to thank my father, mother, and sister for their motivation and helping hands. As the last member of my immediate family to write a thesis, their insights into the upcoming struggles and challenges made the road smoother than it otherwise would have been.

Finally, as a Christian, I'd like to thank the Lord.

THIS PAGE INTENTIONALLY LEFT BLANK

I. INTRODUCTION

A. OBJECTIVE

This thesis utilizes a modified version of Axial Momentum Theory (AMT) and computational fluid dynamics (CFD) to model multiple propellers with similar, simplified flows to estimate aerodynamic and gravitational forces on a commercial-off-the-shelf (COTS) vertical take-off and landing (VTOL) platform. Utilizing the modified version of AMT, a comparison of a COTS platform and a new design optimized for forward flight is conducted to investigate potential improvements in VTOL craft.

B. ENERGY SOURCE

The Department of Defense (DOD) has interest in developing and deploying energy solutions in locations where military forces operate instead of transporting fuel long distances [1]. Producing hydrogen locally using a mobile means could result in safer missions and reform energy supply chains [1]. Because of hydrogen's high heat of combustion and high specific heat, it is a favorable alternative to conventional aircraft fuels [2].

Compared to conventional fossil fuels, "hydrogen has significantly lower volumetric density, but more than double the gravimetric density" [3]. In Sarkar and Banerjee's analysis on hydrogen storage options, they concluded that hydrogen "seems to be the most favorable for long term viability" and "the total energy required for [the] compressed option is the lowest" [3]. Compressing hydrogen increases its volumetric energy density, making it a viable option for immediate use in fuel cells or turbines [3]. Hydrogen has the potential to be properly harnessed in an efficient and cost-effective way, making the possibilities for renewable energy infinite through hydrolysis [4].

A small scale, reliable hydrogen station aboard ship or deployed coupled with persistent unmanned command, control, communications, computer, cyber, intelligence, surveillance, and reconnaissance (C5ISR) assets powered by locally produced hydrogen could meet the demand for self-sustaining and highly mobile assets worldwide [5]. Because hydrogen can be made from water using any available electrical energy source, it can be

produced locally almost anywhere in the world [2]. A clean, sustainable, and mobile method of producing hydrogen is electrolysis of water [3]. If seawater was utilized, every naval vessel could produce the compressed hydrogen needed for unmanned aerial vehicles (UAVs), unmanned surface vessels (USVs), or unmanned underwater vehicles (UUVs). This energy independent naval force would reform supply lines currently needed and increase on-station time for assets in theater.

C. COMMERCIAL PLATFORMS

Multi-copters, like quadcopters, are becoming more relevant platforms for use in military applications. Modeling these platforms in a computationally cheap method has proved to be a challenge due to the multi-propeller design. The COTS platform chosen combines a composite-based material structure with compressed hydrogen storage and fuel cell technology. Companies like Intelligent Energy and HES Energy Systems have demonstrated their fuel cell UAVs could outperform battery only units in endurance [5]. When operating hydrogen fuel cells, the only by-products are electrical energy, heat, and water vapor.

The Naval Postgraduate School acquired a COTS platform from HES Energy Systems named the 'Hycopter' [6]. This hydrogen fuel cell powered system has the following flight characteristics [7]:

- Flight time of 3+ hours with a twelve-liter hydrogen tank pressurized to 34.5 MPa (5000 psi) and no payload
- Maximum advertised payload of 2.5 kg
- Maximum take-off weight (MTOW) of 16.5 kg

According to promotional material, "Hycopter drones can cover 6 times more surface area than most of today's battery drones, making large-scale inspections faster, cheaper, and easier to complete" [7]. In a man overboard or maritime search and rescue scenario, this increased endurance could locate the target and bridge the time needed to deploy manned aircraft for recovery. Figure 1 shows the COTS platform with commercially available attachments.

Figure 1. Hycopter with HES Available Attachments. Source: [7].

"Designed for quiet long endurance (LE) multi-rotor flight, reliability, and high performance," the possible military applications of this craft include C5ISR or search and rescue (SAR) missions in conjunction with or instead of manned aircraft operations [7]. The advertised payload capacity of 2.5 kg limits the possibilities of weaponizing the platform for combat operations or for extraction of injured or trapped personnel [7].

The COTS platform of this study is a VTOL vehicle that is easily deployable by a two-person team in ten minutes and is representative of current technology [7]. The COTS platform's design flight characteristics include a maximum lateral speed of 15.6 m/s, maximum assent speed of 3 m/s, and maximum tilt angle of 32 deg [7]. Sparse data provided by Yang for the Aqua-Quad suggests a linear relationship between angle of attack and true airspeeds [8]. Figure 2 shows the data for the Aqua-Quad.

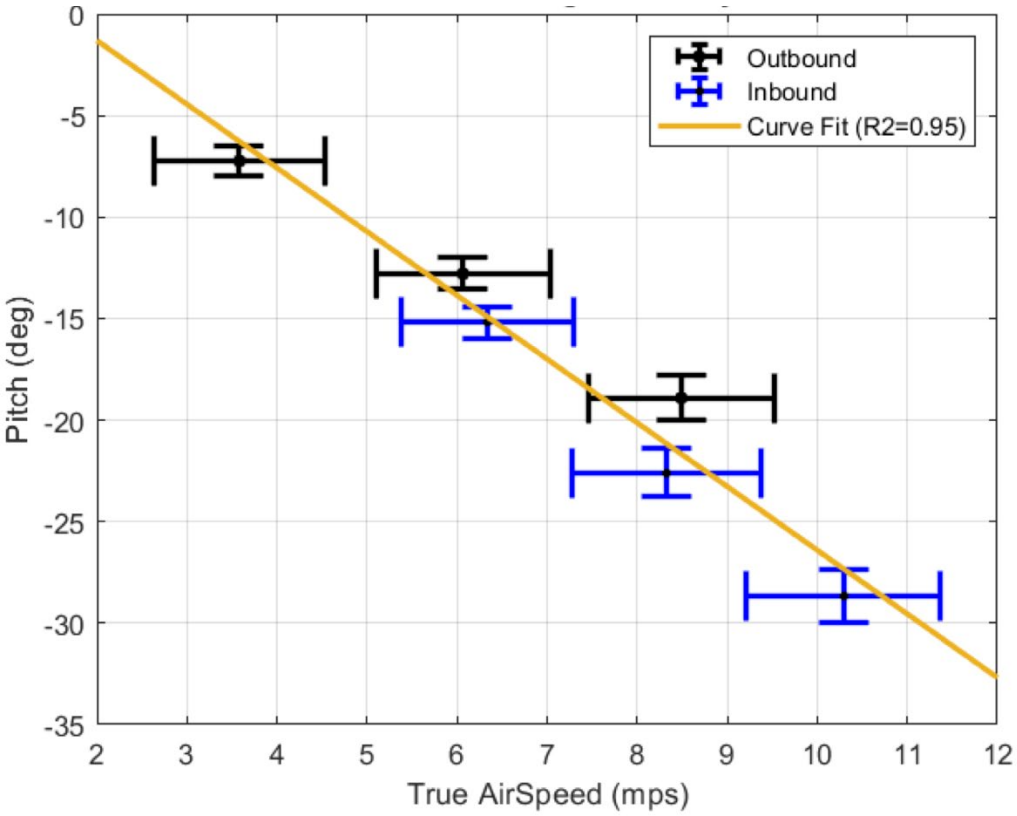

Figure 2. Aqua-Quad True Airspeed versus Platform Pitch. Source: [8].

D. THRUST CONVERSION

The COTS hydrogen platform has significant advantages over battery powered aircraft of a similar size but is limited in flight envelop due to the platform's focus on hover flight. "To achieve a goal of minimum weight, VTOL aircraft design should be optimized for forward flight" [9]. "There are four technologies for converting the system from the vertical thrusting mode to the horizontal cruising flight mode: tilting aircraft, tilting thrust,

thrust vectoring, and separate (dual) thrust" [10-12]. Conceptually, these technologies could allow aircraft to go twice as far and twice as fast as a comparable sized helicopter on the same amount of fuel [13]. For example, the flight envelop of the V-22 Osprey surpasses that of a helicopter and most of that of a turboprop aircraft [13].

The focus on hover flight limits multi-copters in a similar manner to helicopters and other VTOL platforms. Since multi-copters are typically unmanned, there is no design requirement for a cockpit that can carry cargo or personnel like the V-22 Osprey. The design proposal will be a tilting aircraft which significantly reduces craft complexity but maintains similar advantages seen by the V-22. The one advantage of the V-22 over the current COTS hydrogen platform is that the V-22 has variable pitch propellers. The variable pitch propellers allow for efficient flight over all flight modes. Figure 3 shows the Flying Wing proposal in a take-off configuration.

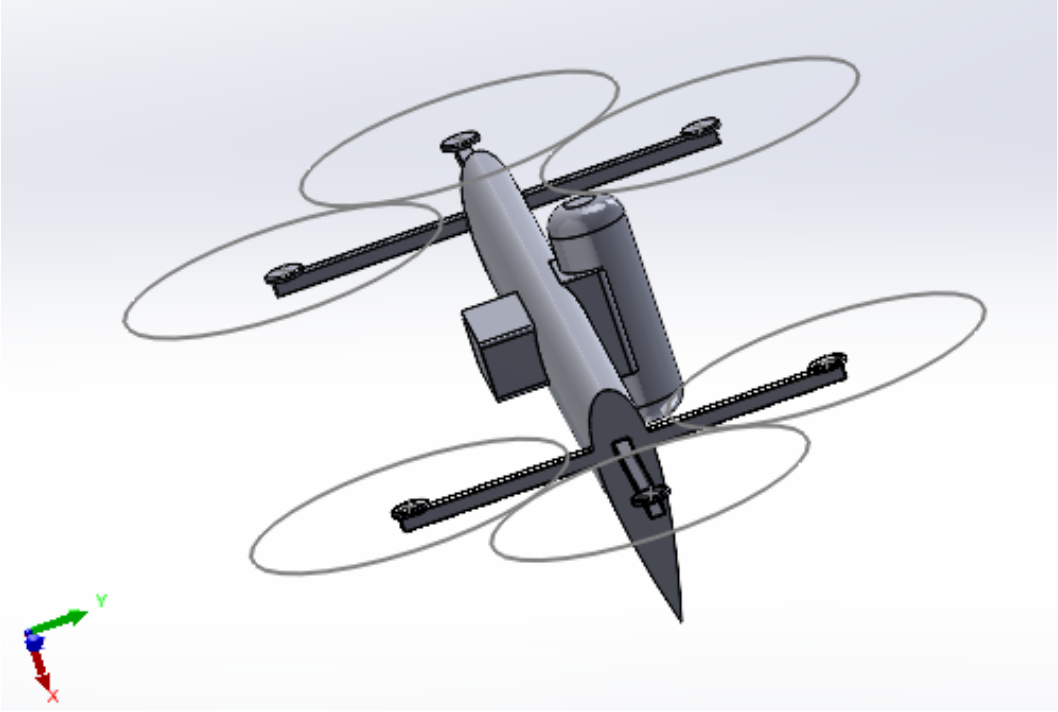

Figure 3. Bluff Body Flying Wing Proposal Take-Off Configuration

"Aircraft range depends on factors such as airspeed, fuel capacity, load, hover requirements, and take-off/landing configurations" [13]. Conventional aircraft have values of thrust at take-off that are thirty to forty percent of the total weight being lifted [11]. For VTOL aircraft, the thrust-to-weight ratio in the vertical lifting mode must exceed the operating weight by some margin [14]. Figure 4 shows the advantages of the V-22 flight envelope compared to traditional aircraft.

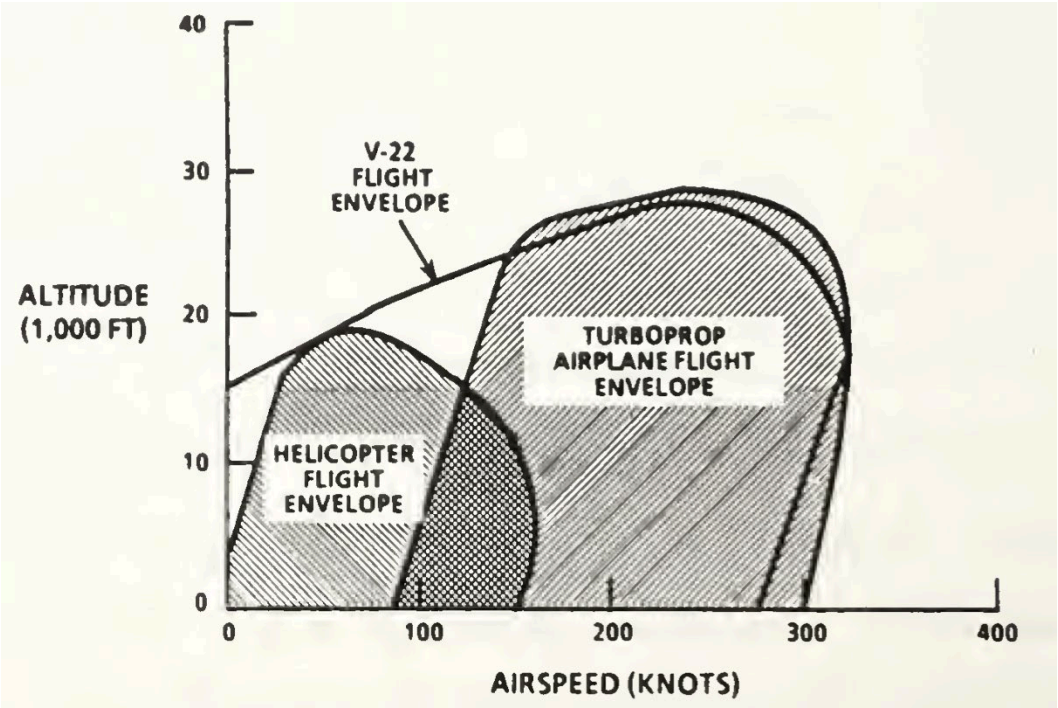

Figure 4. V-22 versus Helicopter/Turboprop Flight Envelopes. Source: [13].

In cruise flight, manned helicopter and rotary type VTOL aircraft have poorer efficiency than ducted fans or turbofans and turbojets [12]. The endurance and range advantages of conventional flight make transitioning from rotary flight to fixed wing flight highly desirable. Maintaining the rotary wing aircraft configuration limits speed due to the development of shockwaves on the advancing blades with stall conditions on the retreating blades [15]. These transonic problems severely limit top speeds of manned rotary wing platforms; however, rotary wing aircraft are faster in maneuvers requiring quick lateral movements and rapid hover-up/hover-down procedures [15]. Some of these limits may not

be as significant for smaller unmanned platforms. Figure 5 shows the benefits of the V-22 in terms of fuel economy compared to conventional aircraft.

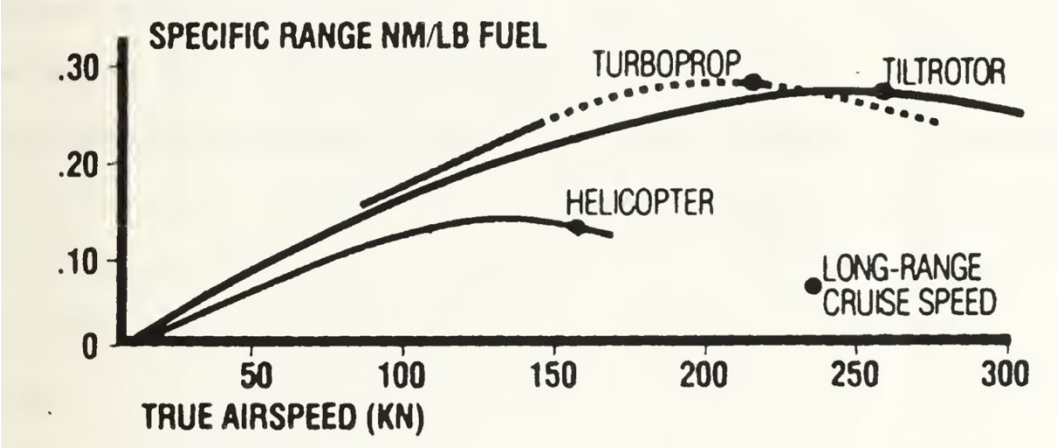

Figure 5. Specific Range (NM/LB Fuel) to True Airspeed. Source: [13].

E. CHAPTER OUTLINE

Chapter I discusses fuel selection considerations, introduces a current commercially available drone, and discusses thrust conversion technologies.

Chapter II discusses AMT and the creation of polynomial velocity distributions.

Chapter III discusses AMT application to a disk in free space, its use in CFD modeling, and the results of modeling a disc in free space.

Chapter IV discusses basic aerodynamic features of the COTS platform, the design features and methods used to create the Flying Wing proposal, the CFD modeling of the crafts, and the results of CFD modeling.

Chapter V summarizes the results and discussions in a conclusion.

Chapter VI provides ideas for future work.

THIS PAGE INTENTIONALLY LEFT BLANK

II. AXIAL MOMENTUM THEORY AND MODIFICATIONS

A. MOTIVATION

AMT models the unsteady flow of a rotating propeller with a steady flow through a disk with a step change in pressure as the flow passes through the disk. For hover and vertical flight, a balance of forces was applied augmenting weight by body drag. For forward flight a balance of forces was applied in the direction of thrust but was not sought for in direction perpendicular to thrust resulting in non-equilibrium solutions for some cases. The cost of achieving full equilibrium is high and left for future work.

The hypothesis is that induced flows from a propeller changes the exerted aerodynamic forces on the craft's body. Modeling propeller flows in addition to external flows could provide better estimates of aerodynamic forces seen by the craft in various stages of flight. Combining the force balance with a steady flow AMT model significantly reduces the computational cost of modeling these flows.

B. THEORY

AMT provides one solution to simplify the modeling of propeller fluid flows by compressing the propeller into an infinitely thin disk [16]. The infinitely thin disk assumes the propeller has an infinite number of blades [16]. The creation of a disk using computer aided design (CAD) software provides a location for an induced velocity to be applied to the fluid in place of a rotating propeller. AMT provides a first estimate of the wake-induced flow by using the integral form of the five fluid flow equations [16].

$$p + \frac{1}{2}\rho v^2 + \rho g = constant \tag{1}$$

Low speed flows are generally defined as speeds less than thirty percent of the sonic velocity and are governed by Bernoulli's equation, shown in Equation 1. In Bernoulli's equation p is the pressure, ρ is the fluid density, v is the fluid velocity, and g is gravitational acceleration [17]. Figure 6 shows the fluid stream tube for vertical flight.

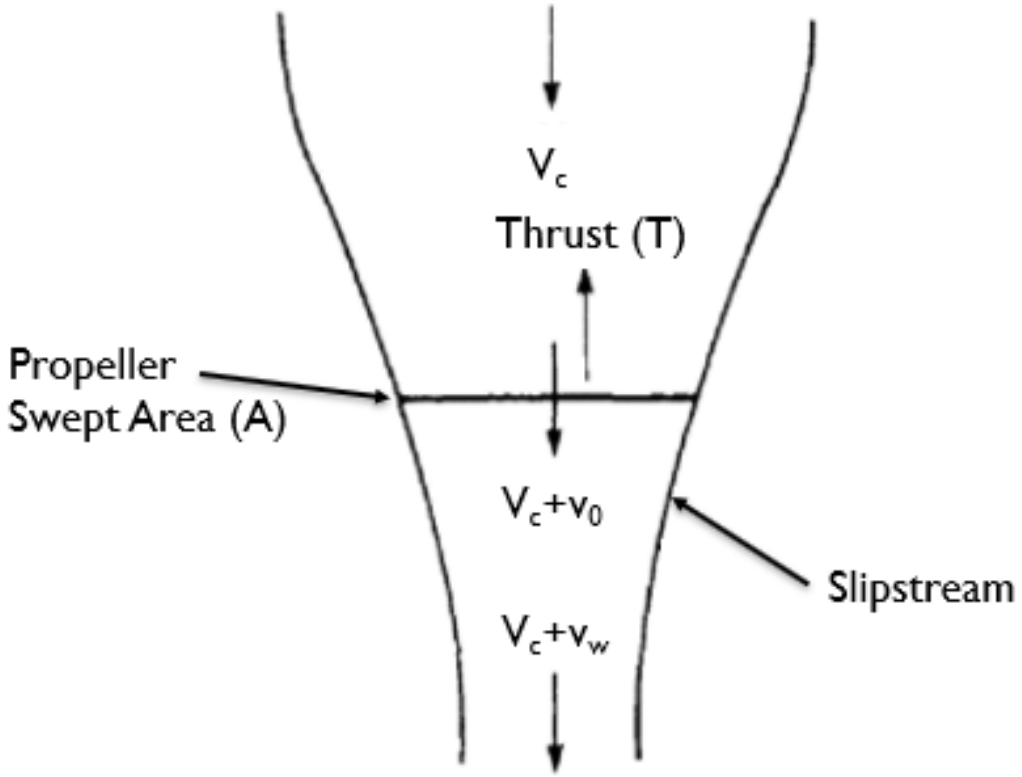

Figure 6. Vertical and Hover Flight Flow Model After. Source: [16].

In Figure 6, v_w is the wake velocity which is $2 * v_0$. Hover flight is a simplification of vertical climb where $V_c = 0$. AMT utilizes the average velocity increase across the disk without any knowledge of the distribution [16]. Utilizing this average, an axial hover velocity, v_h, can be defined where T is the specified thrust from the propeller, ρ is the fluid density, and A is the disk area [16]. The hover velocity is the average velocity across the surface of the disk needed to achieve the appropriate volumetric flow rate through the disk. The disk area is equivalent to the swept area of the replaced propeller. The relationship between the hover velocity and its real-world parameters is shown in Equation 2.

$$v_h = \sqrt{\frac{T}{2\rho A}} \tag{2}$$

When in vertical climbing flight, the hover velocity is part of the induced velocity, v_0, shown in Equation 3. Solving the axial momentum equation for the flow field requires the incoming flow velocity to be considered [16]. From Equation 1, pressure is related to

velocity squared, thus the solution for the induced velocity comes in the form of the quadratic equation [16]. The negative solution to the quadratic equation is ignored since a negative velocity is not applicable in climbing flight.

$$v_0 = \frac{-V_c}{2} + \sqrt{\frac{{V_c}^2}{4} + {v_h}^2} \tag{3}$$

From Equation 3, when $V_c = 0$, $v_0 = v_h$. Obtaining the hover velocity when $V_c = 0$, shows the equation has the right bounds [16]. For forward flight, flow enters the disk axially and tangentially. For analysis, the incoming velocity is broken into its axial and tangential components using the Actuator Disk angle of attack (AoA), $\propto$ [16]. Figure 7 shows the forward flight fluid stream tube.

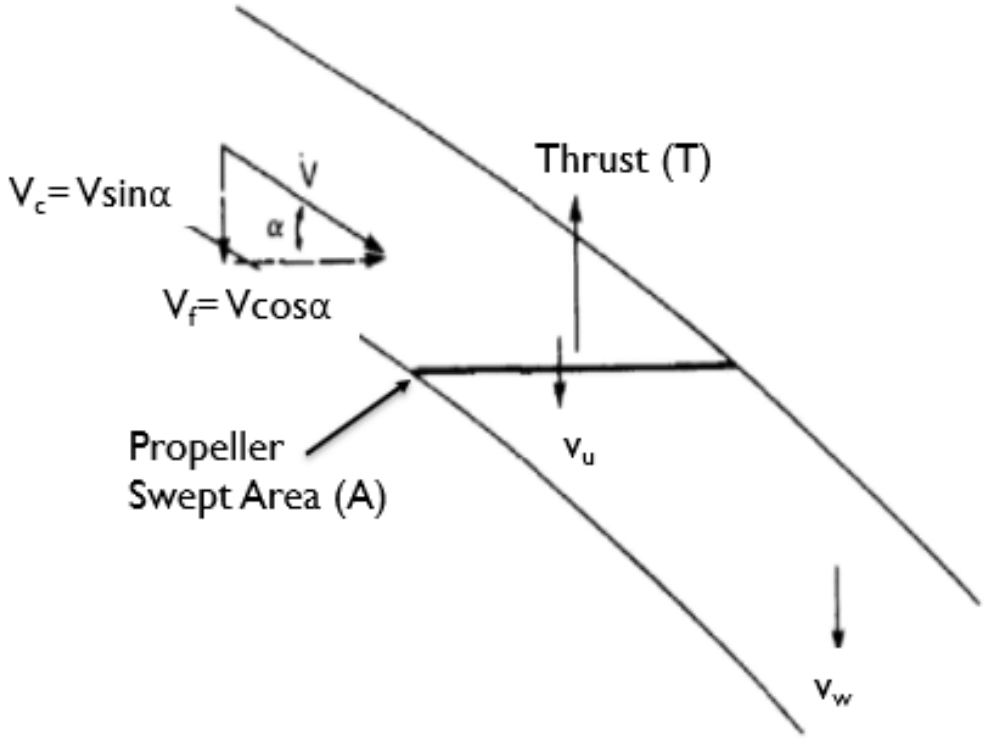

Figure 7. Forward Flight Flow Model After. Source: [16].

For this stage of flight, the components of the incoming velocity, V, were broken up into the velocity component normal to the disk, V_c, and the velocity component tangent with the disk, V_f.

$$V_c = V * sin(\alpha) \tag{4}$$

$$V_f = V * cos(\alpha) \tag{5}$$

Once the components are defined, the full solution to the induced velocity in forward flight, v_u, is defined and shown in Equation 6 [18].

$$v_u = \frac{{v_h}^2}{\sqrt{{V_f}^2 + (V_c + v_o)^2}} \tag{6}$$

The velocity specified by v_u is an average uniform induced velocity needed across the entire disk to achieve the correct volumetric flow rate through the disk. Once again when $V = 0$, $v_u = v_h$, indicating the equation has the right bounds [16]. When in vertical or forward flight, the aerodynamic and gravitational forces acting on the craft are accounted for in the desired thrust calculations.

C. CREATION OF THE VARIABLE AXIAL VELOCITY DISTRIBUTION

The first modification to AMT was to create an axial velocity distribution as a function of radius using a 4th degree polynomial. The initial axial velocity profile was a guess that was adjusted to match thrust. The general form of the function is shown in Equation 7.

$$V_a(r) = C1 + C2 * r + C3 * r^2 + C4 * r^3 + C5 * r^4 \tag{7}$$

Velocity was non-dimensionalized by dividing the velocity profile by the peak axial velocity, V_p. Peak radius, R_p, is the fraction of the outer radius of the disk, R_o, where the peak axial velocity is located. Radius was non-dimensionalized by dividing all radial positions by R_o.

The boundary conditions chosen for the non-dimensionalized axial velocity polynomial were 0 at the disk center, 0 at the disk edge, a peak velocity, V_p, of 1 at the radial position of peak velocity, R_p, 0 slope at the disk center, and 0 slope at the radial position of maximum velocity.

The 0 conditions at the tip and center of the disk were chosen to ensure no axial velocity was induced at the center or disk edge locations. In addition, the 0 condition at the disk edge ensures the disk edge pressure matches ambient pressure through Bernoulli's equation and no pressure discontinuity at the tip exists. The non-dimensionalization by peak velocity results in a maximum velocity of 1. This allows for easy scaling to any disk loading and radius.

The first derivative of Equation 7 was utilized to enforce local minima and maxima. The 0-slope condition at the position of maximum velocity is to ensure the velocity is a local limit. The 0-slope condition at the disk center was chosen to ensure the center of the disk was a smooth curve in three-dimensional space and to extend the relatively flat portion of the curve further out over the motor.

The mathematical representations of the initial boundary conditions applied are shown below:

$$V_a(0) = 0$$
$$V_a'(0) = 0$$
$$V_a(R_p) = 1$$
$$V_a'(R_p) = 0$$
$$V_a(R_o) = 0$$

The constants were solved for symbolically, and the resulting polynomial velocity profile plotted using MATLAB. The code used to generate the constants and graph the resulting polynomial is included in the Appendix A. All the constants, distribution, and scaling were implemented using expression language in Ansys CFX. The expressions, expert parameters, and monitor points used are included in Appendix B.

Axial Velocity profile data derived from CFD simulations of the propeller utilized by the COTS platform was provided by Richmond for comparison [19]. Richmond's data was utilized to create two additional polynomials for future modeling. The first fit maintained the 4th degree polynomial but changed the slope at the center of the disk to a non-zero value and moved the peak radius to match the data. The non-zero value for the slope at the center of the disk does not appear to match the data at the disk center but

maintains the same number of needed boundary conditions by maintaining polynomial degree.

To better approximate Richmond's data and maintain the original boundary conditions, a 5th degree polynomial was created to fit the data. The extra degree of freedom was utilized to capture the concavity shift displayed near the disk center by defining the radius at the inflection point, R_i, and setting the value of the second derivative of Equation 7 to 0. Figure 8 shows all axial velocity polynomials generated over Richmond's data. The mathematical representation of the additional boundary condition is displayed below:

$$V_a''(R_i) = 0$$

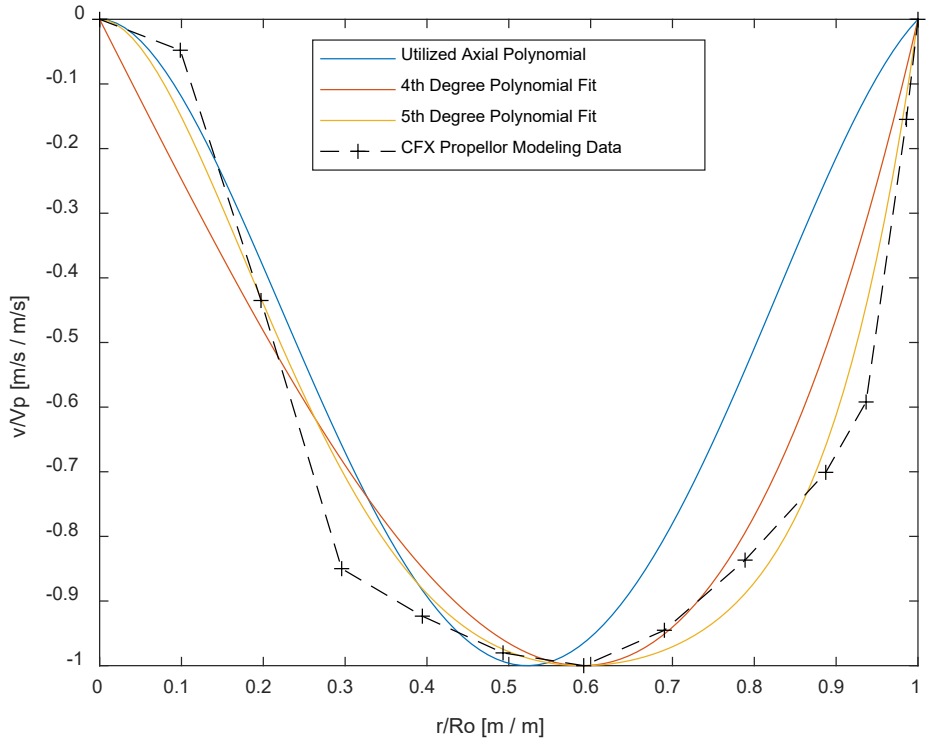

Figure 8. Axial Polynomial Distributions versus Propeller Modeling Data. Source: [19].

The blue polynomial shown is the one utilized for all modeling in this study. From Figure 8, the blue polynomial does not model the fuller shape of the blade loading predicted

by Richmond and results in higher peak velocities needed to achieve the same thrust. The better profiles provided by the two additional polynomials generated should reduce peak velocities by better matching the blade loading but are left for future studies.

D. CREATION OF THE VARIABLE RADIAL VELOCITY DISTRIBUTION

The second modification to AMT was to create a radial velocity distribution to generate the necessary stream tube contraction at the disk. The same polynomial distribution used for axial velocity was used for radial velocity with a non-dimensionalized linear modification. The equation used for the radial velocity is shown in Equation 8.

$$V_r(r) = V_a(r) * \frac{r}{R_o} \tag{8}$$

In Equation 8, Equation 7 is multiplied by a ratio where r is the radial distance from the center of the disk, and R_o is the outer radius of the disk. In effect, the polynomial proportionally spreads the compression created by the tip vortex over the entire area of the disk. Figure 9 shows the applied radial velocity polynomial.

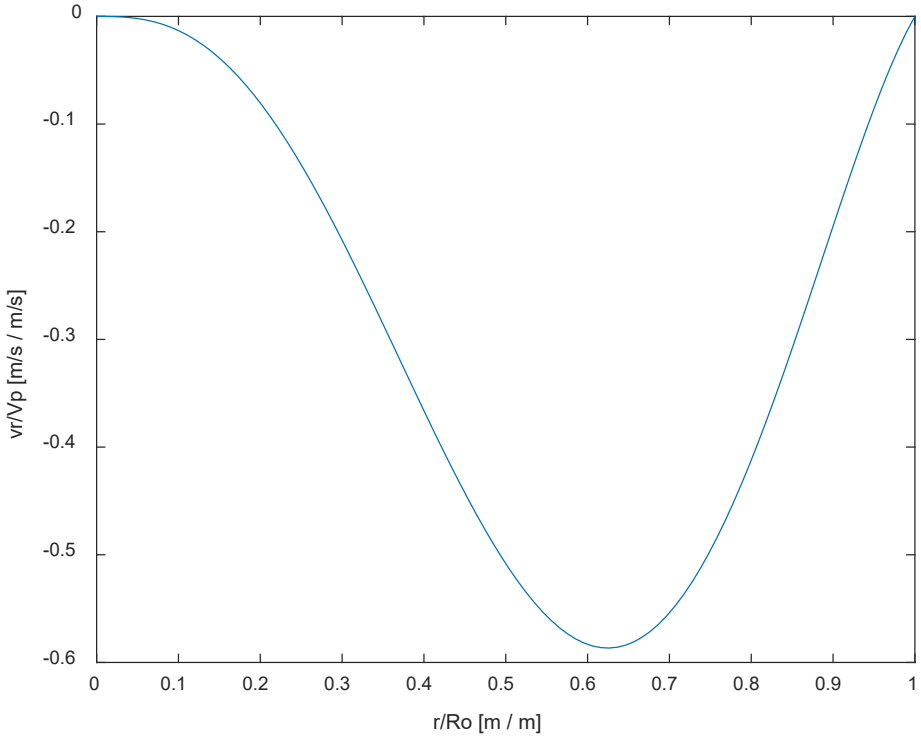

Figure 9. Applied Radial Polynomial Distribution

III. ACTUATOR DISK CFD METHODS AND APPLICATION

A. FLUID DOMAIN CREATION

The first fluid domain modeled was an Actuator Disk in free space. All fluid domains for this thesis were created in SolidWorks and imported into Ansys CFX. Figure 10 shows the fluid domain utilized for an actuator disk in free space. The diameter of the disk is equal to the diameter of the replaced propeller at 0.71 m ensuring the same swept area between the propeller and the disk. In Figure 10, the upper surface of the cylindrical fluid domain is the actuator disk which is immersed in a much larger fluid domain to simulate an actuator disk in free space. The cylindrical fluid domain below the disk extends 3 m to ensure there was a region of fluid for mesh refinement at least 3 diameters below the disk. The whole domain was large enough to ensure all boundaries are at least 10 disk diameters away from the Actuator Disk.

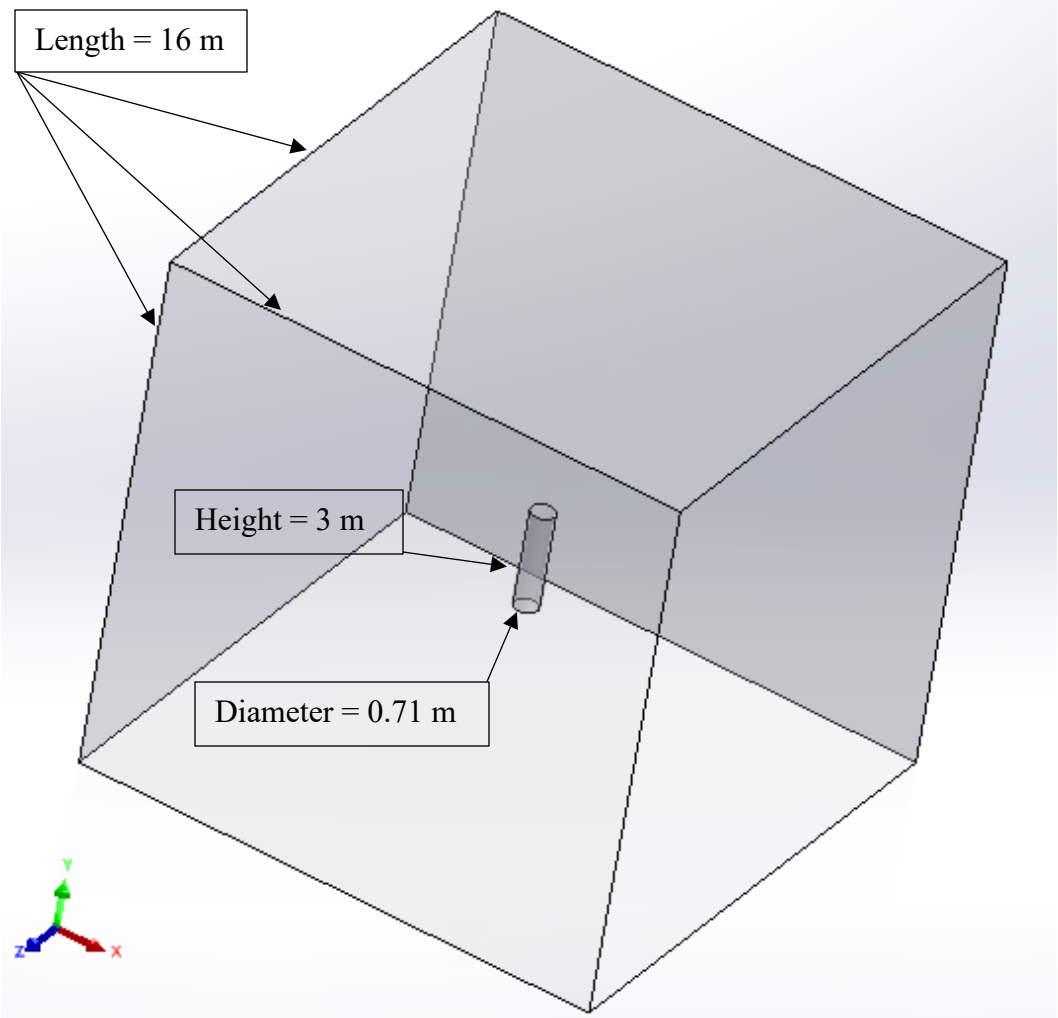

Figure 10. Single Actuator Disk Fluid Model

B. DOMAIN MESHING

The final disk in free space mesh consisted of 4.5 million nodes and 10.8 million elements. The CFD setup details and settings for the disk in free space are included in Appendix C. Figure 11 shows a cut halfway through the volume to view the internal portions of the mesh.

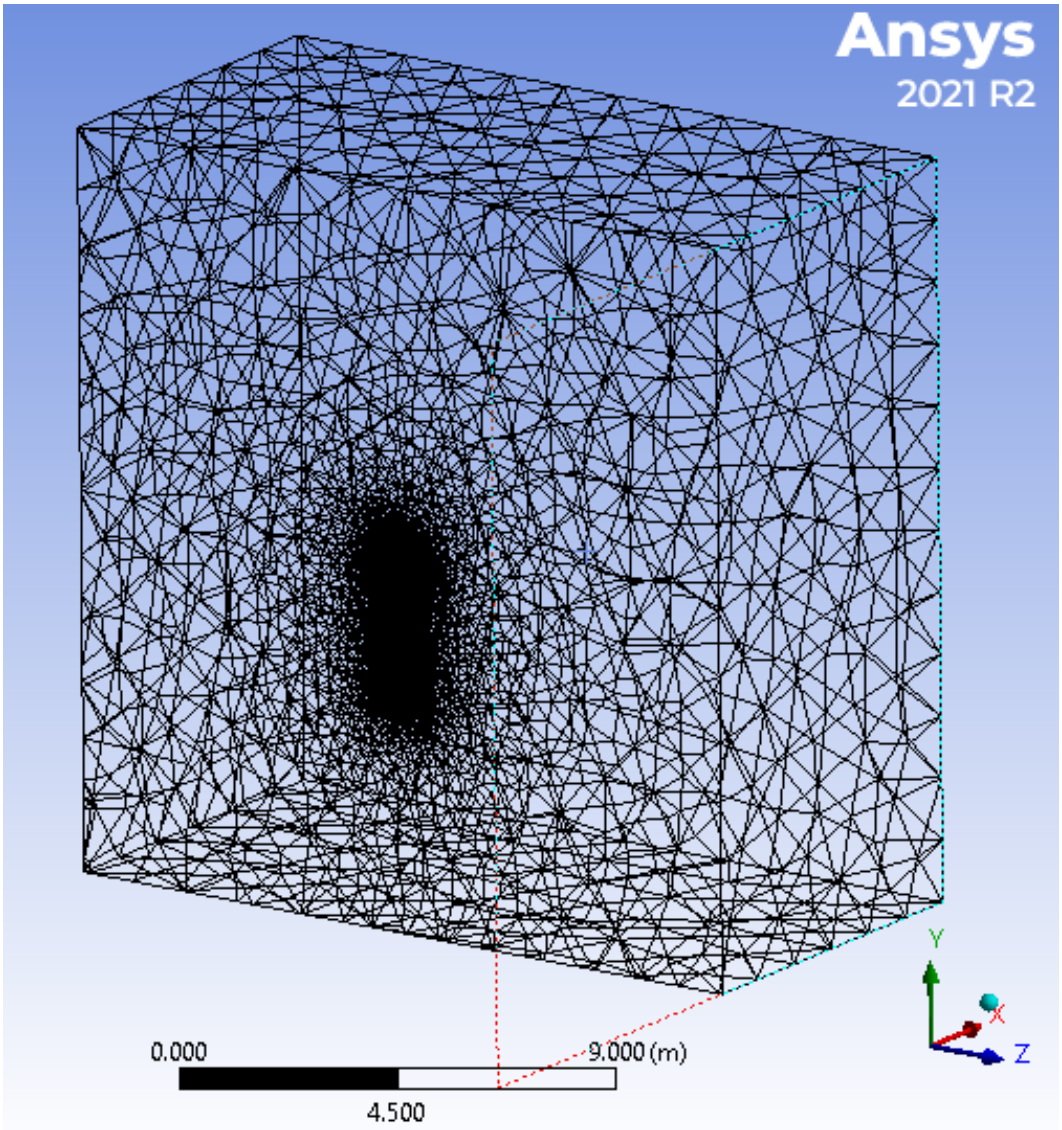

Figure 11. Single Actuator Disk Mesh

For disk meshing, a sphere of influence was attached to the center of the Actuator Disk's surface through geometry selection. The sphere of influence has a radius equal to the disk radius and influences all fluid volumes. Next, a face sizing for all inner and outer cylindrical faces and the bottom surfaces of the cylinder volume was applied to ensure element size was consistent across the fluid-to-fluid boundary. Figure 12 shows a zoomed in view of the final Actuator Disk mesh.

Initially, a course mesh of approximately 100,000 nodes was run to obtain a rough solution that could be quickly manipulated to match the craft of interest's numbers. The sphere of influence and face sizing allowed for simple refinements of the mesh at the disk and around the disk edge.

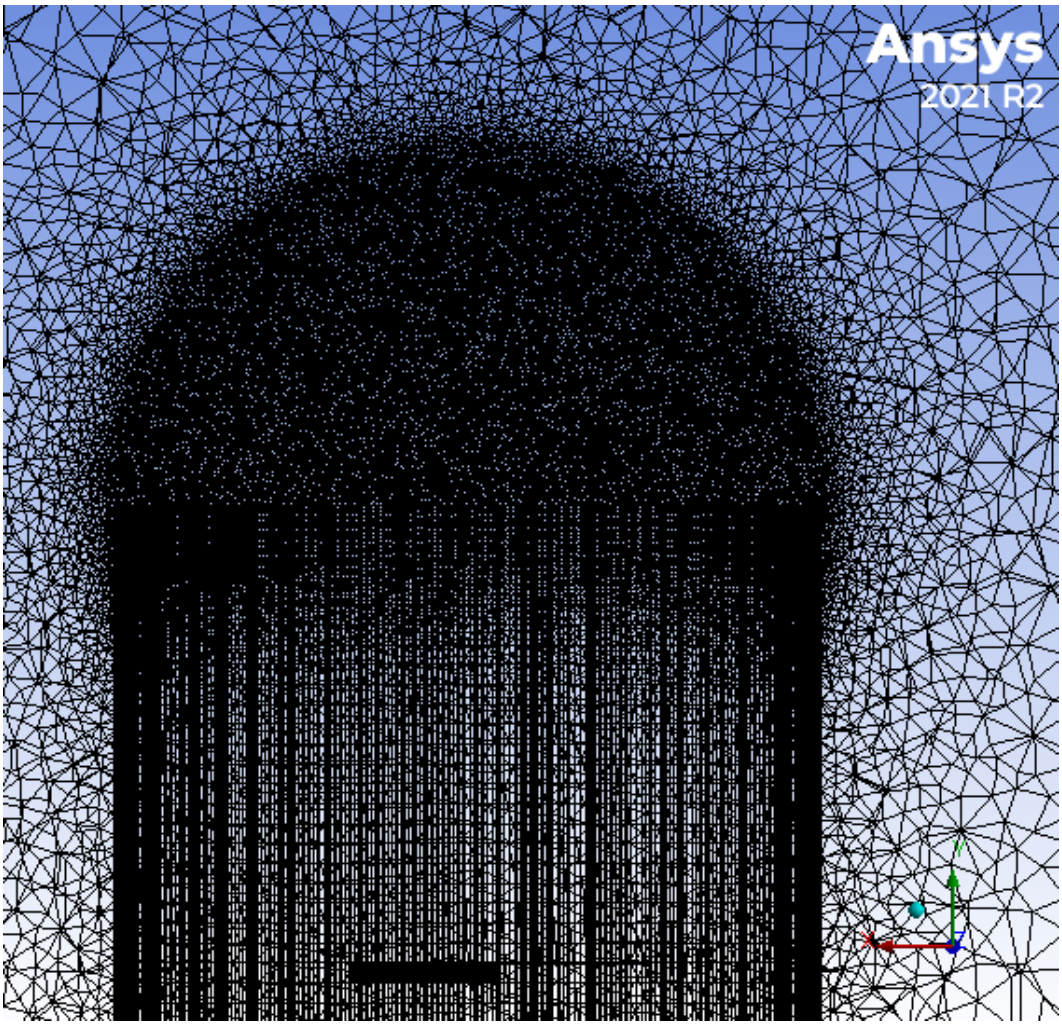

Figure 12. Actuator Disk Mesh

C. PROBLEM SETUP

For the setup, an isothermal steady-state analysis at 25 °C and 1 atm using the Shear Stress Transport turbulence model was utilized for all calculations. The flow was assumed fully turbulent, so no transition model was used. An isothermal analysis was utilized due

to the speeds being analyzed remaining less than thirty percent of the sonic speed and to decrease computational load. The Shear Stress Transport model was chosen so that the boundary layer effects on the crafts could be calculated and analyzed. All outer boundaries of the fluid domain were initially defined as Entrainment Openings with a relative pressure of 0 Pa. The upper and lower disk surfaces were also defined as openings with the velocity at the disk specified in cylindrical coordinates using the polynomials described earlier.

1. Hover Flight

Hover flight is the simplest flight mode for the disk as the thrust to weight ratio must equal 1. With no incoming flow, the disk must entrain all the flow necessary to counter gravity and keep the craft aloft. To achieve this, an expression for the hover velocity was inserted and scaled. The expected thrust per disk with the craft in hover is 27.0 N for a total craft thrust of 162 N. Applying a completely uniform axial velocity distribution in a CFD environment was not able to create the thrust required, so the polynomial velocity distributions were created to better model propeller flow. The completely uniform flow is also physically unrealistic as the work done by the propeller should vary with distance from the center. Figure 13 shows the hover flight setup.

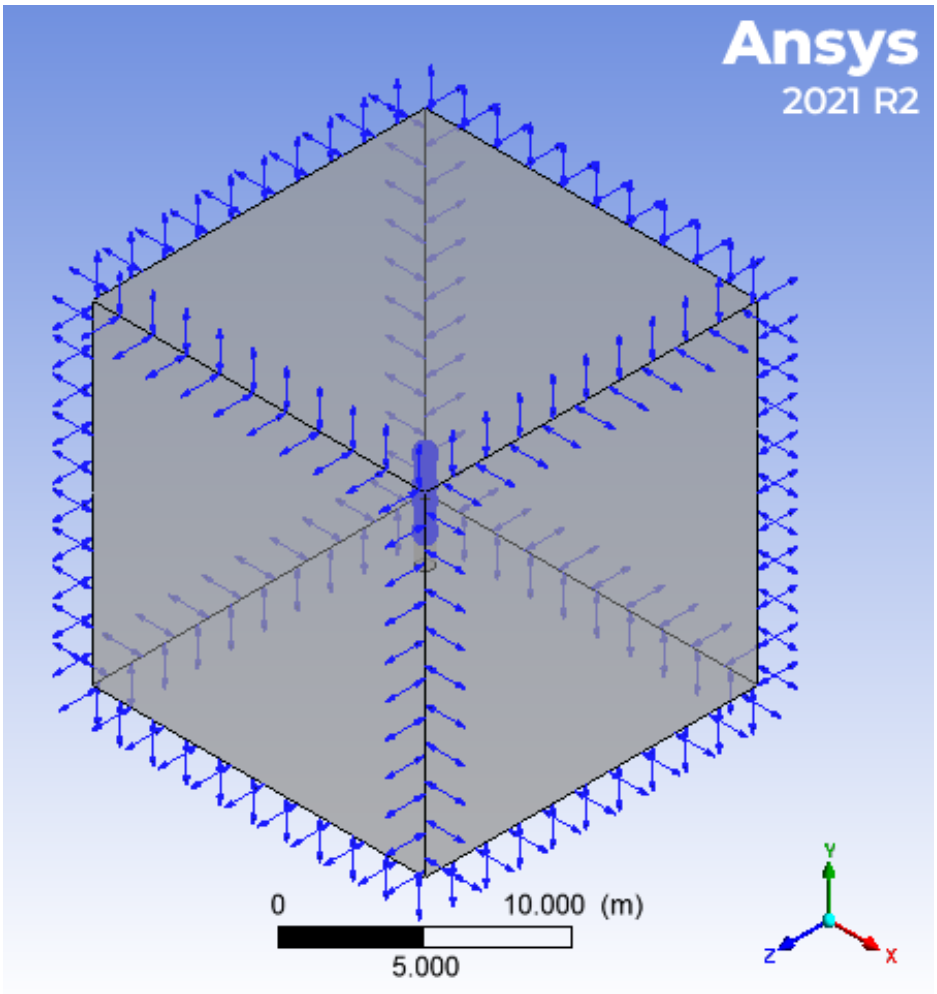

Figure 13. Single Actuator Disk Hover Flight Setup

2. Vertical Flight

For vertical flight, the outer Top boundary was redefined as an inlet with velocity specified in cartesian coordinates. At the disk, the inlet and induced velocities summed in cylindrical coordinates along the axial dimension. The COTS platform model projected area is 0.287 m^2 and with the drag coefficient estimated by a flat plate perpendicular to flow (C_d = 1.28 [20]), the desired thrust per disk is 27.8 N for a total craft thrust of 167 N. The Flying Wing has a projected area of 0.432 m^2 and with a drag coefficient estimated by an airfoil (Cd = 0.05 [20]), the desired thrust per disk is 27.0 N for a total craft thrust of 162 N. Figure 14 shows the vertical flight setup with the outer domain top surface redefined as an inlet.

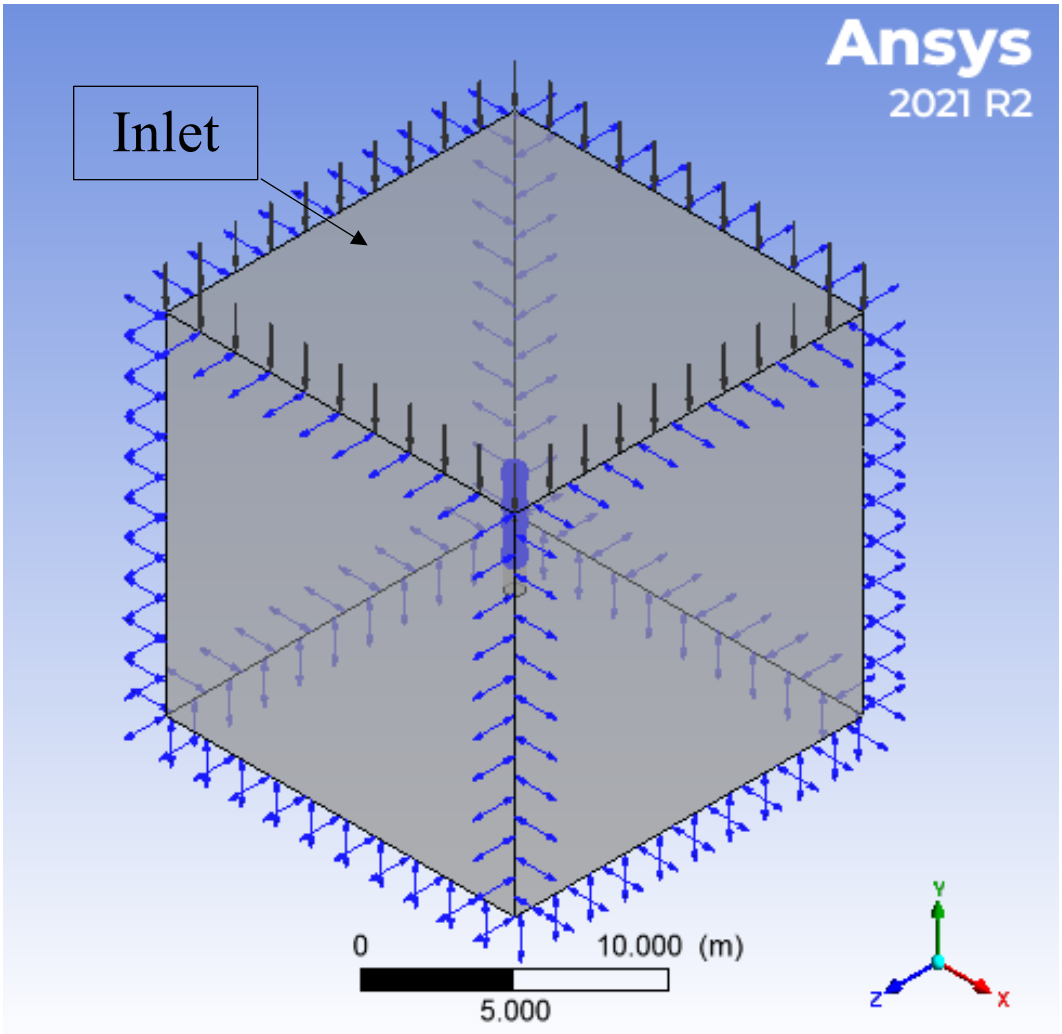

Figure 14. Single Actuator Disk Vertical Flight Setup

3. Forward Flight

For forward flight, both the outer Top and Left boundary were defined as an inlet with velocity specified in cartesian coordinates. At the disk, the inlet and induced velocities were summed in cylindrical coordinates along the axial and radial dimensions. The forward flight expectations will differ with inlet velocity and generated lift force. The expected trend is for the Flying Wing to require less thrust in each forward flight case due to the airfoil body. Figure 15 shows the forward flight setup with the outer domain top and left surfaces redefined as inlets.

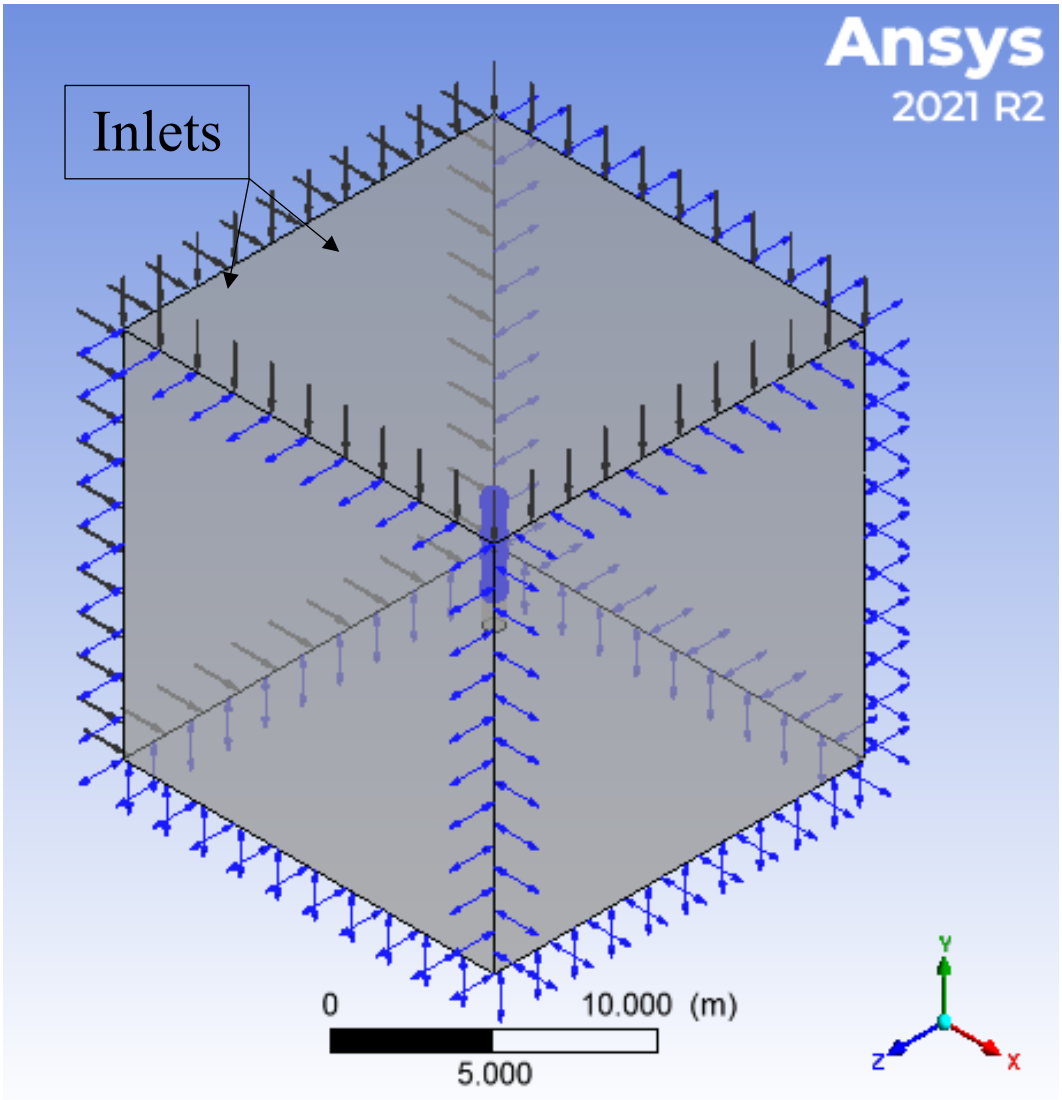

Figure 15. Single Actuator Disk Forward Flight Setup

The same setup modeling scheme was also used for the two UAV fluid domains.

D. RESULTS

1. Hover Flight

For the actuator disk in free space, the modeling goal was to match the real-world thrust generated by the craft. With no significant lift or drag forces on the body, the total craft thrust must counter the weight of the craft. For an MTOW of 16.5 kg, the expected thrust per disc is 27.0 N with an average v_h = 5.36 m/s across the disk. A uniform axial

velocity distribution was the first case modeled followed by the polynomial axial velocity distribution and the polynomial axial and radial velocity distributions. In all the tables in this thesis, the Expected thrusts are derived from the balance of forces in the thrust direction. The other values of thrust provided are the result of integrating the pressure forces over all the disk surfaces. The expected thrust was an input to all models for that flight case. Table 1 shows the expected thrust versus thrust results from the hover simulations.

Table 1. Single Disk Hover Thrust

Expected Thrust	27.0 N
Uniform Disk Loading	11.6 N
Axial Polynomial Disk Loading	17.6 N
Axial and Radial Polynomial Disk Loading	26.8 N

a. Uniform Axial Distribution

Applying $v_h = 5.36$ m/s uniformly across the disk yielded 11.6 N of thrust. Figure 16 shows the velocity distribution from a uniform loading. From Figure 16, a fluid spreading is seen from the bottom of the disk with small regions of extremely high velocity on the top of the disk near the edge. The induced velocity at the disk edge is not zero which causes high sheer stresses in the fluid, and an ever-tightening vortex around the disk edge. If the mesh was a continuum, infinite values for acceleration would exist at the edge. As a result, the imposed non-zero boundary condition at the edge causes large losses in the flow, a significant reduction in thrust, and is non-physical.

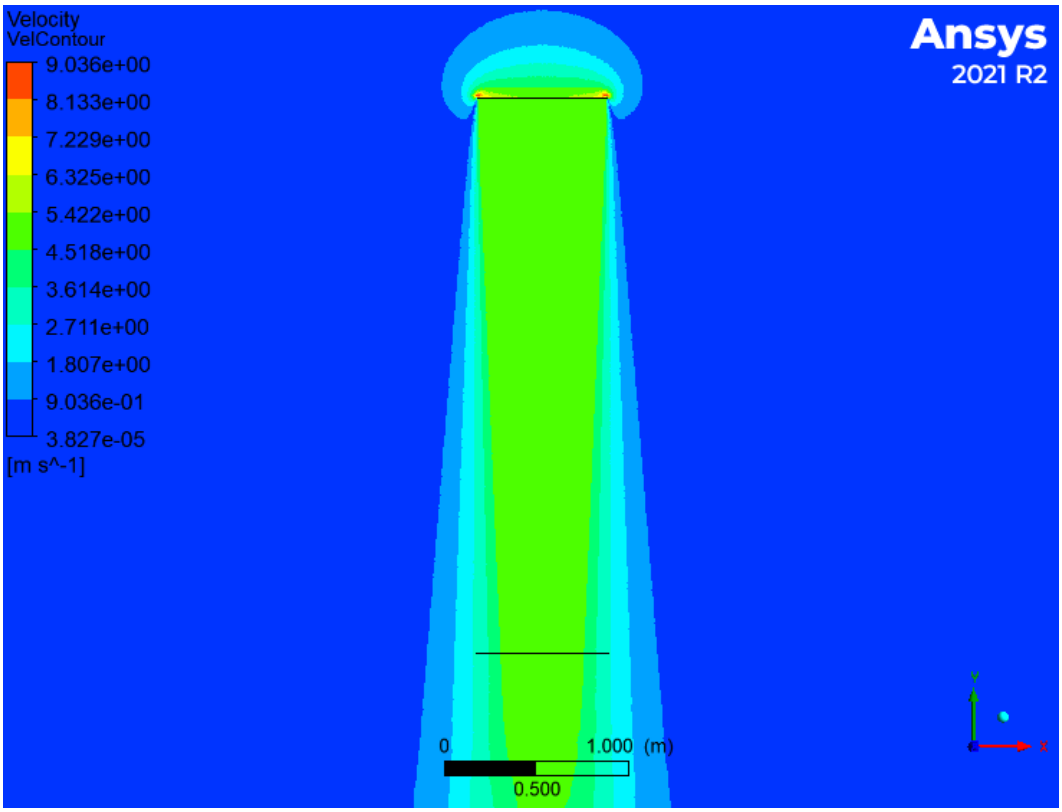

Figure 16. Uniform Axial Distribution Velocity Contour Plot

In addition, Figure 17 shows the streamlines from the uniform axial velocity distribution have no stream tube contraction at the disk.

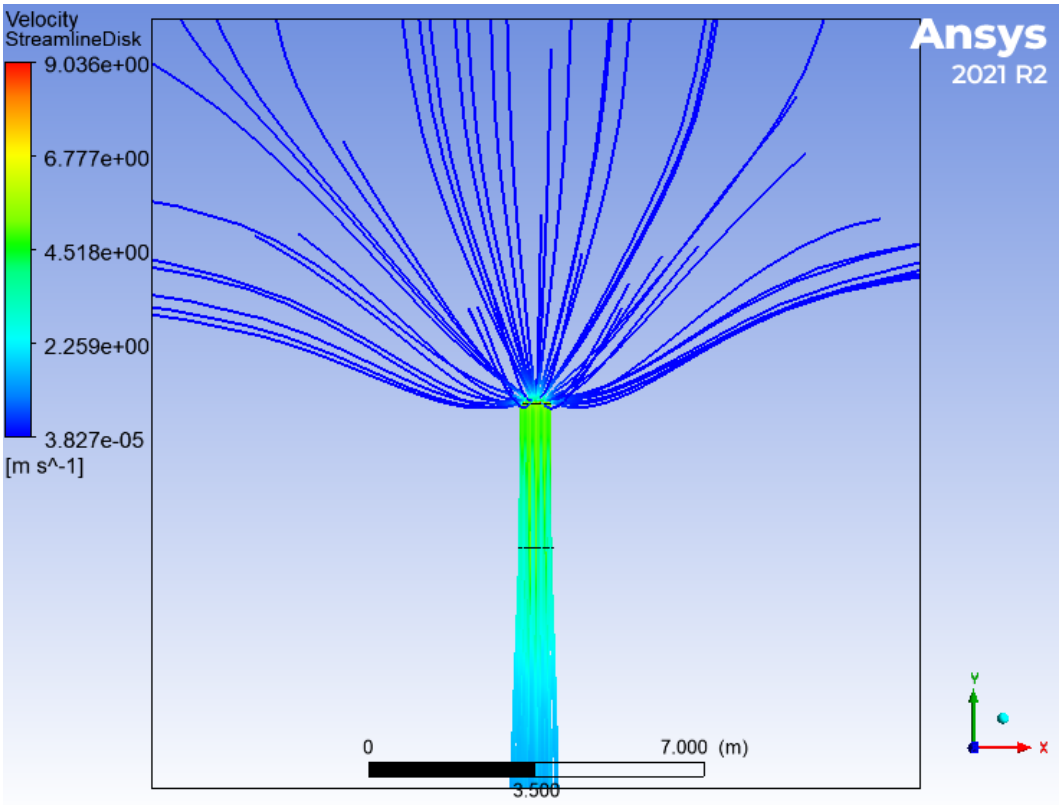

Figure 17. Streamlines from Uniform Axial Distribution

b. Polynomial Axial Distribution

The volumetric flow rate from the uniform distribution was then redistributed across the disk radially via a polynomial axial velocity distribution. Figure 18 shows the velocity distribution from a variable axial distribution only. Figure 18 shows a migration of high entrainment regions inward along the upper disk surface to the mid radius point. The redistribution required a peak velocity, $V_p = 9.32$ m/s at 0.185 m to match the flowrate predicted by AMT and produced a disk thrust of 17.6 N.

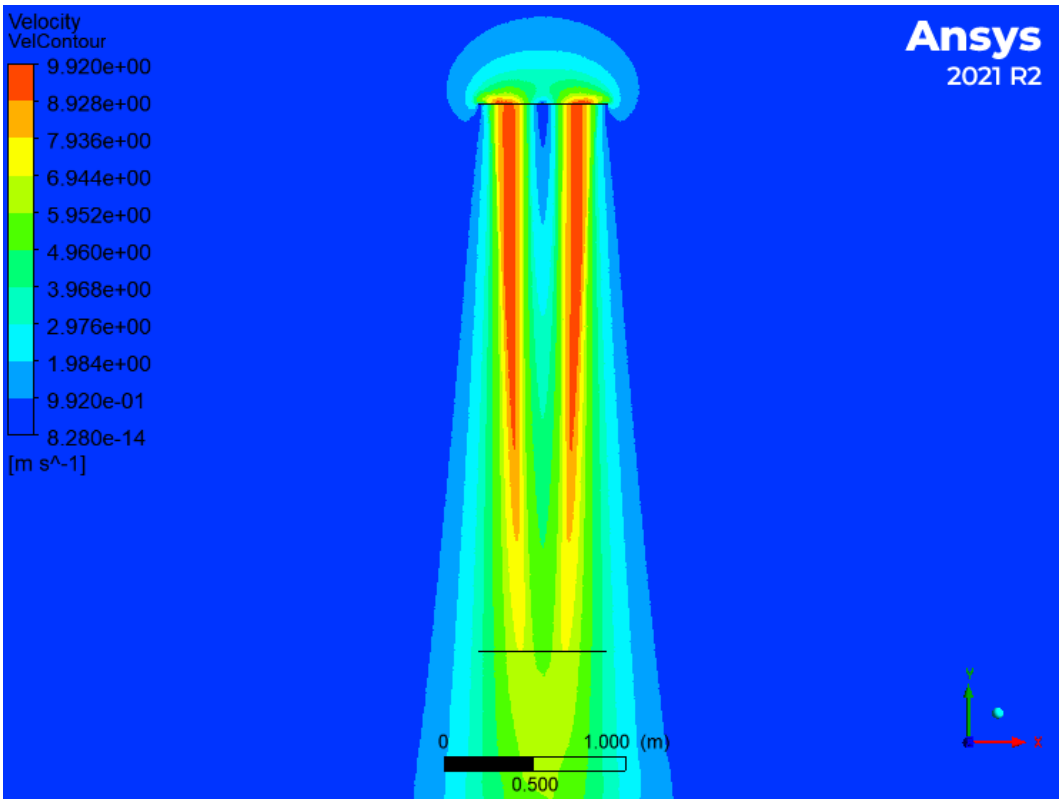

Figure 18. Axial Polynomial Distribution Velocity Contour Plot

Figure 19 shows the streamlines from a variable axial loading only. Figures 18 and 19 still do not show significant stream tube contraction at the disk. The stream tube contraction is important to model because the propeller creates a tip vortex that radially compresses the flow beneath the disc. For pressure to increase on the lower surface of the disk, flow curvature at the disk must be present. Qualitatively, Figure 19 appears to show a larger entrainment of fluid through the disk than the uniform axial velocity distribution.

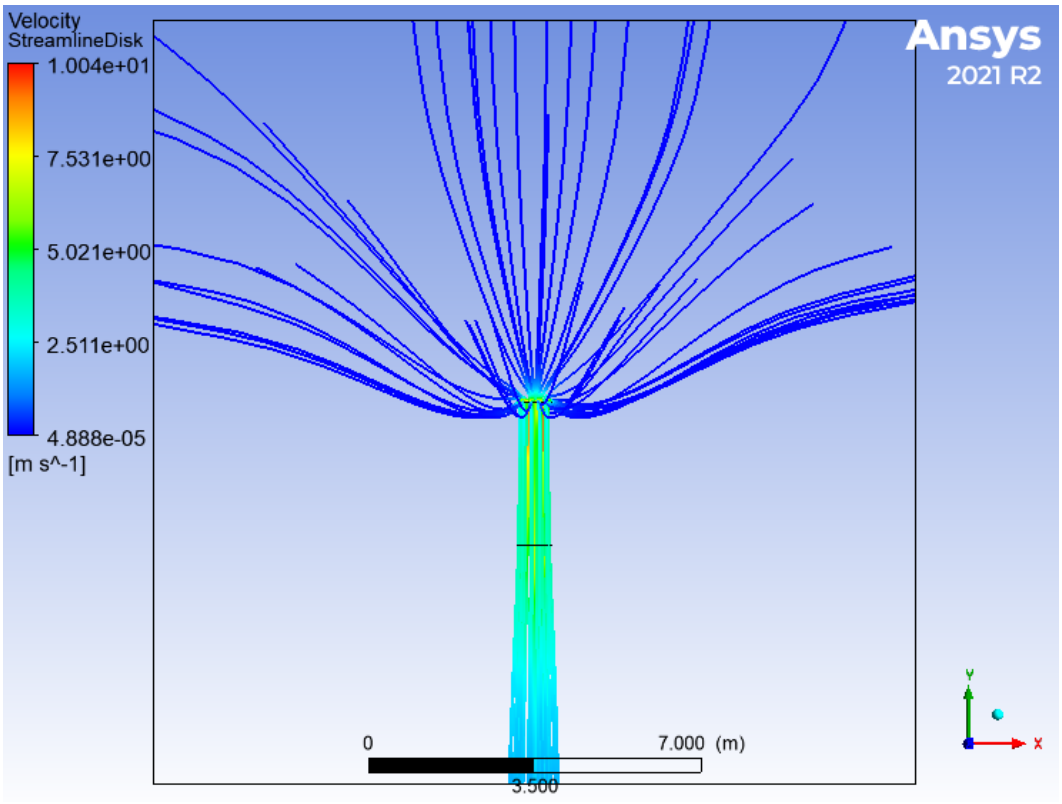

Figure 19. Streamlines from Axial Polynomial Distribution

c. Polynomial Axial and Radial Distribution

Through iteration, the polynomial axial velocity distribution was determined to induce reversed fluid flow through the inner portions of the disk for certain values of R_p. The reversed flow was determined to be non-physical for the cases of flight considered in this thesis. To avoid reversed flow, the values of R_p were iterated using a MATLAB script through a range of $0.5 * R_o \leq R_p \leq 0.75 * R_o$ with the polynomial radial velocity distribution applied in conjunction. The raw CFD data and the graphing code for the variation is available in Appendix D. Figure 20 shows the thrust results from simulations as a function of peak radius.

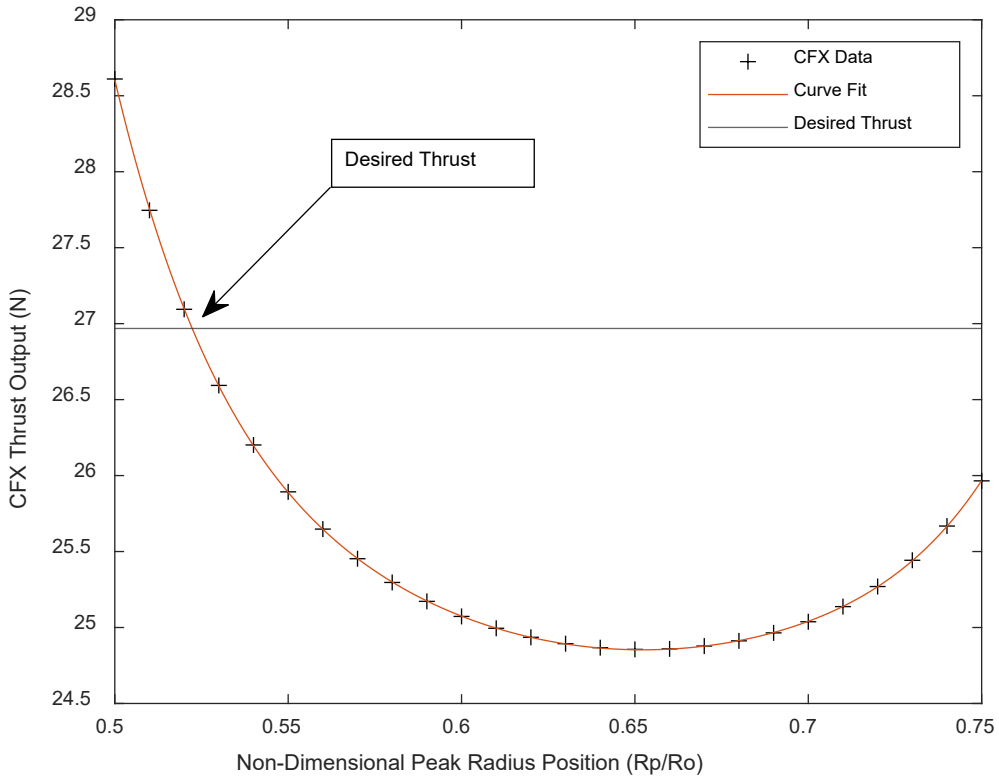

Figure 20. Peak Radius Location versus Thrust

The peak radius variation only produced one solution that gave good agreement with desired hover thrust over the range investigated. The radial location of the peak velocity that gave good agreement with the desired thrust was $0.5223 * R_o$ which is equal to 0.185 m. This peak radius was held constant over all simulations and may not be a good assumption. The resulting axial velocity distribution is overlaid on CFD data obtained from propeller simulations done by Richmond [19]. The raw axial velocity CFD data and the graphing code for the overlay is available in Appendix E. Only the position of the peak radius was varied in this thesis.

Comparing the generated axial velocity distribution to the axial velocity profile from the propeller simulations shows the generated profile does not model the blade loading of the actual propeller. The other axial velocity polynomials may generate better fits of blade loading of the propeller. Figure 21 shows the raw axial velocity distributions from all single actuator disk in free space hover simulations over Richmond's data.

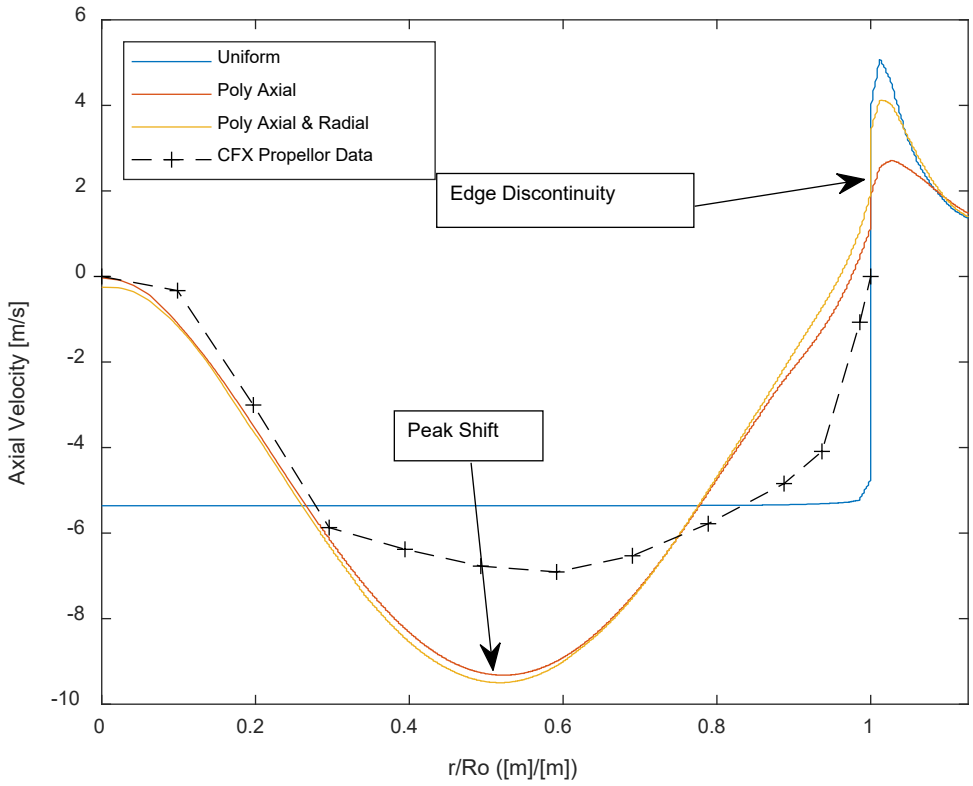

Figure 21. Raw CFX Axial Velocity Distributions versus Radius. Source: [19].

The data provided by Richmond shows a fuller shaped blade loading. This shape is more difficult to mimic with a polynomial. To achieve the same thrust, both polynomial distributions shift the position of peak velocity inwards and increase the magnitude. This distribution is exaggerated in the pressure distribution by the dynamic pressure term $(\frac{1}{2}\rho v^2)$ in Equation 1. The volumetric flow through the disk is held constant, so the higher and lower pressures act on smaller areas. The resulting integration of the pressures over the same area would be within error tolerance to the actual distribution.

When both polynomial velocity distributions were applied, a non-zero axial velocity was generated at the disk center. The reason for the non-zero velocity is unknown and requires further investigation but is likely related to the use of an opening boundary condition versus a connected inlet and outlet boundary condition for the actuator disk.

The uniform axial velocity distribution has the largest edge discontinuity of the three profiles investigated which helps explain the large loss in thrust observed. All data utilized in Figure 21 is available in Appendix F. The addition of a radial velocity component through the disk required a $V_p = 10.6$ m/s at 0.183 m and a produced a disk thrust of 26.8 N. The addition of the radial polynomial resulted in radial location of V_p slightly more towards half the radius with a slightly larger magnitude when compared to the axial polynomial velocity distribution alone. Those small adjustments in V_p location and magnitude recovered nearly all the missing thrust for an error of 0.61% from expected. Different values of hover thrust were simulated with the same error achieved. Figure 21 shows the velocity jump at the disk edge is larger than when the polynomial axial distribution is applied alone most likely due to the increased velocity induced by the disk.

Figure 22 shows the velocity distribution from the ideal peak radius axial and radial loading combination. Figure 22 shows the inward migration of the high entrainment regions along the top of the disk combined with stream tube contraction beneath the disk. The high entrainment regions on the upper surface of the disk have a smoother transition across the disk than applying the axial polynomial distribution alone.

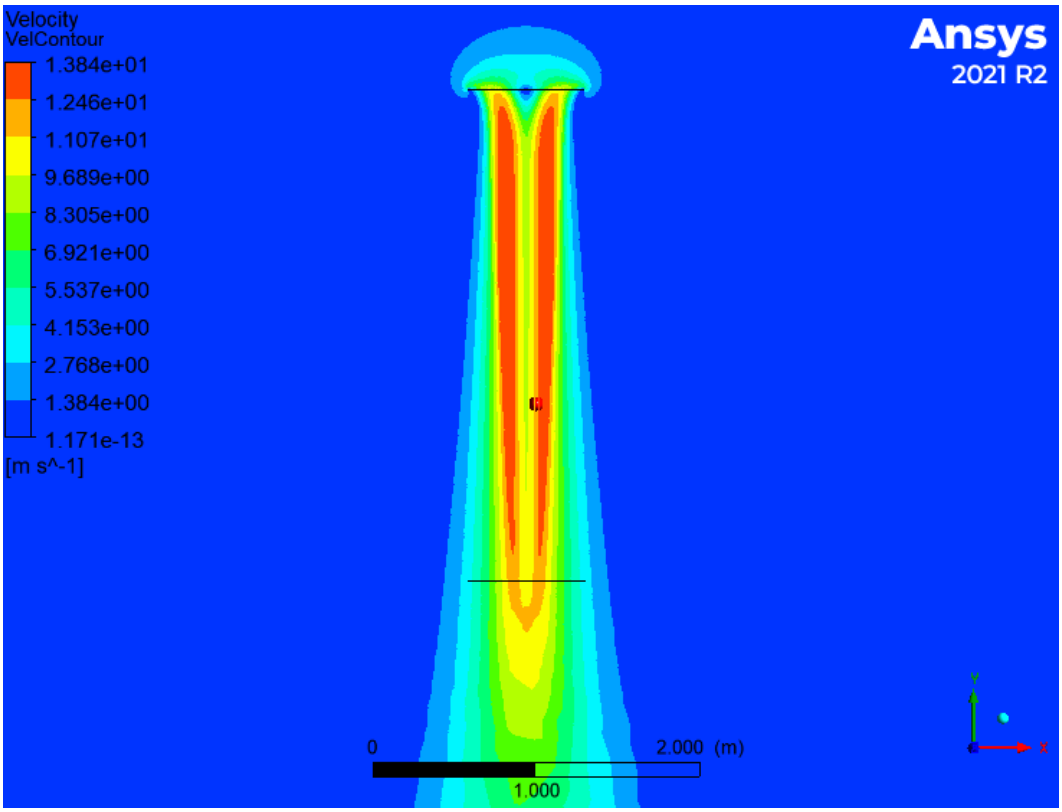

Figure 22. Axial and Radial Polynomial Distribution Velocity Contour Plot

Figure 23 shows the streamlines from the same loading setup. Figure 23 shows the streamlines also contracting. Qualitatively, the streamlines appear to show the largest entrainment of fluid through the disk of the three distributions investigated.

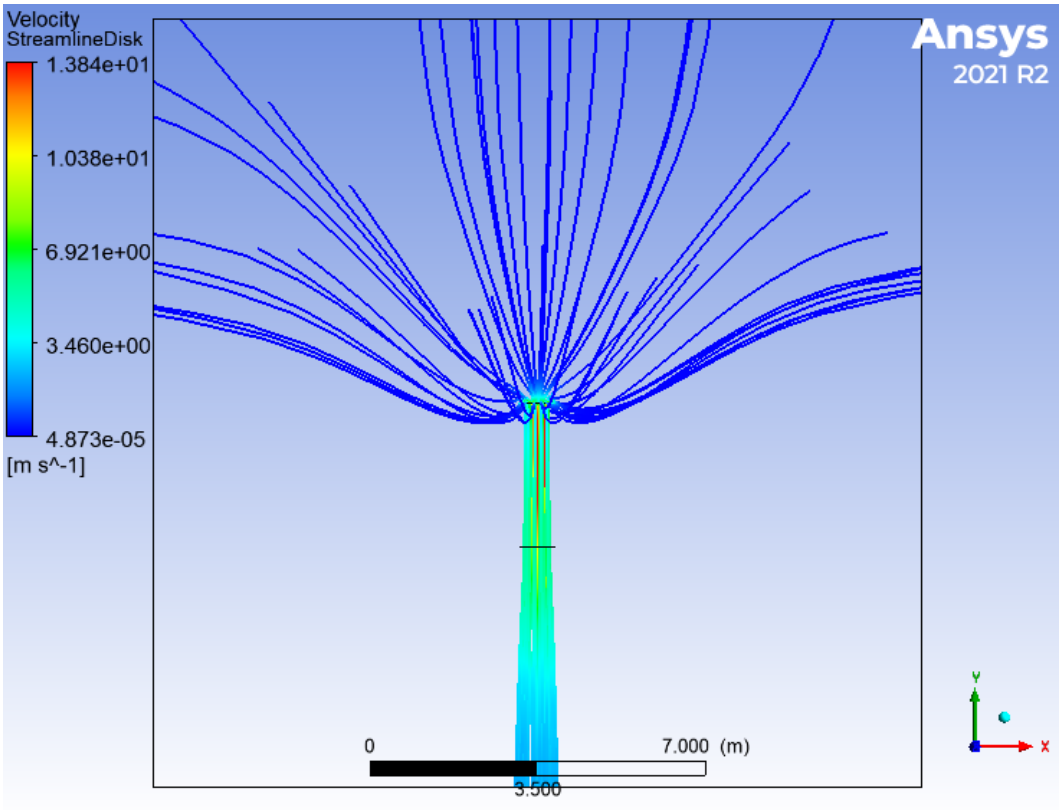

Figure 23. Streamlines from Axial and Radial Polynomial Distributions

2. Vertical Flight

In steady climb, there is no acceleration. Since the craft is not accelerating and a disk in free space has no walls to create drag, the thrust produced must again equal the craft weight. In vertical flight, the induced velocity is reduced due to the incoming flow. The disk needs to add momentum to the flow passing through. The thrust and power required still increases due to the total flow through the disk increasing ($V = V_c + v_0$). Table 2 shows the expected versus obtained thrust results for climbing flight.

Table 2. Single Disk Vertical Climb Thrust

2 m/s Expected Thrust	28.1 N
2 m/s Vertical Climb Thrust	25.6 N

The disk in free space with a 2 m/s inlet flow required a $V_p = 10.7$ m/s and produced a disk thrust of 25.6 N. From Figure 24, there are regions of nearly zero velocity just below the disk edge. The peak radius utilized was not adjusted from the hover case for any of the following cases modeled. This assumption may be incorrect and needs further investigation in follow on study. Figure 24 shows the velocity distribution for climbing flight.

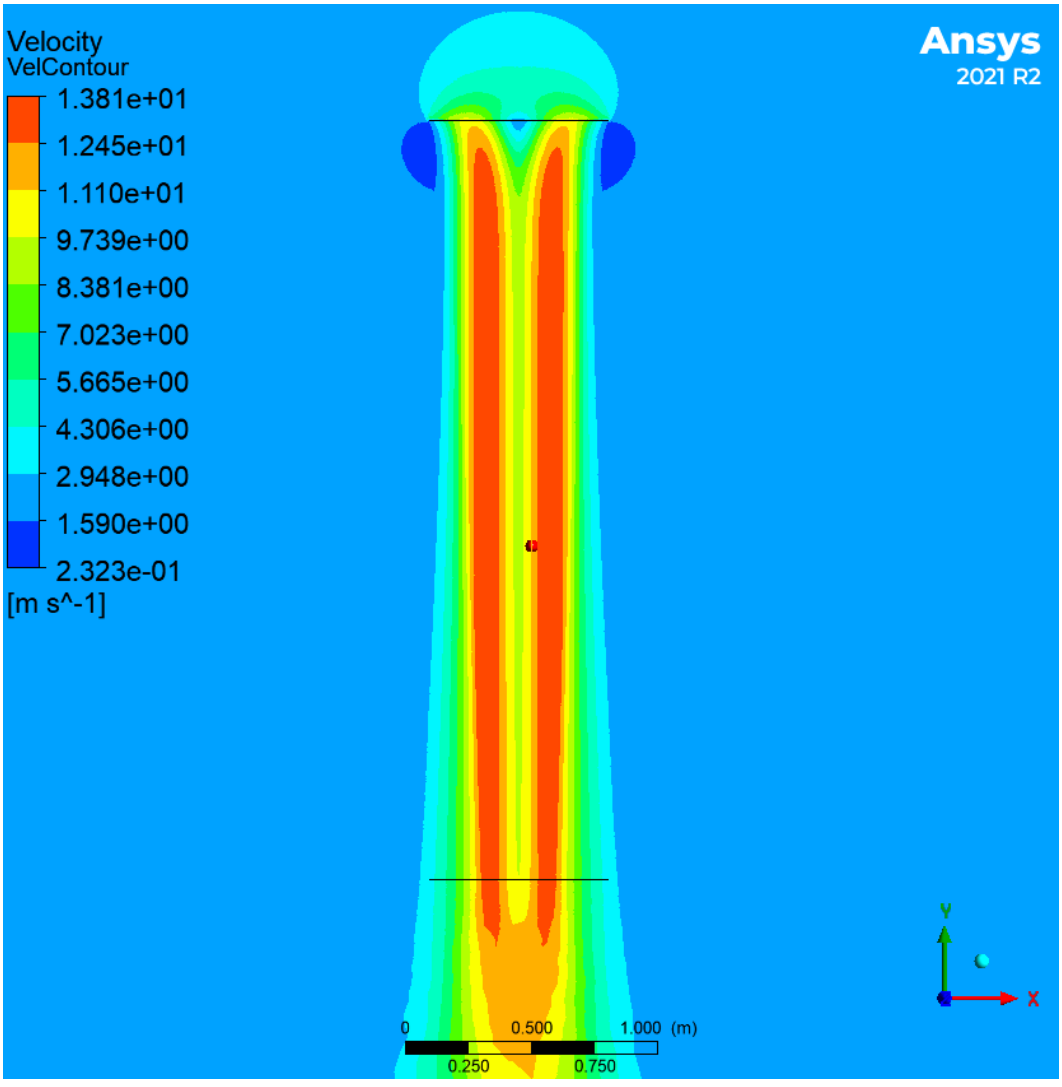

Figure 24. 2 m/s Vertical Climb Velocity Contour Plot

Figure 25 shows the streamlines for climbing flight. In Figure 25 the streamlines in vertical climb continue to show contraction through the disk. Adjustments may need to be made to the vertical climb model to achieve the desired thrust but were not investigated due to time constraints.

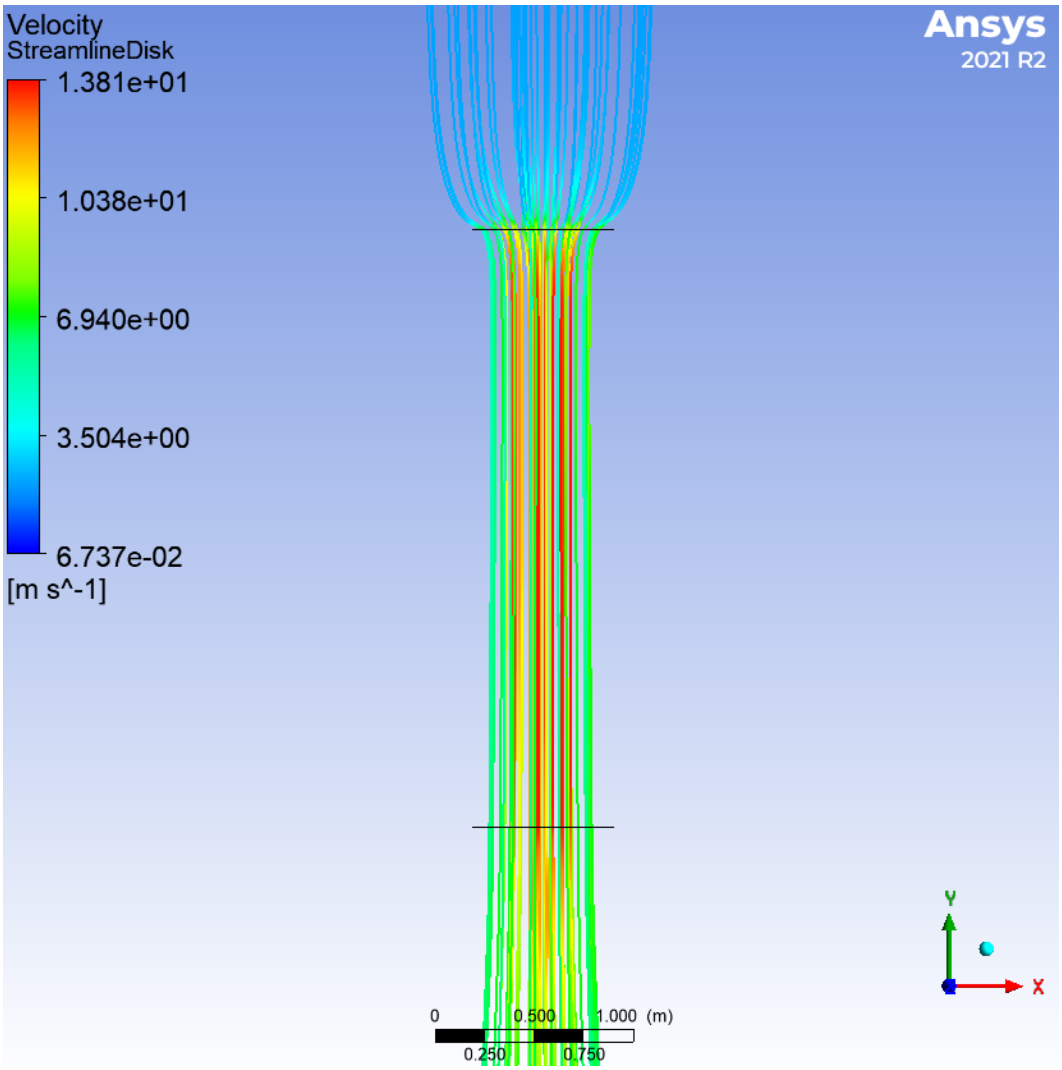

Figure 25. Single Disk in 2 m/s Vertical Climb Streamlines

3. Forward Flight

With no walls to create drag, the thrust expected is to counter the weight of the craft. Forward flight differs from vertical flight in that some of the velocity that passes

through the disk is parallel to the disc surface. Due to lack of experimental data available for the COTS platform, the linear relationship from Yang's research and the COTS platform brochure was used to estimate all Actuator Disk AoA to be two times the platform's true airspeed [7,8]. Due to the lack of platform specific experimental data, the simulations may not be in equilibrium. Table 3 shows the expected versus obtained thrust from forward flight.

Table 3. Single Disk Forward Flight Thrust

2 m/s at 4° Actuator Disk AoA Expected Thrust	27.1 N
2 m/s at 4° Actuator Disk AoA Thrust	19.6 N

The VTOL craft convention for Actuator Disk AoA shown in Figure 7 will be maintained throughout all analyses. The chord AoA is defined as the AoA the external flow makes with the UAV's chord. The chord AoA will be used to compare the two UAVs in forward flight. For the COTS platform, the Actuator Disk AoA and chord AoA will be the same angle since the craft's chord is in the same plane as the actuator disks. For the Flying Wing, the craft's chord AoA is perpendicular to the plane the actuator disks are located in. The Flying Wing's chord AoA, ϵ, is defined as:

$$\epsilon = 90° - \alpha \tag{9}$$

Figure 26 shows a 2 m/s forward velocity at an Actuator Disk AoA of 4°. From Figure 26, the large crossflow velocity is seen interacting with the flow produced by the disk. In addition, the disk inlet shows heavy regions of entrainment toward the front half of the disk. The losses in thrust may be a model limitation as the translation lift seen in slow cruise for similar platforms appears to not be a part of the model. For the thrust to counter the weight, the vertical component of thrust must equal the weight. The vertical component of the resulting thrust provides 19.5 N of the 27.0 N desired. This result was not fully investigated due to time constraints and needs to be fully investigated in a follow-on study. Figure 26 show the velocity distribution from this forward flight case.

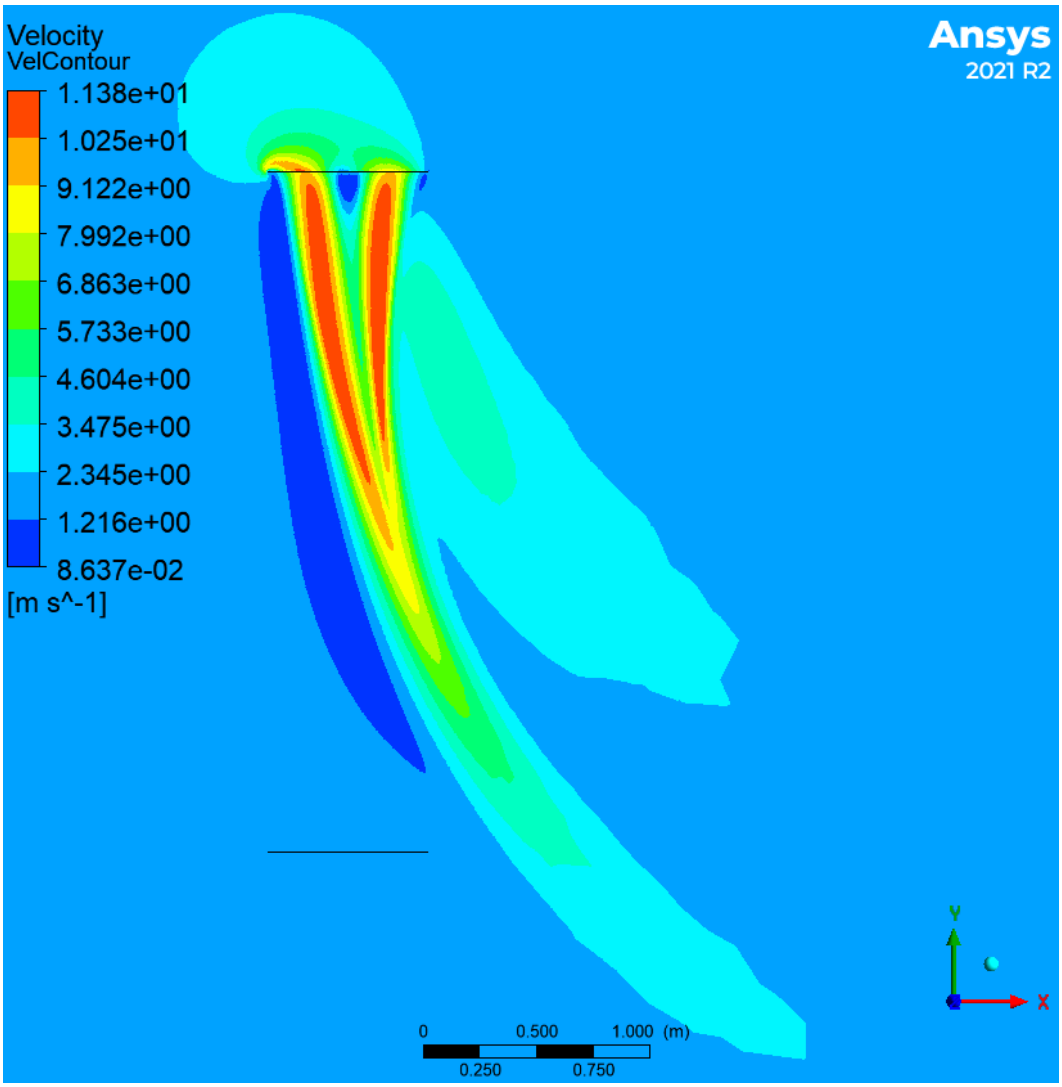

Figure 26. 2 m/s 4° α Velocity Contour Plot

Figure 27 shows the streamlines from this forward flight case. The streamlines in Figure 27 continue to show the stream tube contraction at the disk, flow redirection through the disk, and the external flow interaction with the induced flow. The arrow on Figure 27 shows the direction of forward flight.

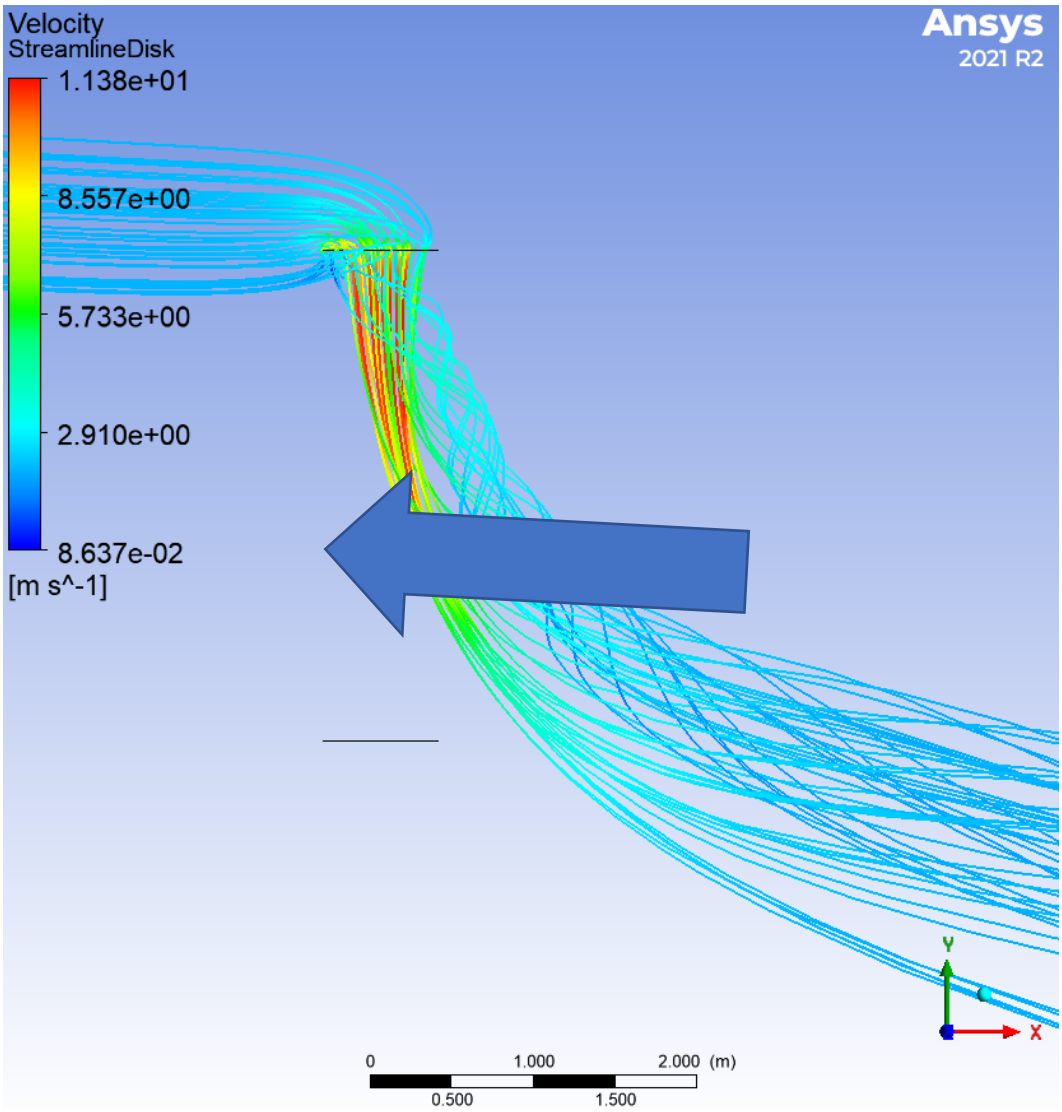

Figure 27. 2 m/s 4° α Streamlines

The COTS chord AoA is the same angle as the Actuator Disk AoA. A benefit of the tilting aircraft is that the disk face becomes more perpendicular to the incoming flow which may make the model more accurate given the assumption of the same peak radius for all models. In addition, the thrust produced in forward flight mainly overcomes aerodynamic drag. Figure 28 shows the velocity distribution from the forward flight case expected from the Flying Wing. Figures 28 and 29 show the same inlet speed and chord AoA results for the Flying Wing. Figure 28 shows the significant reduction in crossflow by reorienting the incoming flow more perpendicular to the disk face.

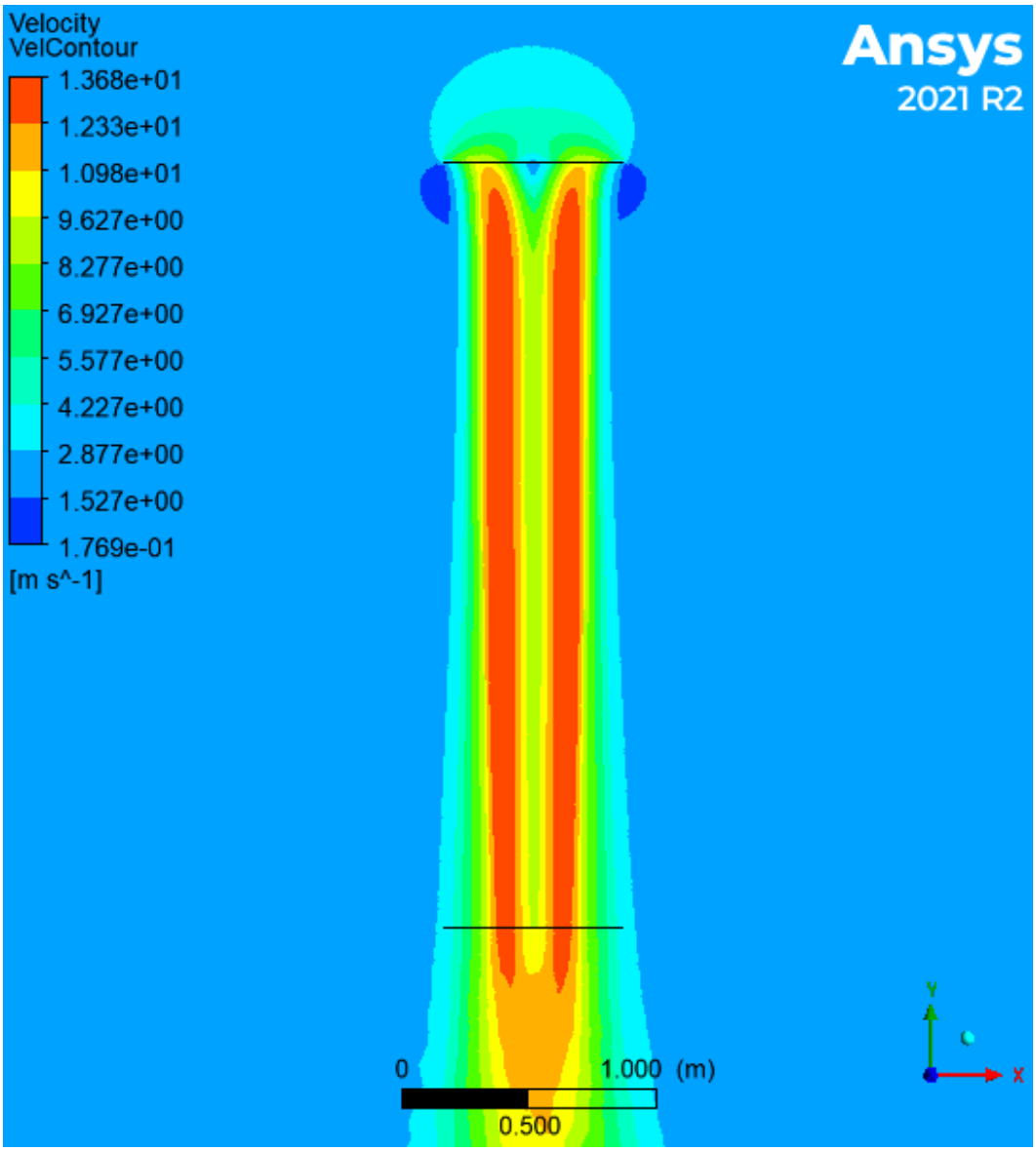

Figure 28. 2 m/s 86° α Velocity Contour Plot

Figure 29 shows the streamlines from the same forward flight case as Figure 28. Figure 29 also shows the stream tube contraction from the disk and flow redirection of the offset incoming flow.

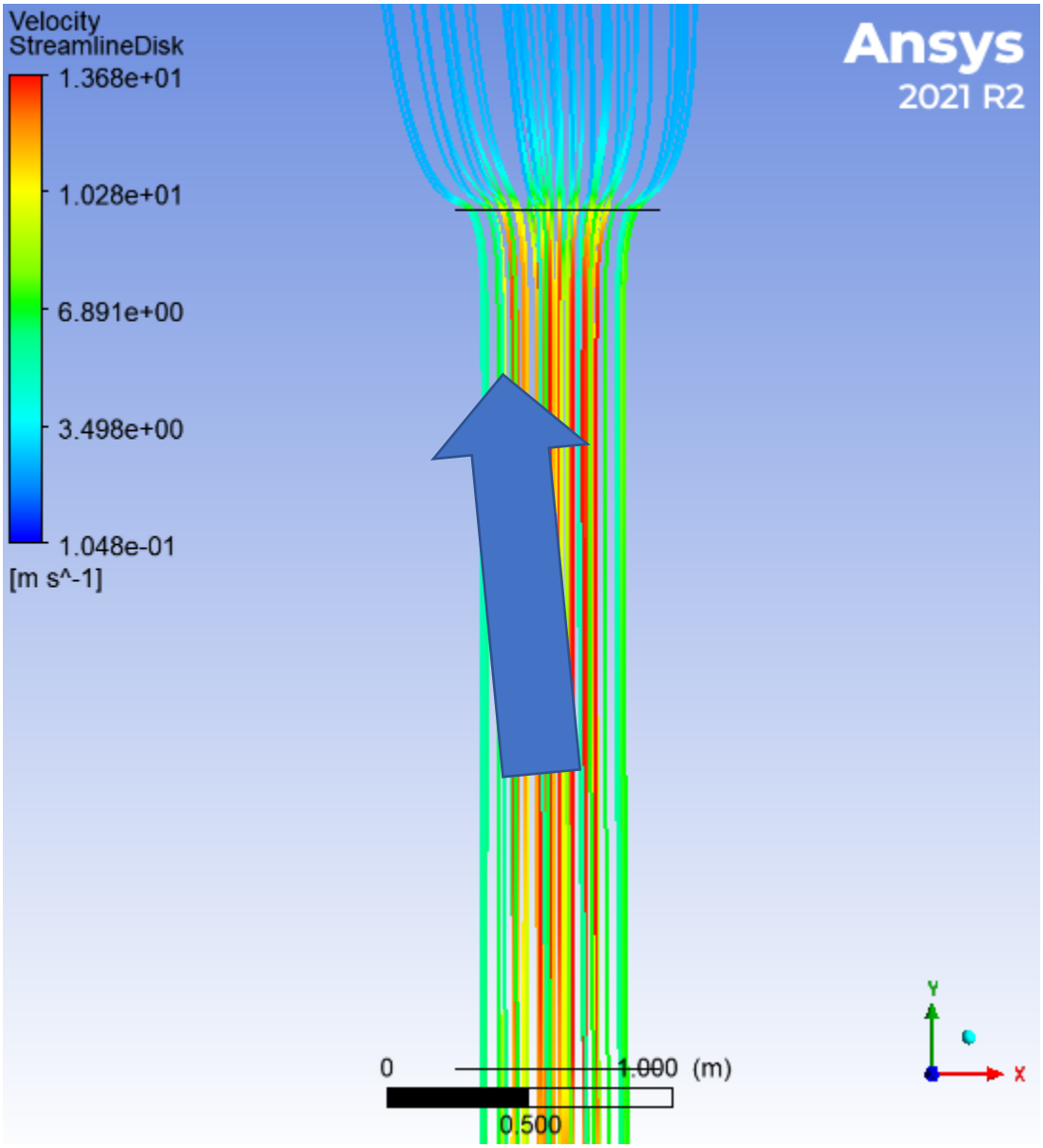

Figure 29. 2 m/s 86° α Streamlines

Adjustments need to be made to the forward flight model but were not made due to time constraints. Additional data on the relationship between platform true airspeed and Actuator Disk AoA needs to be collected as well. With an individual disk in free space modeled across three regimes of flight, multiple disks in free space around a craft were modeled to look at multi-rotor craft.

THIS PAGE INTENTIONALLY LEFT BLANK

IV. CRAFT MODELING AND DESIGN

One challenge in obtaining efficient forward flight for multi-copters arises from the angle that develops to generate lateral movement which creates a conventionally negative lift force on the body [8]. This negative lift force must be overcome by additional thrust in the vertical direction produced from the craft. Another challenge in steady state forward flight is the force balance between thrust, gravity, lift, and drag. This force balance results in a tilting of the thrust vector to counter the gravitational and aerodynamic forces on the platform. The current COTS platform design minimizes thrust vector tilting and negative lift by having a small body and minimizing time in relatively high-speed forward flight.

A. COTS PLATFORM ANALYSIS

Treating the main frame as if it were a flat-plate wing, the COTS platform has a wingspan of 0.34 m and chord length of 0.54 m. The resulting aspect ratio is 0.63. The fuel cell is 0.315 m wide and attaches to the bottom of the craft. The wingspan of the craft is just large enough to securely attach the fuel cell. Figure 30 shows the COTS bluff body model used for simulations.

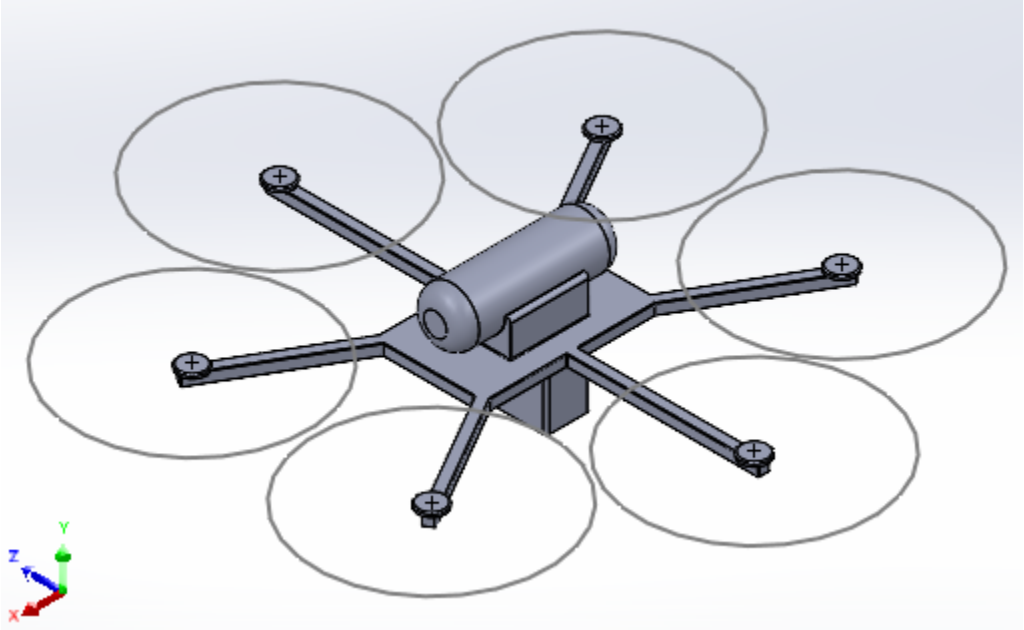

Figure 30. Bluff Body COTS Platform Model

The flat plate portions of the body house the batteries and control system electronics for the craft. The hydrogen is stored in a carbon-fiber fuel tank that is strapped to the top of the craft with Velcro. Landing legs were not modeled on either craft to reduce complexity and computational load but would produce additional side-force drag in cruise flight.

B. AIRFOIL SELECTION

The airfoil chosen for the Flying Wing was the NACA 0024 airfoil. The airfoil was chosen because of its thickness, symmetric geometry, and large range of increasing lift-to-drag ratio as a function of AoA. Figure 31 shows the lift-to-drag ratio as a function of angle of attack for various NACA airfoils.

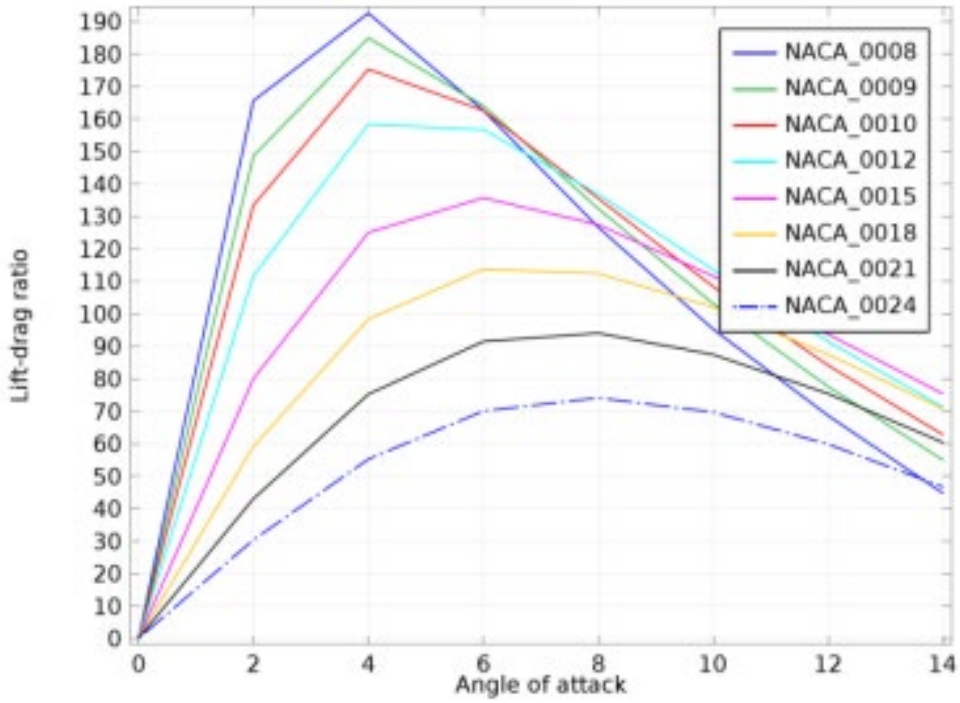

Figure 31. Lift to Drag Ratio versus Angle of Attack. Source: [21].

The airfoil shape was imported into SolidWorks from coordinates provided by University of Illinois at Urbana-Champaign Applied Aerodynamics Group [22]. The shape was scaled in SolidWorks so that the chord length of the airfoil was the same length as the flat body of the COTS platform. Figure 32 shows the imported shape.

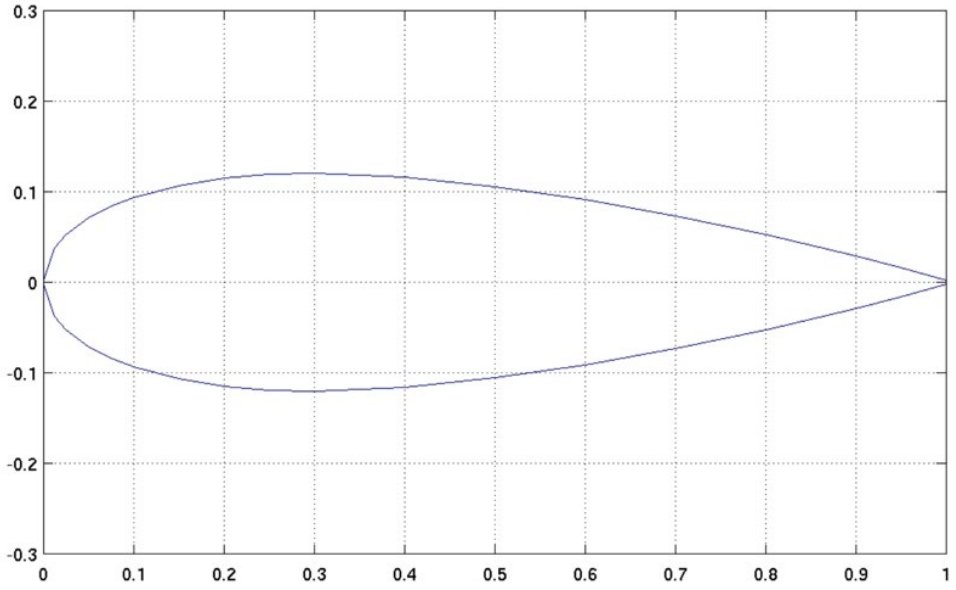

Figure 32. NACA 0024 Airfoil. Source: [22].

C. DESIGN PARAMETERS

An aspect ratio of 4 was utilized to maintain the two-person handling team design parameter of the COTS platform studied. The additional wingspan is inserted to ensure the wing area is large enough to generate a significant, conventionally positive lift force. For direct comparison, the same MTOW of 16.5 kg specified in the COTS platform brochure is utilized for the Flying Wing [7]. The tank and fuel cell were kept external to the wing with the same frontal area as the COTS platform for a fair comparison. All items external to the wing are centered and mounted along the quarter chord line. The Flying Wing platform is designed to take off in the VTOL configuration shown in Figure 3, then rotate approximately 90° into forward flight as shown in Figure 33.

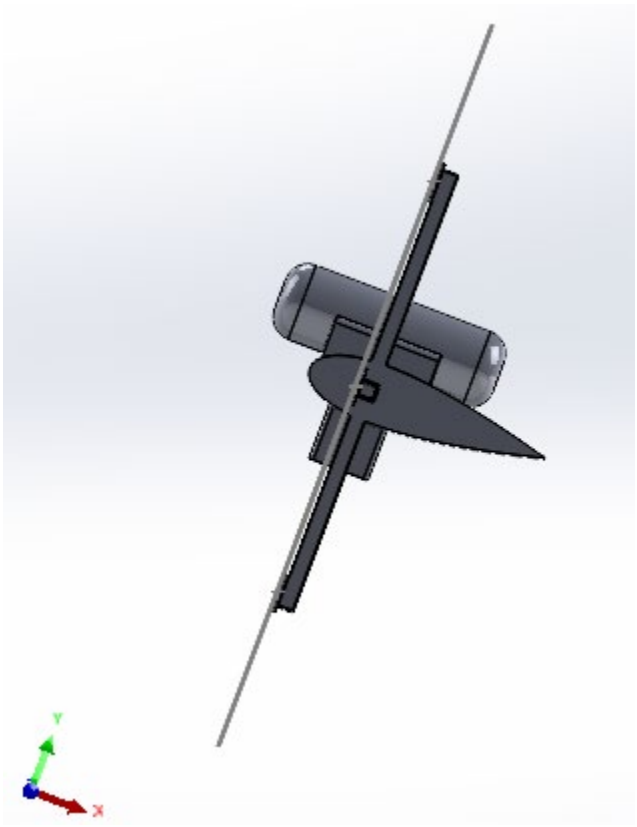

Figure 33. Bluff Body Flying Wing Forward Flight Configuration

D. CFD METHODS

1. Fluid Domain Creation

Bluff body models of the COTS platform and the Flying Wing were generated and cut out of fluid domains in SolidWorks. Since both craft are symmetric left to right, the domains were generated using a half-body to reduce computational load. Figure 34 shows zoomed in picture of the COTS half body fluid domain.

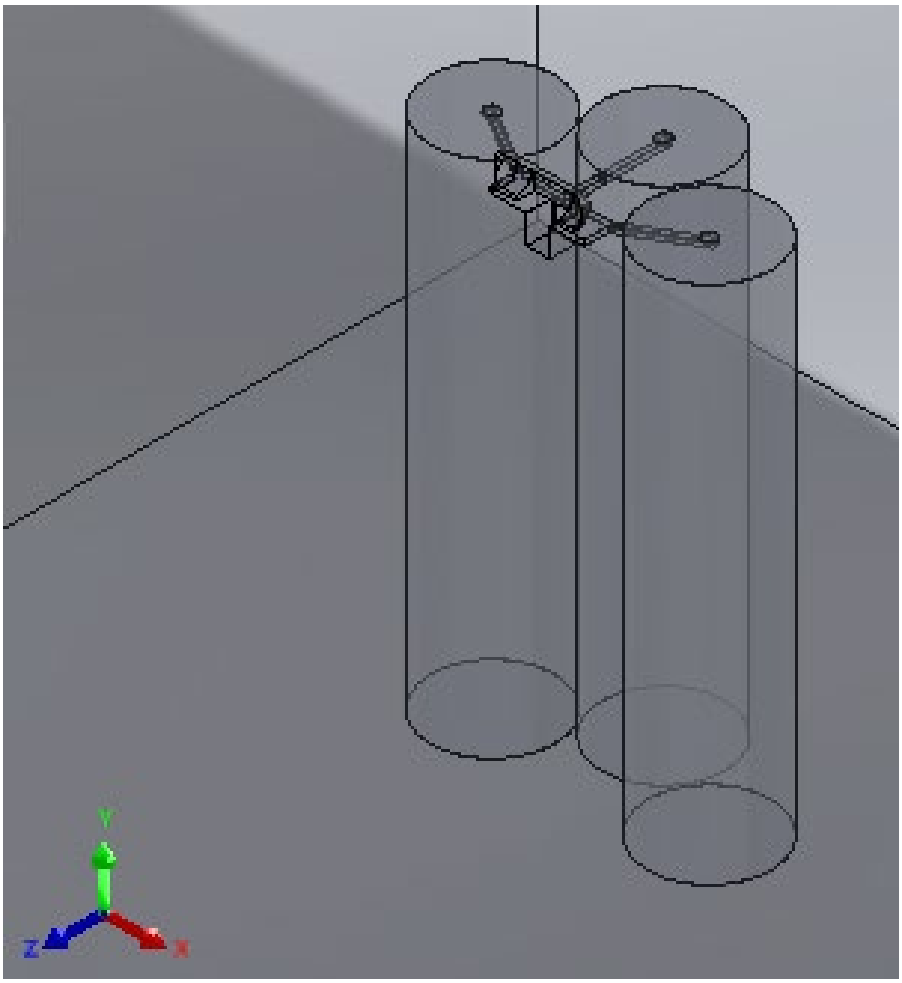

Figure 34. COTS Platform Fluid Domain

Both UAV fluid domains were large enough to ensure all actuator disks and body surfaces were 10 disk diameters away from any domain boundary that was not a symmetry plane. Figure 35 shows a zoomed in picture of the Flying Wing half body fluid domain.

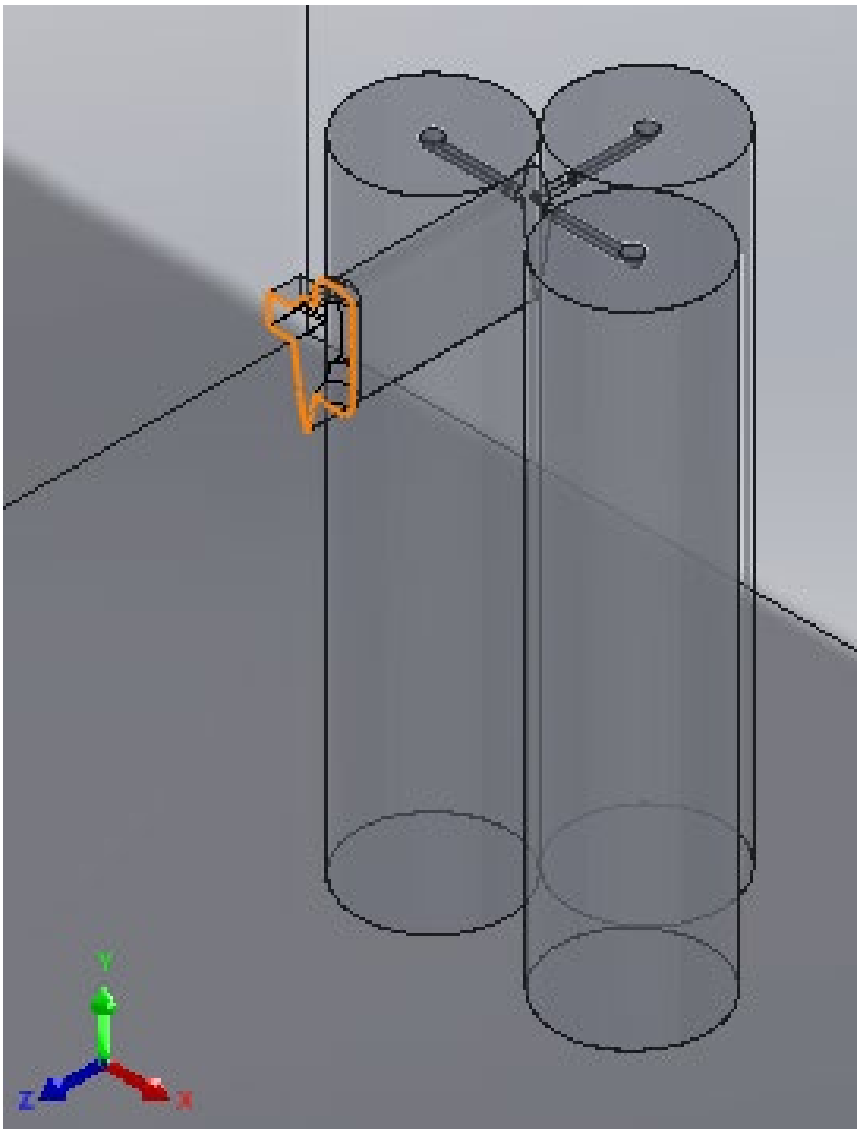

Figure 35. Flying Wing Fluid Domain

2. Meshing

For all simulations with a craft, half-body models with symmetry planes were used to reduce computational load.

a. COTS Platform

The same settings from the single disk in free space were used on the three actuator disks in the volume. In addition to those settings a 1 mm face sizing was inserted on the COTS platform body. The final mesh consisted of 11.1 million nodes and 62.6 million

elements. The CFD setup details and settings are included in Appendix F. Figure 36 shows the whole COTS fluid domain and mesh. Figure 37 shows a zoomed in picture of the mesh around the COTS platform.

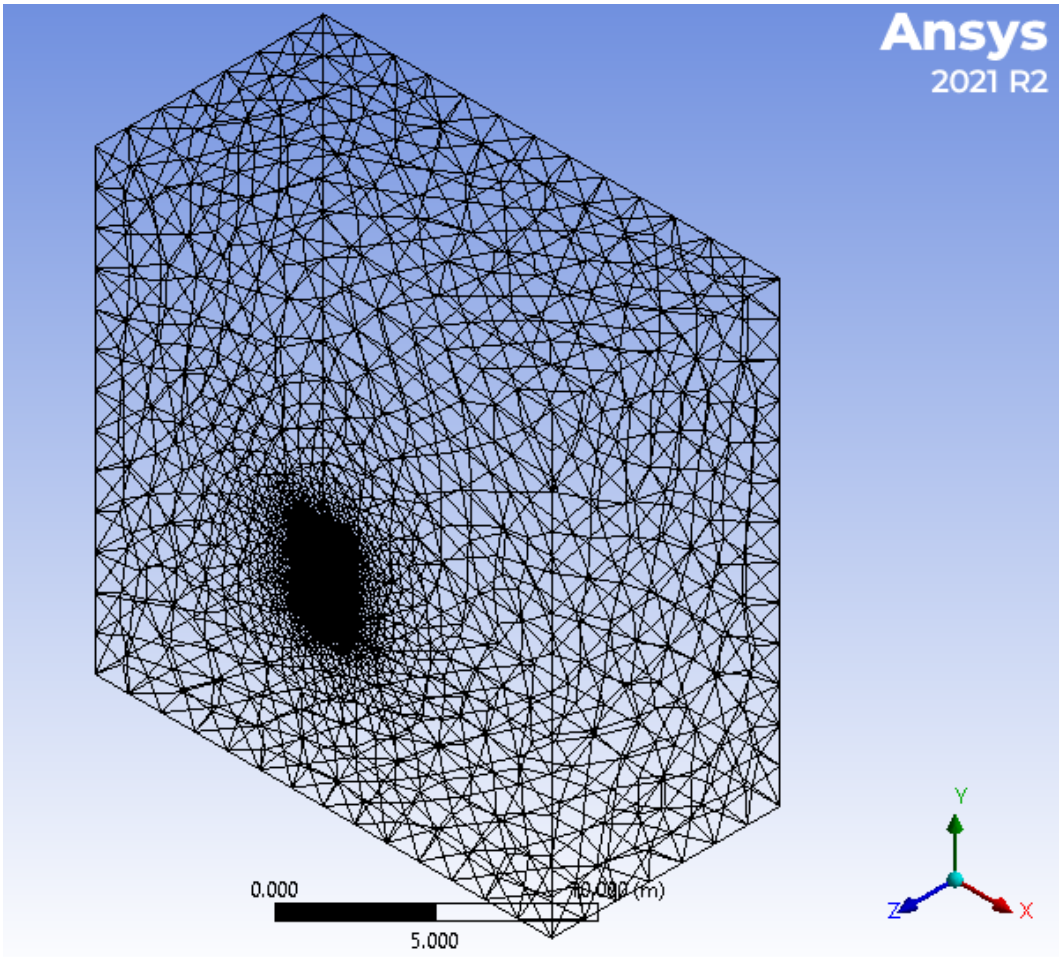

Figure 36. COTS Platform Mesh Volume

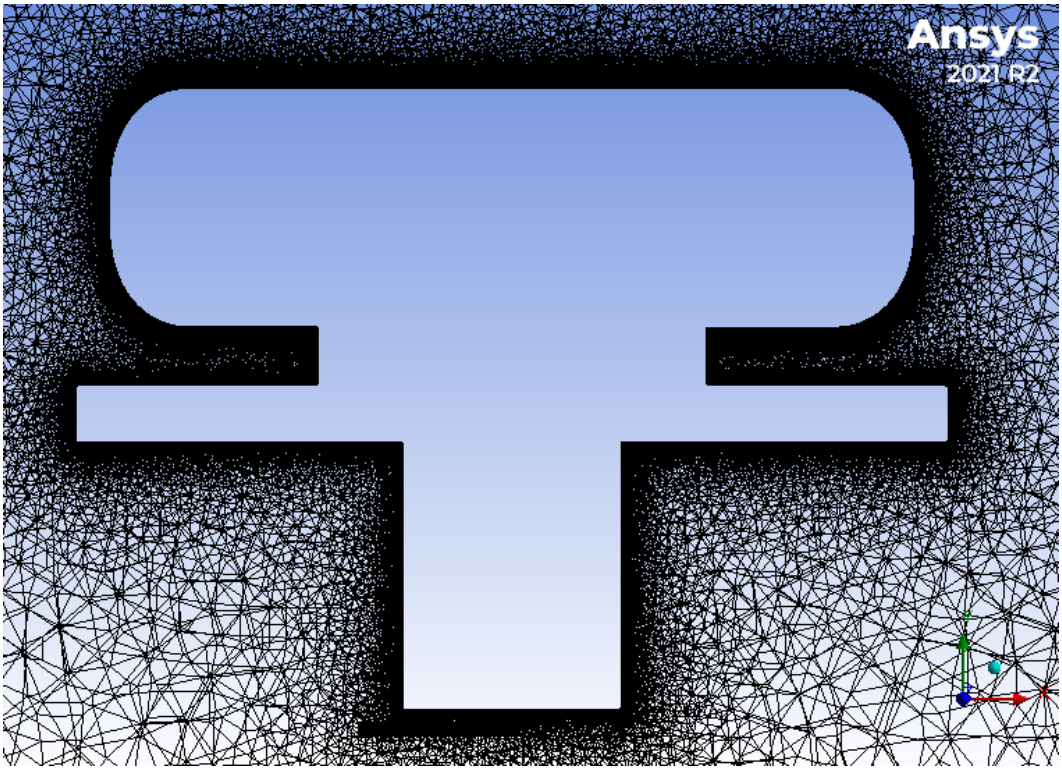

Figure 37. COTS Platform Body Mesh

b. Flying Wing

The same settings from the single disk in free space were used on the three actuator disks in the volume. In addition to those settings, a 2 mm face sizing and an inflation layer on the wing surface was inserted on the craft body. The final mesh consisted of 14.9 million nodes and 65.8 million elements. The CFD setup details and settings are included in Appendix G. Figure 38 shows a zoomed in picture of the mesh around the Flying Wing.

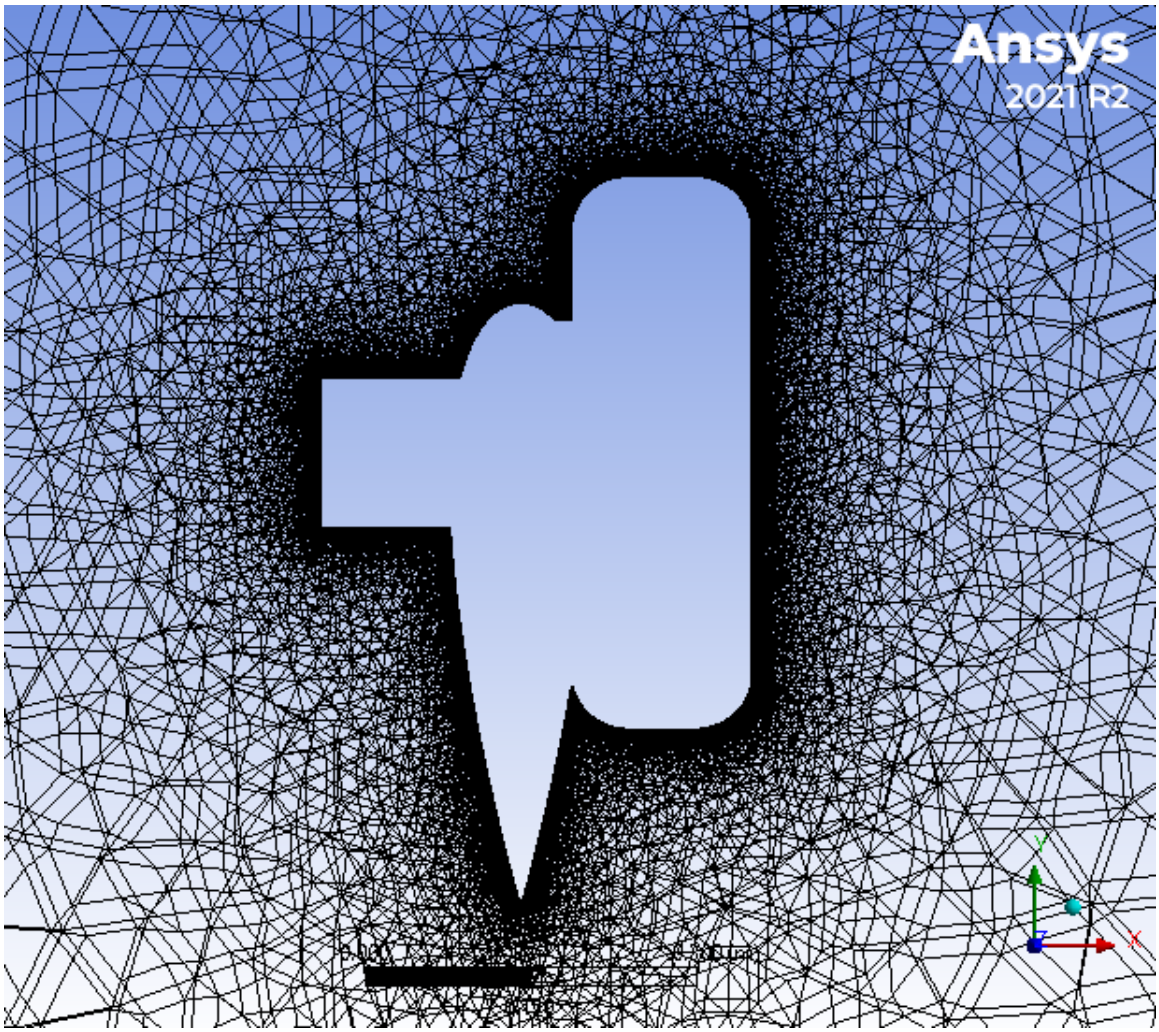

Figure 38. Flying Wing Body Mesh

The same setup modeling scheme used for single disk in free space was also utilized for the two UAV fluid domains.

E. RESULTS

1. COTS Platform

a. Hover Flight

The COTS platform hover model calculated a vertical force of 4.62 N. The fluid viscous effects produce a noticeable force in the vertical direction in hover that increases

the thrust per disk to 28.5 N. The calculated side force on the body is a negligible -0.06 N. Figure 39 shows the pressure distribution over the top surface of the COTS platform.

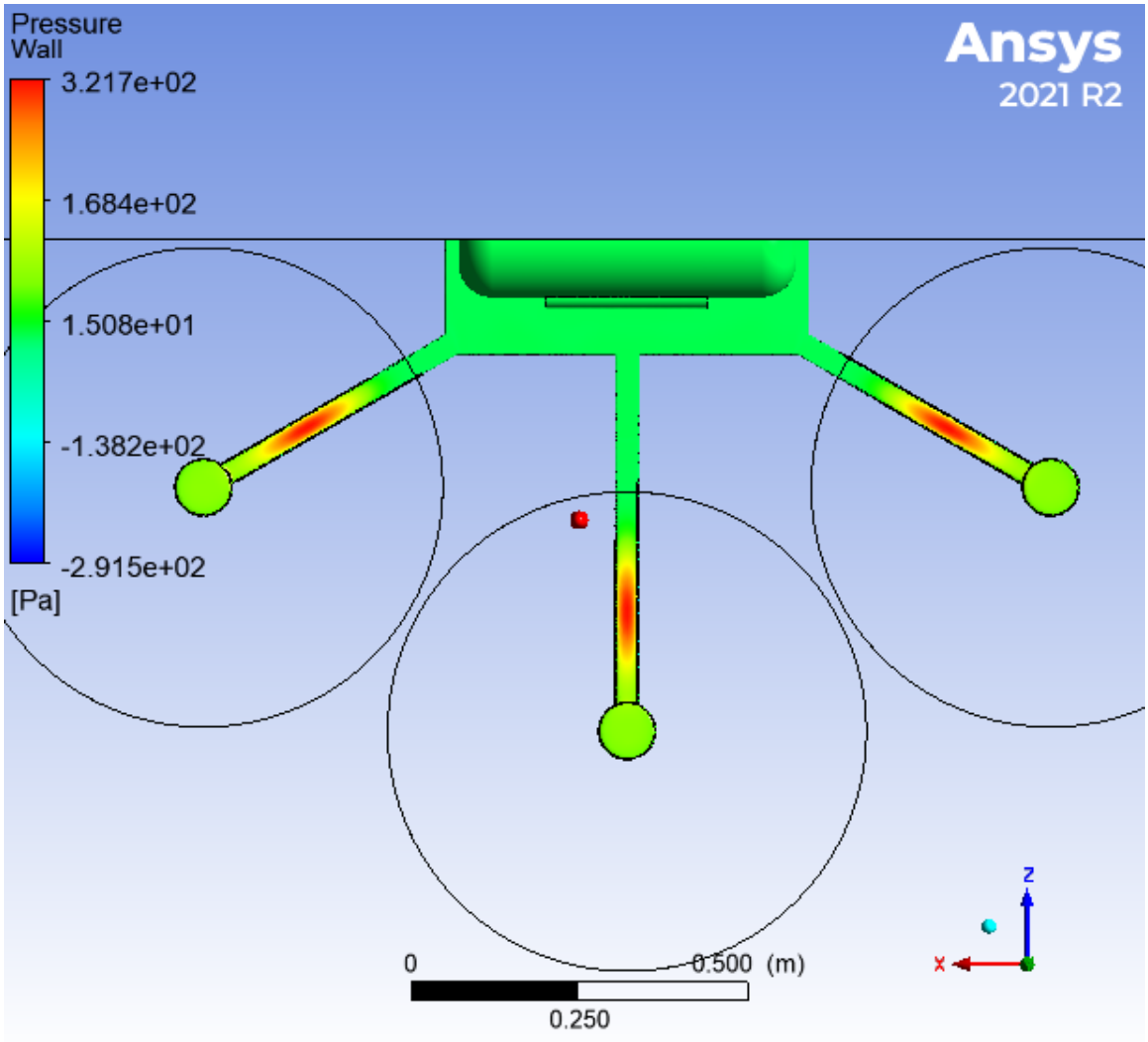

Figure 39. COTS Hover Pressure Distribution

The pressure distribution shows the arms experiencing the highest pressure. The maximum velocity induced by the disk is 11.0 m/s. Using the velocity term in Equation 1, dynamic pressure should be 71.1 Pa upon flow stagnation. The maximum pressure of 322 Pa shown in Figure 39 is most likely a flow effect like ground effect and significantly contributes to model drag. A rough calculation over the arms using an affected arm area of 0.0018 m^2 yields a pressure drag of 1.65 N from the arms alone. This result was discovered

too late in the modeling process to be investigated. The simulated ground effect is seen across all models containing walls with actuator disk flow. Models of the crafts without actuator disk flows for every external flow case was conducted for model error estimates.

For all models, the thrusts from the disk were obtained directly from the model by calculating the sum of the force in the y-direction across all disks. The hover model produced slightly more thrust than calculated. The peak radius was not adjusted between the single disk and multiple disks. The extra thrust could come from having multiple disks in the same vicinity. The effects of having multiple disks in the same vicinity without a craft present was not investigated in this thesis. Table 4 shows the expected and obtained thrust from the simulations.

Table 4. COTS Platform Hover Thrust

Expected Total Thrust	85.5 N
Expected Thrust per Disk	28.5 N
Total Thrust Obtained	87.9 N
Thrust Obtained per Disk	29.3 N

Figure 40 shows the COTS hover streamlines. Figure 40 shows the same heavy entrainment of flow through the three disks. In addition, the streamlines also show regions of spiraling flow from wall interactions. Using the drag calculated by the model, the expected thrust is shown in Table 4 against the sum of the thrusts from the disks.

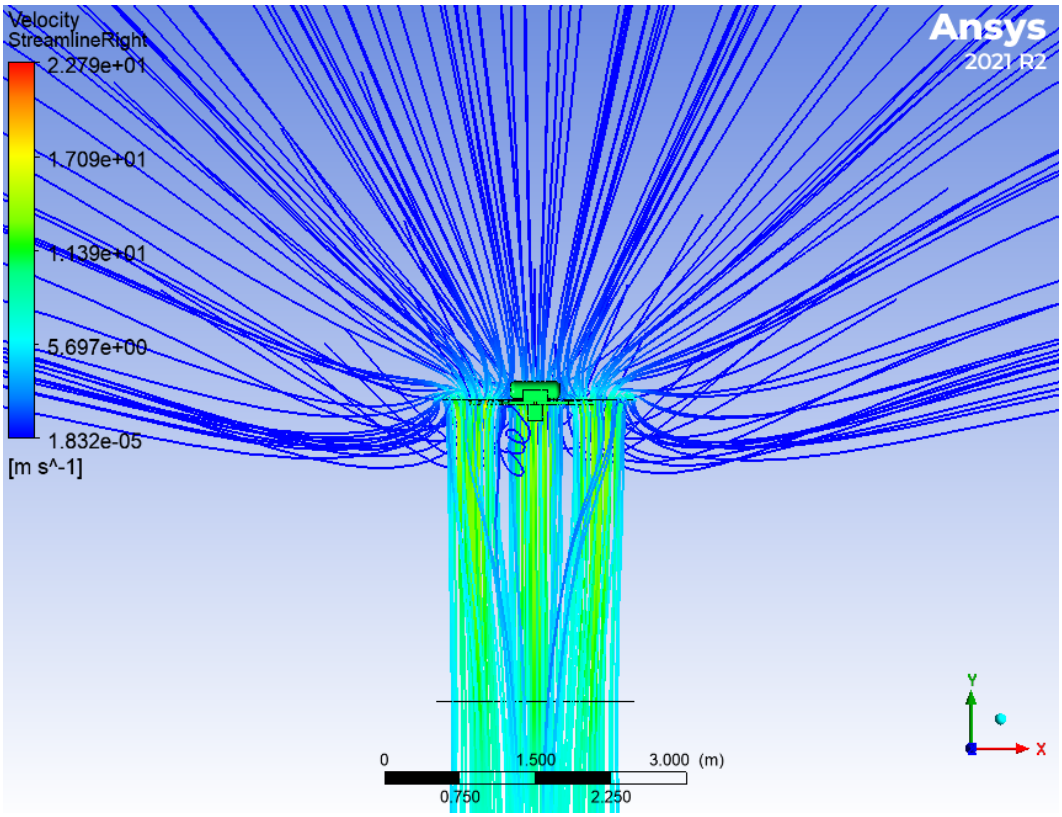

Figure 40. COTS Hover Streamlines

b. Vertical Flight

The drag force for the COTS platform with and without actuator disk flows were 7.68 N and 0.37 N respectively. The large difference between external flow only and external with actuator flows is mostly due to the large pressures exerted on the arms and motors also seen in the hover model. In vertical climbing flight, the side force from the platform is not really a factor. The side force with and without actuator disk flows were -0.07 N and 0.00 N. The COTS platform model in vertical flight predicted a thrust of 29.5 N needed to maintain vertical climb. The model only produced 25.6 N per disk. One reason for the difference could be that the model needs to be tweaked when transitioning to different stages of flight. The peak radius location is most likely not the same for hover and vertical flight. Another possibility derives from the disk proximities. Since the stream tubes are close to each other, the tubes do not contract as much which drags less flow through the disk per unit energy expended. A follow-on study should be conducted on to see if this

effect exists for multiple disks in vicinity of each other. Table 5 shows the expected and obtained thrust from the simulations.

Table 5. COTS Vertical Climb Thrust

Expected Total Thrust	88.5 N
Expected Thrust per Disk	29.5 N
Total Thrust Obtained	76.8 N
Thrust Obtained per Disk	25.6 N

Figure 41 shows the streamlines from flow simulations with and without actuator disks. Figure 41 shows the streamlines for vertical flight with and without actuator flows. All streamlines shown in the model with actuator flows pass through the actuator disks. The large separation region is affected by the presence of actuator flows which provides evidence that modeling these flows is important to quantifying craft performance. The large separation region beneath the main body is expected and contributes to the increased thrust needed by the craft.

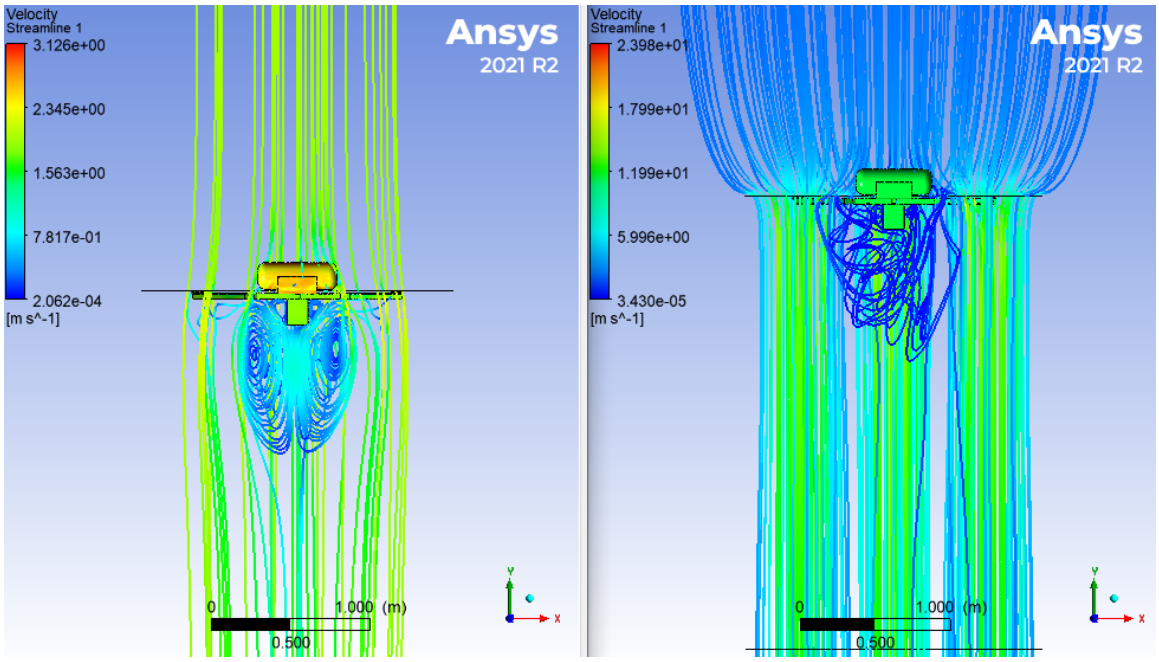

No Actuator Disks (left) and Actuator Disks (right)

Figure 41. COTS 2 m/s Vertical Climb Streamlines

Figure 42 shows the differences in pressure on the upper surfaces of the platform with and without the actuator disk flows. With actuator flows present, all external flow forces exerted on the main body are masked by the pressures exerted on the arms and motors. This is the expected result due to the flow effect seen in the hover model. The scales used for color shading are significantly different for the two cases modeled.

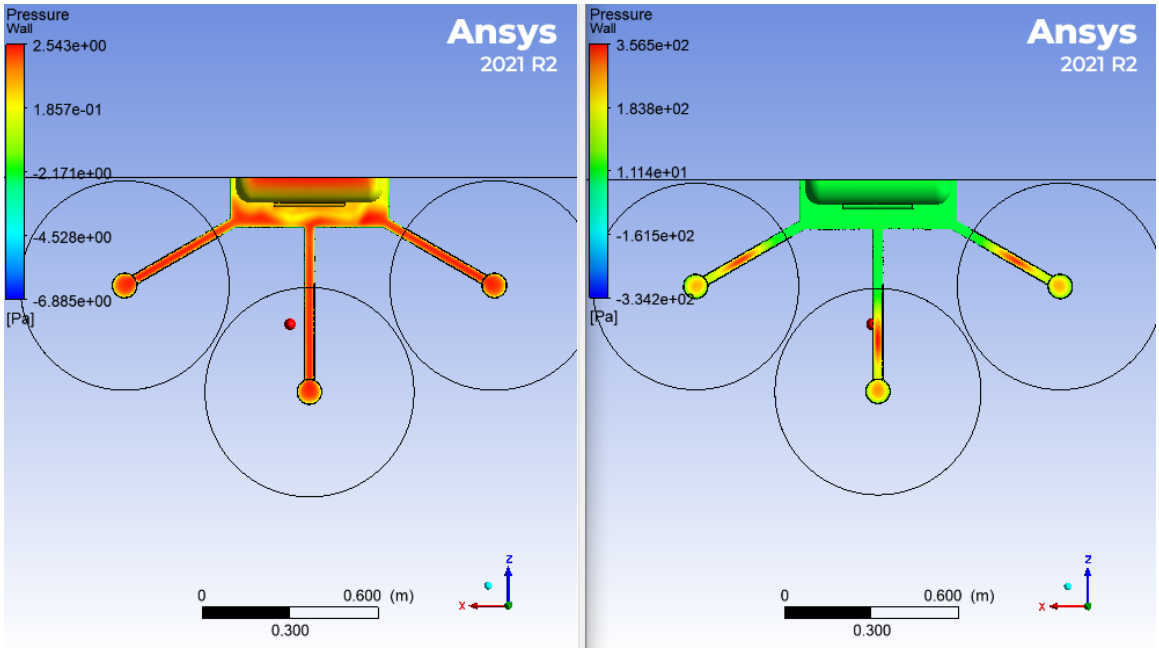

No Actuator Disks (left) and Actuator Disks (right)

Figure 42. COTS 2 m/s Vertical Climb Pressure Distributions

c. Forward Flight

For forward flight the thrust vector is tilted due to lift and drag forces being defined by the incoming airflow. Figure 43 shows the force balance with the incoming airflow for the COTS platform. The incoming airflow was rotated instead of rotating the craft for ease of simulation. The chord AoA, ϵ, is equal to the Actuator Disk AoA, α, for the COTS platform. Figure 43 shows an example forward flight force balance.

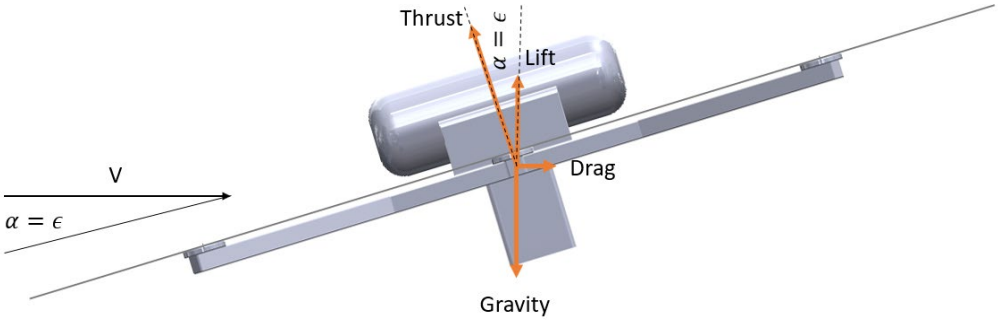

Figure 43. Example COTS Forward Flight Force Balance

Across all forward flight models, the thrust produced was significantly less than the expected thrust calculated indicating the models need adjustment. A limited analysis can be conducted on the force trends; however, the raw data is overly conservative due to the high pressures seen on the arms and motors and produced thrust underperformance.

Figure 44 shows the trend in the lift and drag forces for the modeled forward flight cases. The COTS platform had nearly 0 lift in all external flow only cases except for the 15 m/s case. This result was initially unexpected, but shows the small body primarily acts a blunt body instead of a wing with drag forces relatively independent of external flow AoA. The large frontal area of the fuel cell causes a large separation region behind it. That low pressure region appears to be countering the expected negative lift of the craft over the lower speed regimes. When actuator flows are modeled, the lift forces are all negative. There is a reduction in negative lift over the lower speeds modeled. Further modeling and analysis need to be conducted to confirm these results. The raw CFD data and graphing code for the force trends is provided in Appendix H.

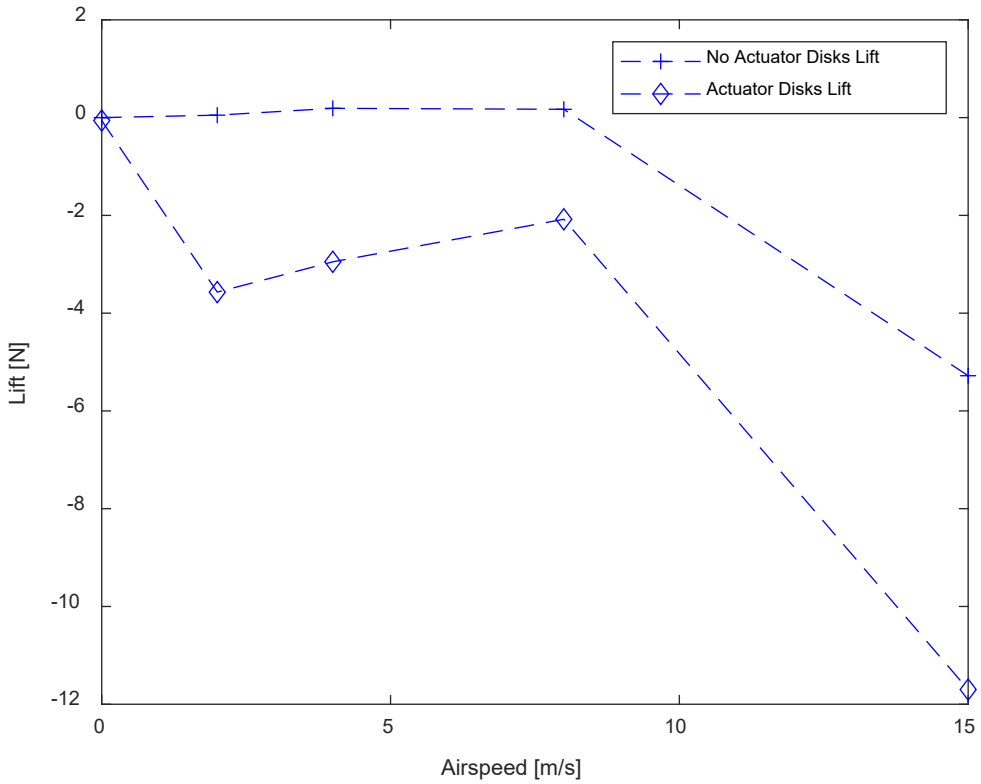

Figure 44. COTS Lift versus Airspeed

Figure 45 shows the trend in drag forces rise with airspeed in all cases except the transition from hover to forward flight when actuator flows are modeled. This is most likely due to the modeled flow effect seen on the arms and motors produced by the Actuator Disk.

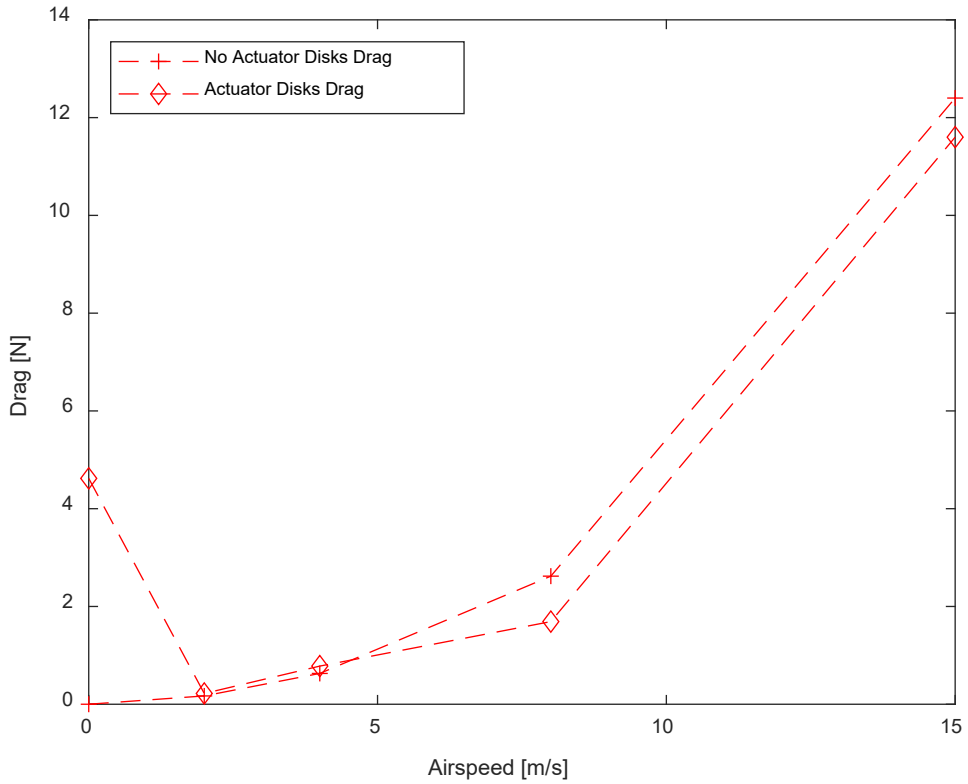

Figure 45. COTS Drag versus Airspeed

Figure 46 shows the predicted thrust trends for the modeled cases. The data point at 0 m/s airspeed is the expected hover thrust obtained from the hover model. The predicted thrusts drop over the lower speeds modeled, then rise back to approximately hover thrust at the highest speed modeled. This result is unexpected, but trends with the reduction in negative lift and low drag seen across the lower speeds in Figure 44.

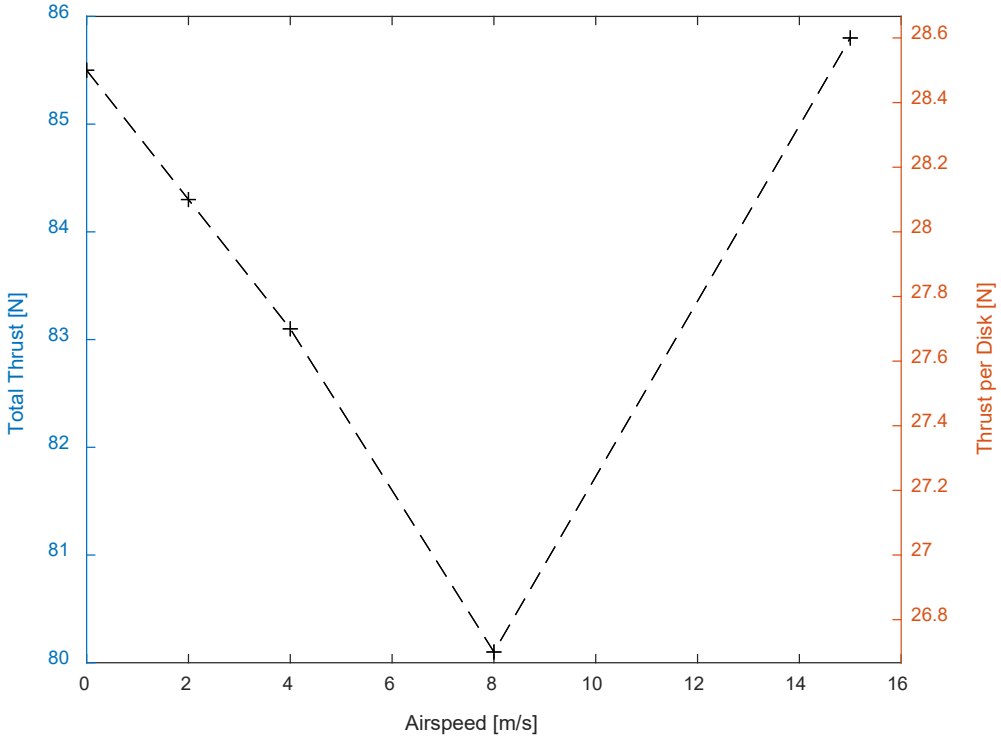

Figure 46. COTS CFD Predicted Thrust Results

Figure 47 shows the pressures exerted on the platform in forward flight with and without actuator flows. The arms and motors continue to overshadow the external flow forces on the body. This effect was seen across all forward flight models.

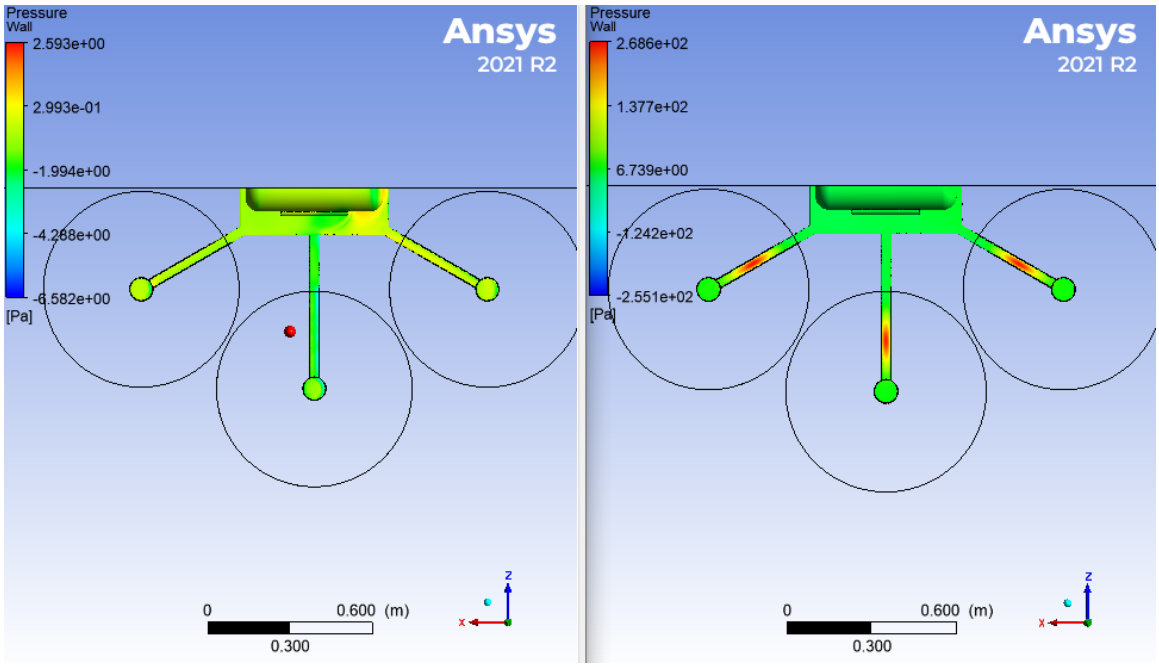

No Actuator Disks (left) and Actuator Disks (right)

Figure 47. COTS 2 m/s 4° ϵ Pressure Distributions

Figures 48 through 51 show the streamlines from the various airspeeds and Actuator Disk AoA modeled. In general, as speed and AoA increase, less stream tube contraction and flow redirection occur. At 8 m/s airspeed, the streamlines show hardly any stream tube contraction or change in flow direction. At 15 m/s airspeed, there appears to be no stream tube contraction or redirection of the flow through the disks. On all streamline figures, the direction of forward flight is shown by the incoming streamlines.

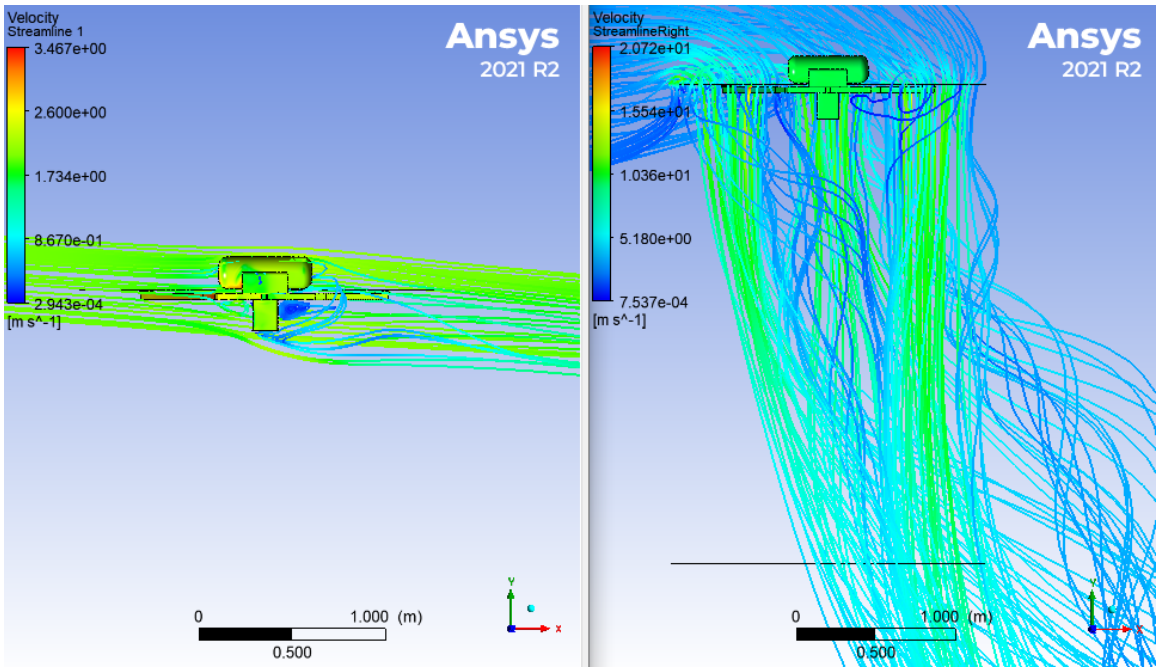

No Actuator Disks (left) and Actuator Disks (right)

Figure 48. COTS 2 m/s 4° ϵ Streamlines

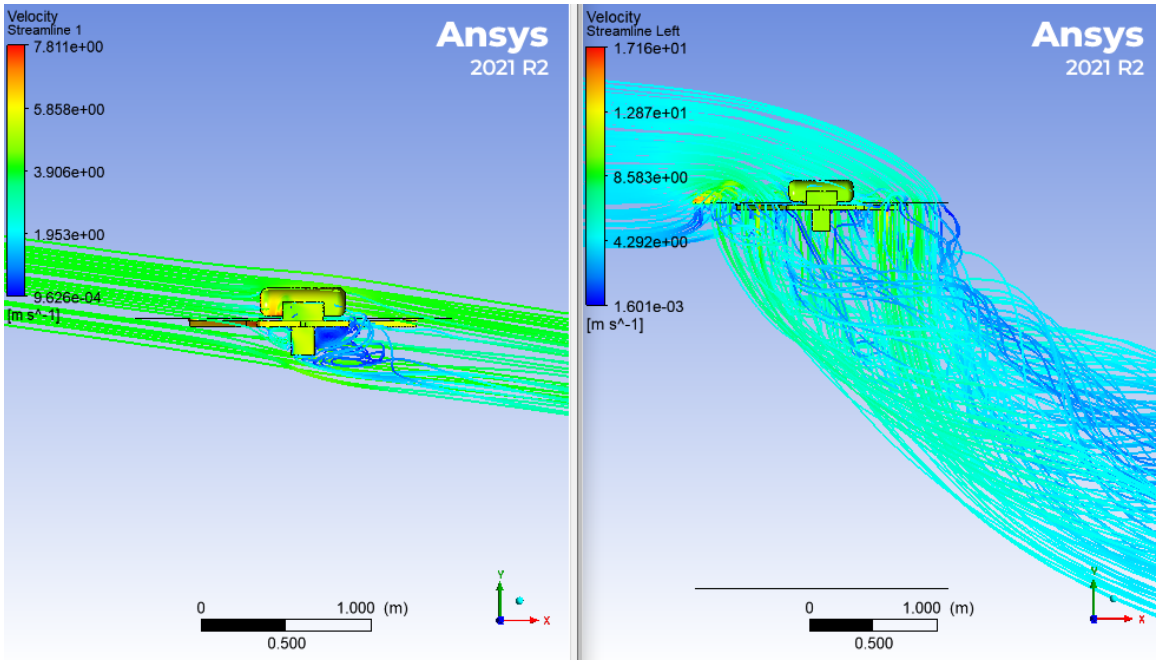

No Actuator Disks (left) and Actuator Disks (right)

Figure 49. COTS 4 m/s 8° ϵ Streamlines

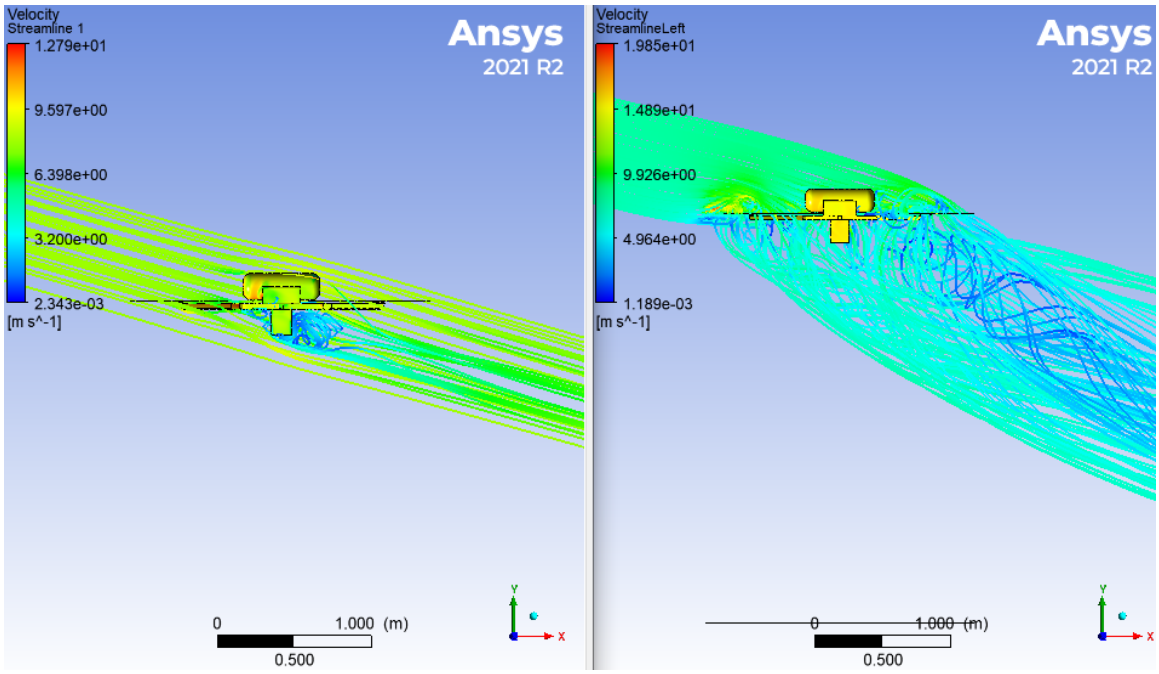

No Actuator Disks (left) and Actuator Disks (right)

Figure 50. COTS 8 m/s 16 ° ϵ Streamlines

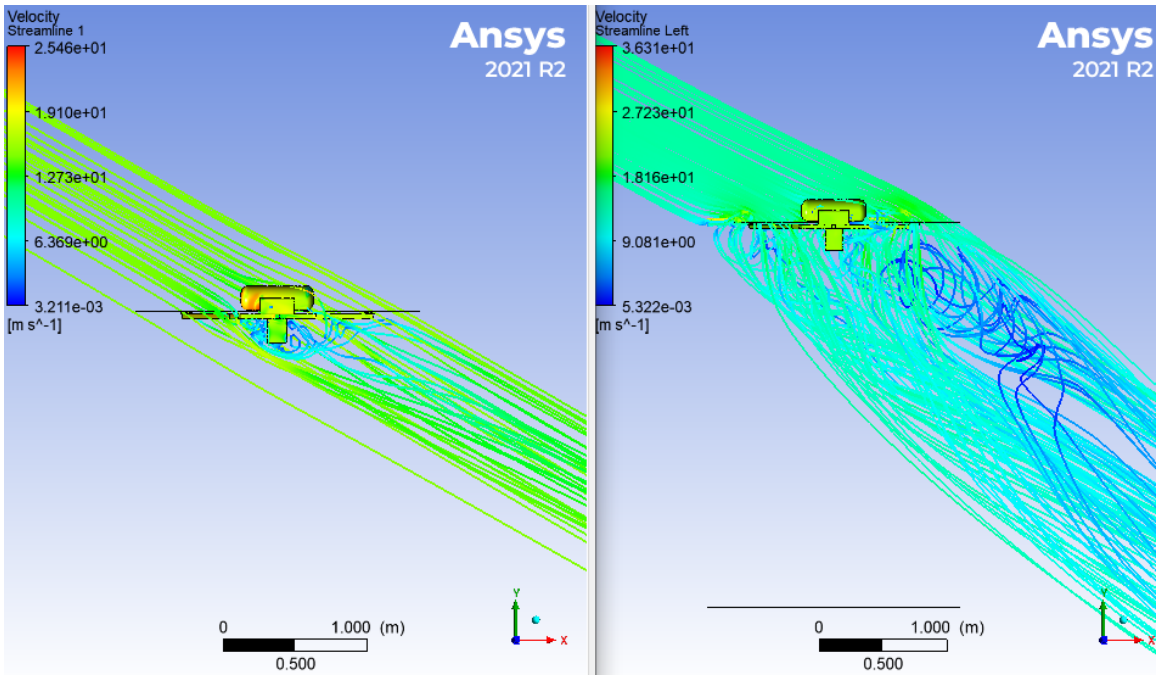

No Actuator Disks (left) and Actuator Disks (right)

Figure 51. COTS 15 m/s 30° ϵ Streamlines

2. Flying Wing

a. Hover Flight

The Flying Wing model predicts increased aerodynamic effects on the craft body and shows more thrust is needed to maintain hover flight. The Flying Wing hover model calculated a drag force of 4.47 N. The fluid viscous effects produce a noticeable force in the vertical direction in hover that increases the thrust per disk to 28.5 N. This was the same increase seen in the COTS hover model. The calculated side force on the body is negligible like the COTS hover model at -0.03 N. Figure 52 shows the hover pressure distribution over the top surface of the COTS platform.

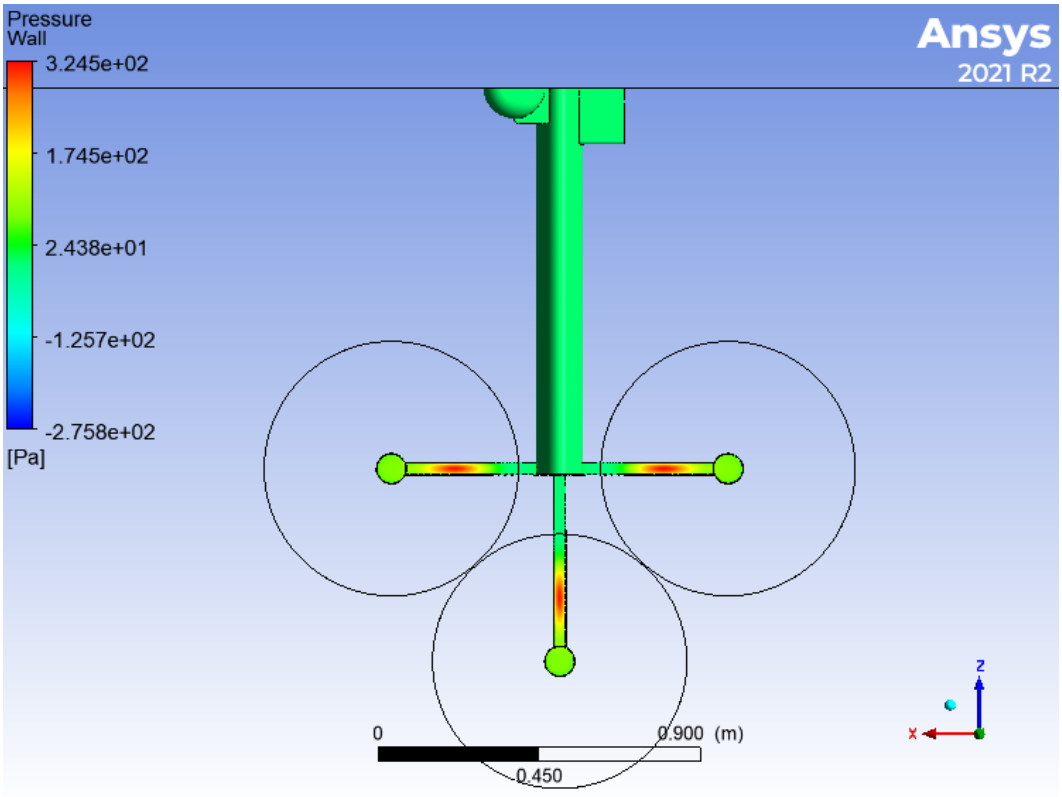

Figure 52. COTS Hover Pressure Distribution

The pressure distribution shows the same high pressure on the arms seen in the COTS hover model. Table 6 shows the expected and obtained thrust from the simulations.

Table 6. Flying Wing Hover Thrust

Expected Total Thrust	85.5 N
Expected Thrust per Disk	28.5 N
Total Thrust Obtained	88.3 N
Thrust Obtained per Disk	29.4 N

The thrust produced by the model is higher than the thrust produced by the COTS hover model. The larger produced thrust could be a result of the disks being further from the symmetry plane and the model may need to be adjusted. The increased distance could allow more flow to be contracted and entrained. Another reason could be the space between the disks is smaller in the Flying wing design. The tighter spacing could entrain more flow and cause larger thrusts for the same velocity distributions than the COTS design. Figure 53 shows the hover streamlines. Figure 53 shows the heavy disk entrainment and stream tube contraction for the Flying Wing in hover.

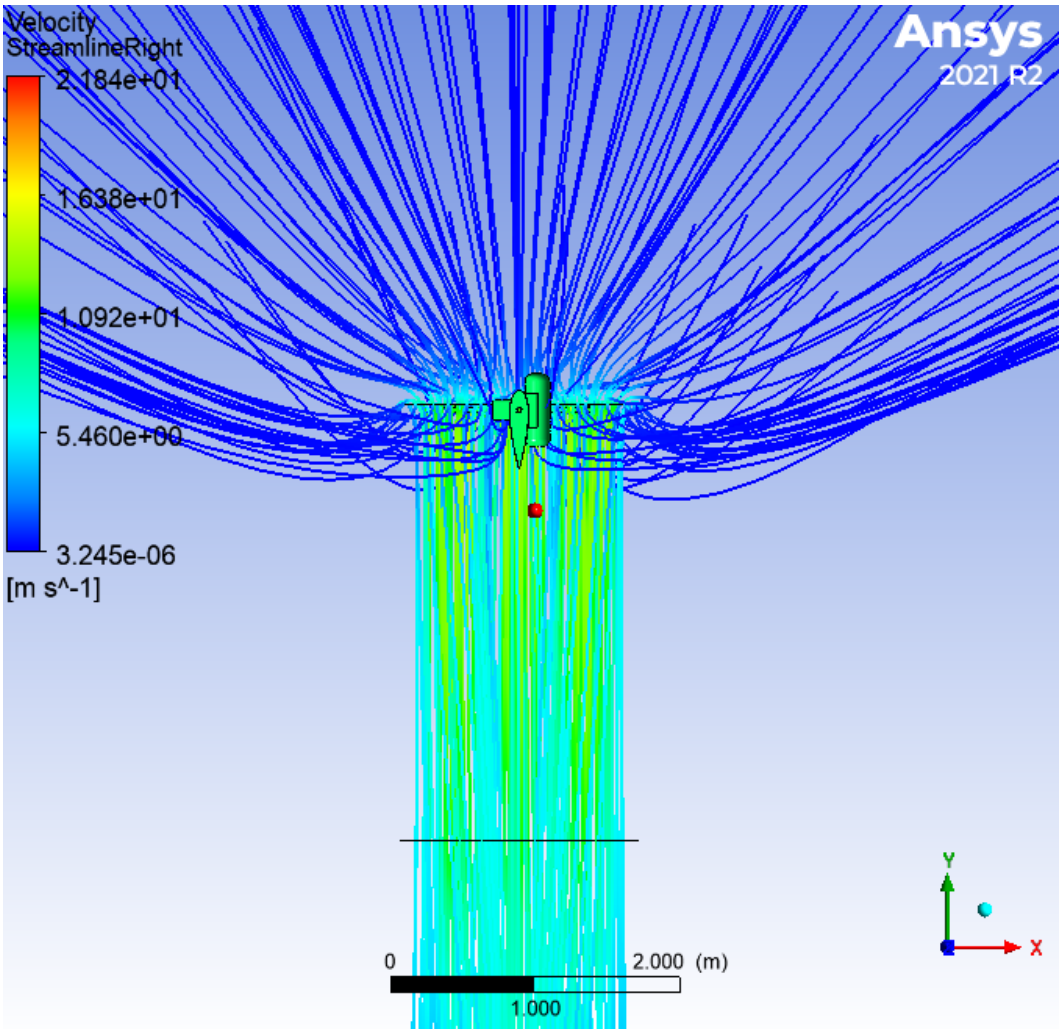

Figure 53. Flying Wing Hover Streamlines

b. Vertical Flight

The force in the vertical direction and side force for the Flying Wing with and without actuator disk flows were 9.68 N and 0.37 N respectively. The large difference between external flow only and external with actuator flows is mostly due to the modeled flow effect in the hover model. In vertical climbing flight, the lift from the platform is not really a factor due to the chosen airfoil's symmetry. The lift force with and without actuator disk flows were 0.49 N and 0.13 N. The Flying Wing model in vertical flight predicted a thrust of 28.5 N needed to maintain vertical climb. The model produced 29.4 N per disk. The tighter disk configuration could be one reason for the difference. Since the stream

tubes are closer to each other and further away from the symmetry plane, the tubes can contract more which drags more flow through the disk. Table 7 shows the expected and obtained thrust from the simulations.

Table 7. Flying Wing Vertical Climb Thrust

Expected Total Thrust	85.5 N
Expected Total Thrust per Disk	28.5 N
Total Thrust Obtained	88.3 N
Thrust Obtained per Disk	29.4 N

Figure 54 shows the streamlines for vertical flight with and without actuator flows. The model with no actuator disk flows shows the same separation region seen behind the fuel cell seen in COTS forward flight models. The separation region is still affected by the presence of actuator flows despite the increased distance of the actuator disks from the fuel cell and tank. This result provides further evidence that modeling these flows is important to quantifying craft performance. All streamlines from external and actuator flow models pass through the actuator disks.

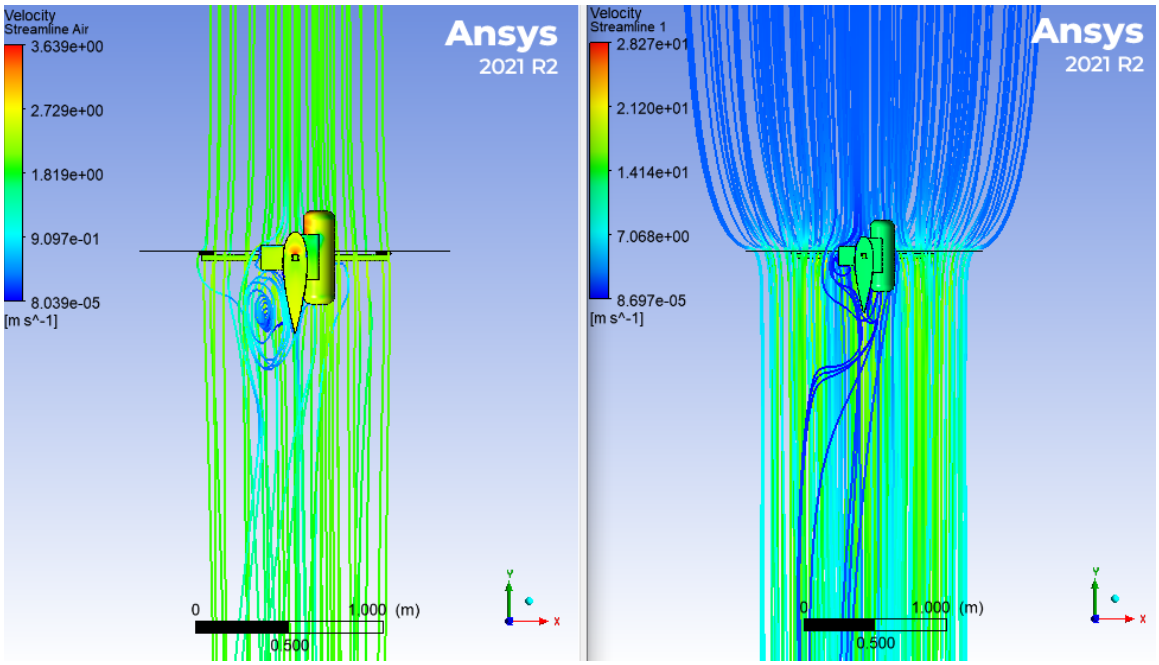

No Actuator Disks (left) and Actuator Disks (right)

Figure 54. Flying Wing 2 m/s Vertical Climb Streamlines

c. Forward Flight

The main difference between the COTS and Flying Wing is the chord AoA for the external airflow. Figure 55 shows an example forward flight force balance for the Flying Wing. For the Flying Wing, $\epsilon = 90° - \alpha$ which is shown in Figure 55.

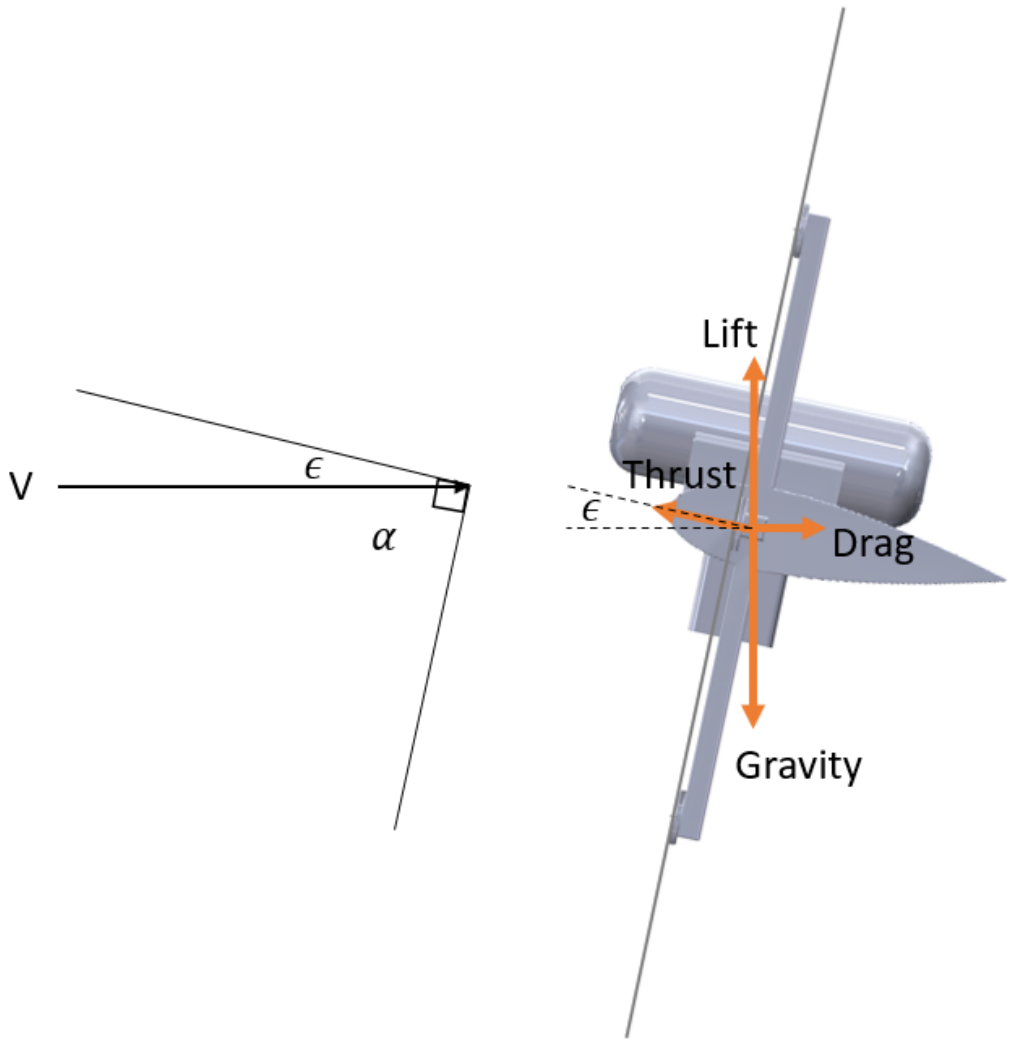

Figure 55. Example Flying Wing Force Balance

For the Flying Wing forward flight models, the thrust produced was much closer to the expected thrust calculated. Still only a limited analysis can be conducted on the force trends due to the conservative nature of the raw data and simulated ground effect.

Figure 56 shows the trend in the lift forces for the modeled forward flight cases. The Flying Wing had insignificant lift until external flow reached 8 m/s. The introduction of actuator flows also decreased the lift produced by the craft. This result is most likely a model limitation due to the ground effect seen on the arms and motors of the craft. The raw CFD data and graphing code for the force trends is provided in Appendix H.

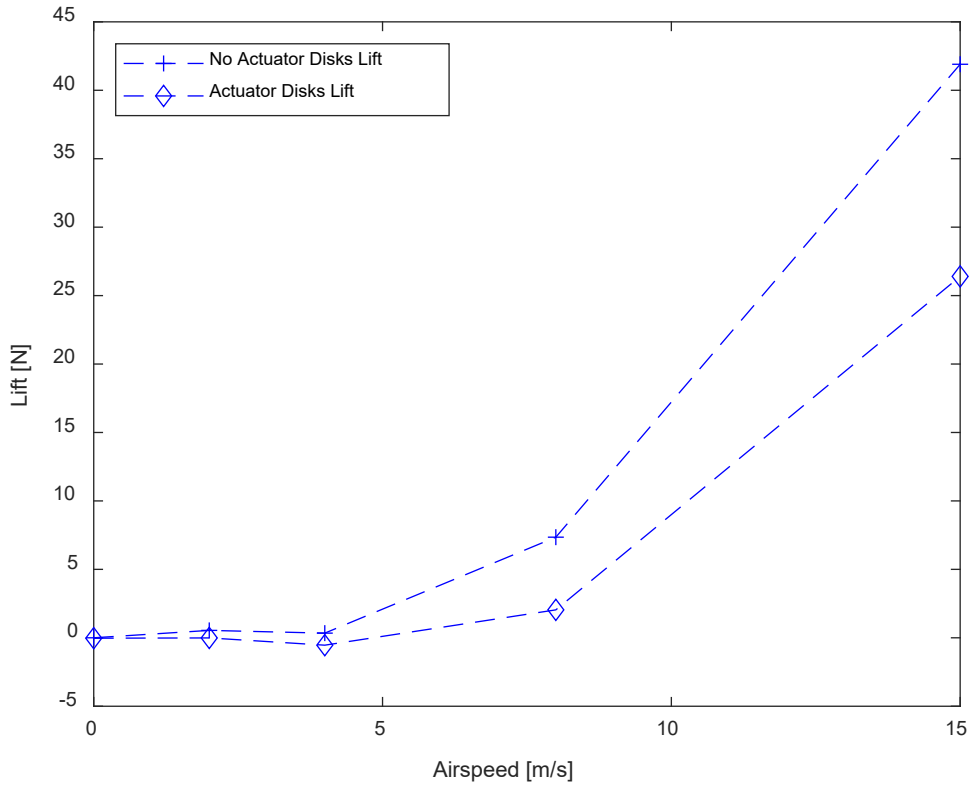

Figure 56. Flying Wing Lift versus Airspeed

Figure 57 shows the trend in drag forces rise with airspeed in all cases except the transition from hover to forward flight when actuator flows are modeled. Drag with actuator flows is always higher than the external flow alone. This is expected due to the increased flow seen near a no slip surface. The difference between the two is most likely larger than actual present in reality because of the modeled flow effect.

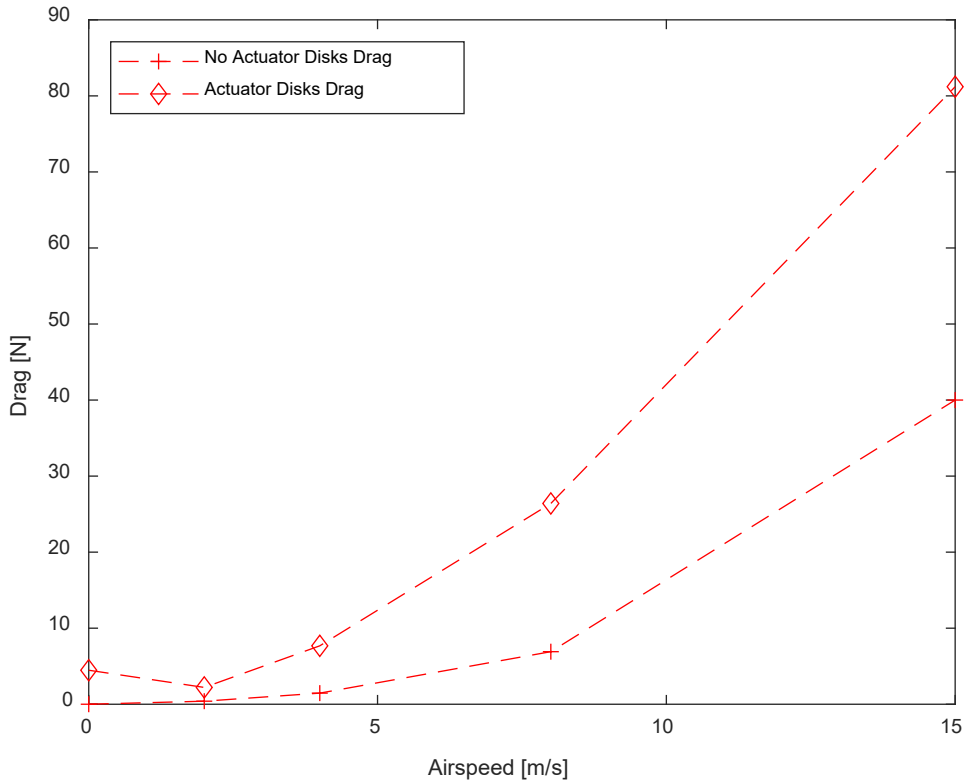

Figure 57. Flying Wing Drag versus Airspeed

Figure 58 shows the predicted thrust trends for the modeled cases. Once again, the data point at 0 m/s is the expected hover thrust obtained from the hover model. The Flying Wing had a significant reduction in thrust from hover to forward flight. This reduction in required thrust means less power is required to maintain the craft in flight. A minimum is seen at the 4 m/s case modeled. When referencing Figure 31, the maximum lift to drag ratio for the NACA 0024 airfoil is seen at 8° and the 4 m/s case had a chord AoA of 8°. For the maximum combination of true airspeed and chord AoA, the Flying Wing model has significant increases in lift and drag which requires more thrust. An investigation into maintaining the chord AoA at 8° and varying airspeed should be investigated further but was not conducted due to time constraints.

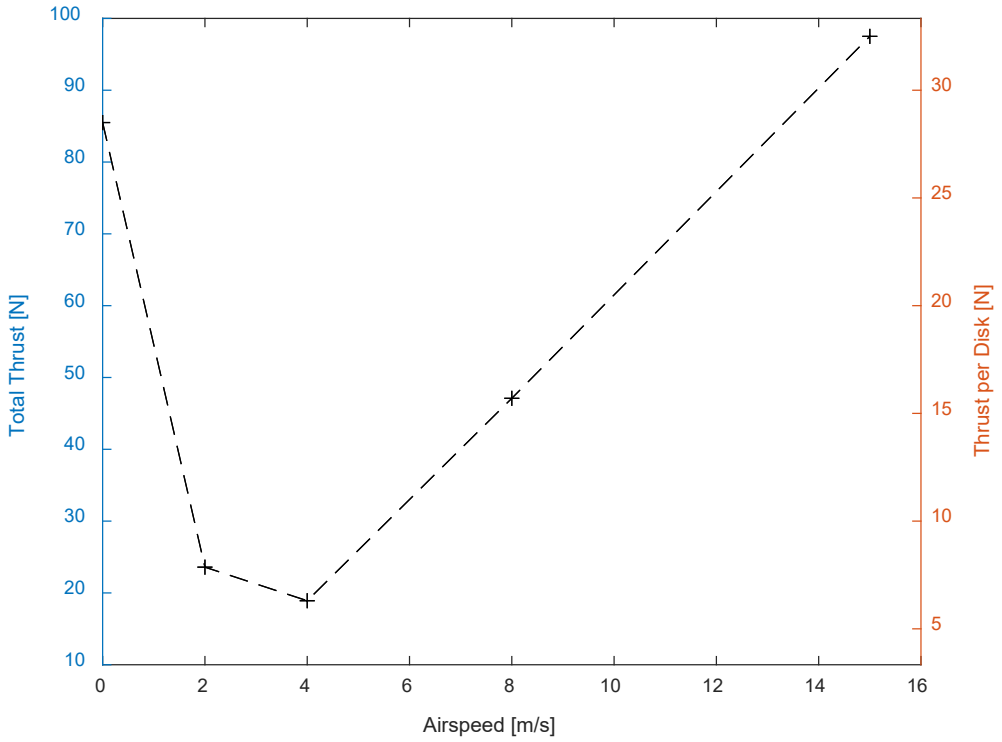

Figure 58. COTS CFD Predicted Thrust Results

Figure 59 shows the pressures exerted on the body in forward flight in simulation with and without actuator disks. The arms and motors continue to overshadow the external flow forces on the body when actuator flows are modeled. This effect was seen across all forward flight models.

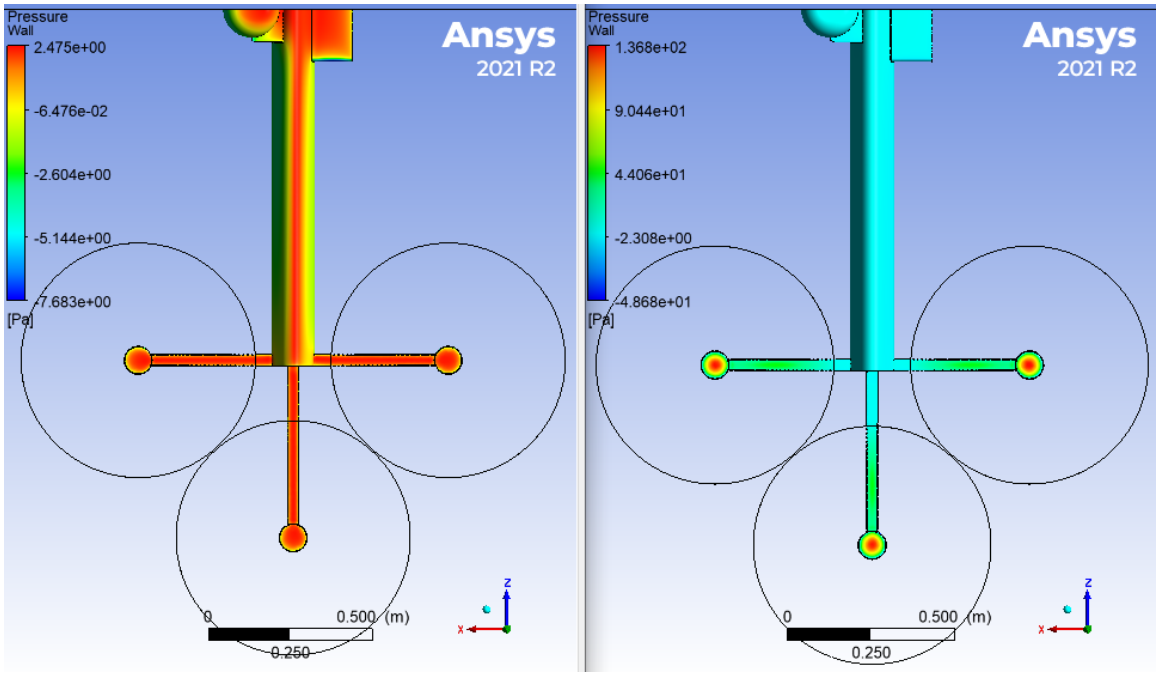

No Actuator Disks (left) and Actuator Disks (right)

Figure 59. COTS 2 m/s 4° ϵ Pressure Distributions

Figures 60 through 64 show the streamlines with increasing chord AoA. In general, the Flying Wing design did a better job at producing the expected thrust and maintaining flow redirection through the disks. The better performance is attributed to better alignment of the flow perpendicular with the disk surface. In all streamline figures, the direction of forward flight is indicated by the incoming streamlines.

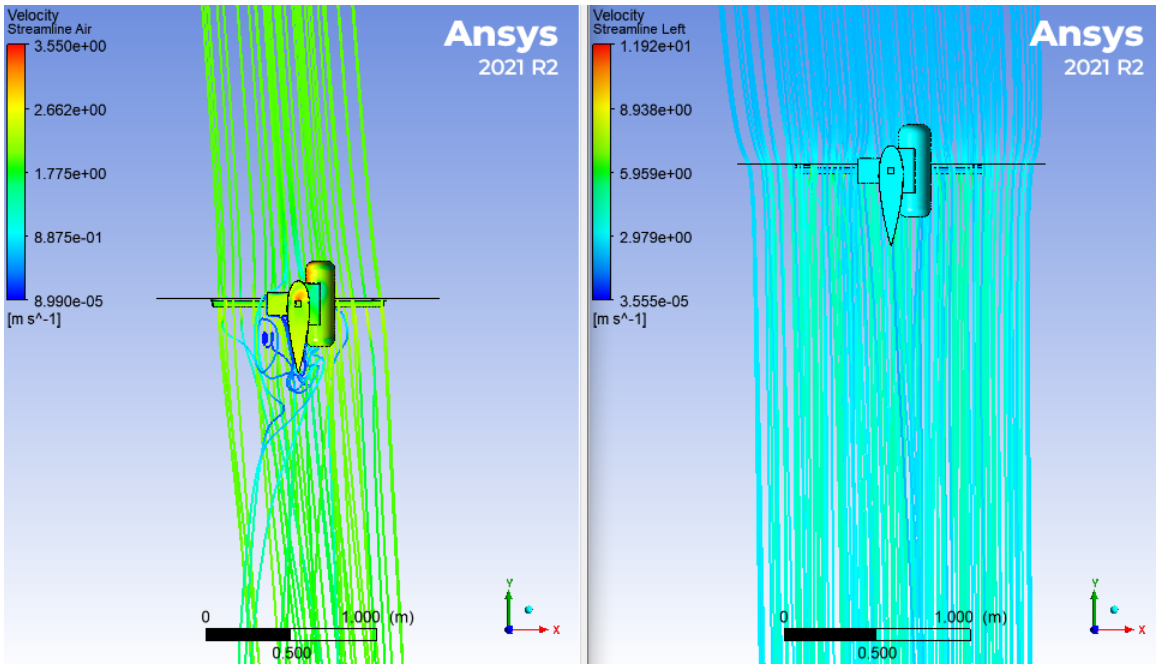

No Actuator Disks (left) and Actuator Disks (right)

Figure 60. Flying Wing in 2 m/s 4° ϵ Streamlines

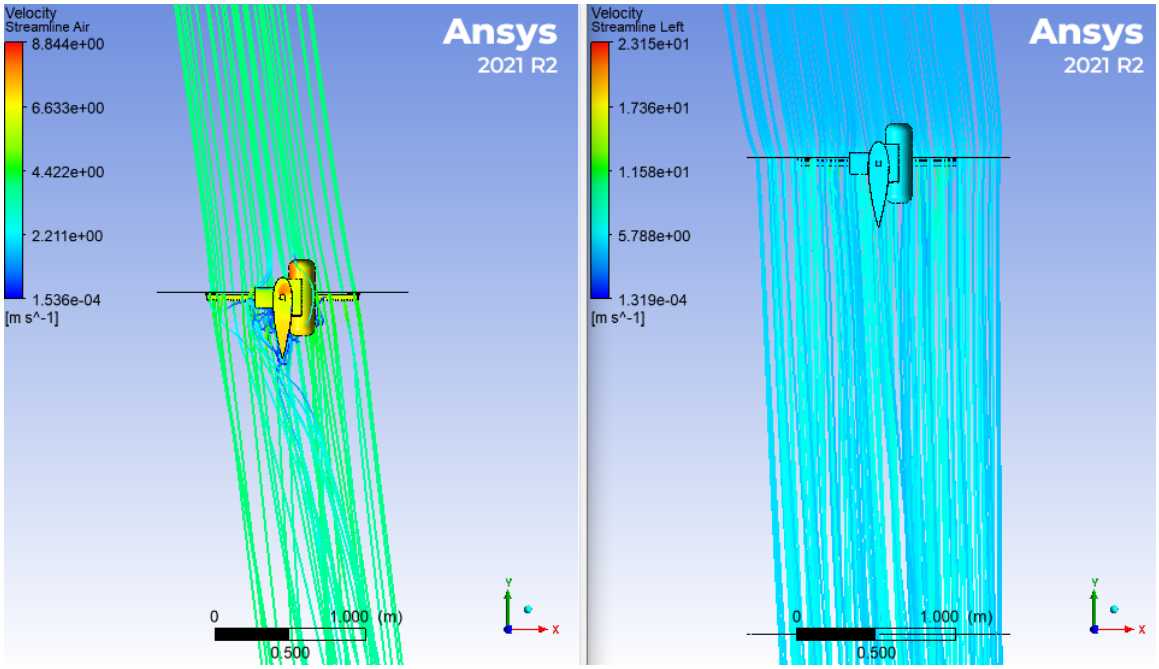

No Actuator Disks (left) and Actuator Disks (right)

Figure 61. Flying Wing in 4 m/s 8° ϵ Streamlines

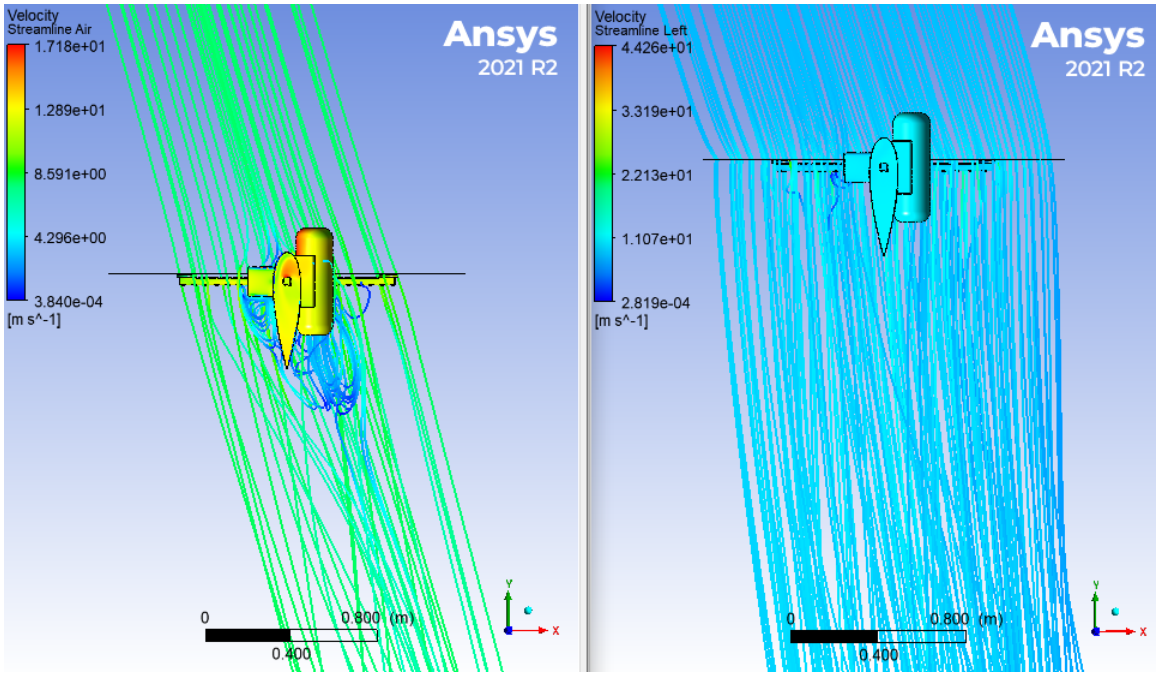

No Actuator Disks (left) and Actuator Disks (right)

Figure 62. Flying Wing in 8 m/s 16° ϵ Streamlines

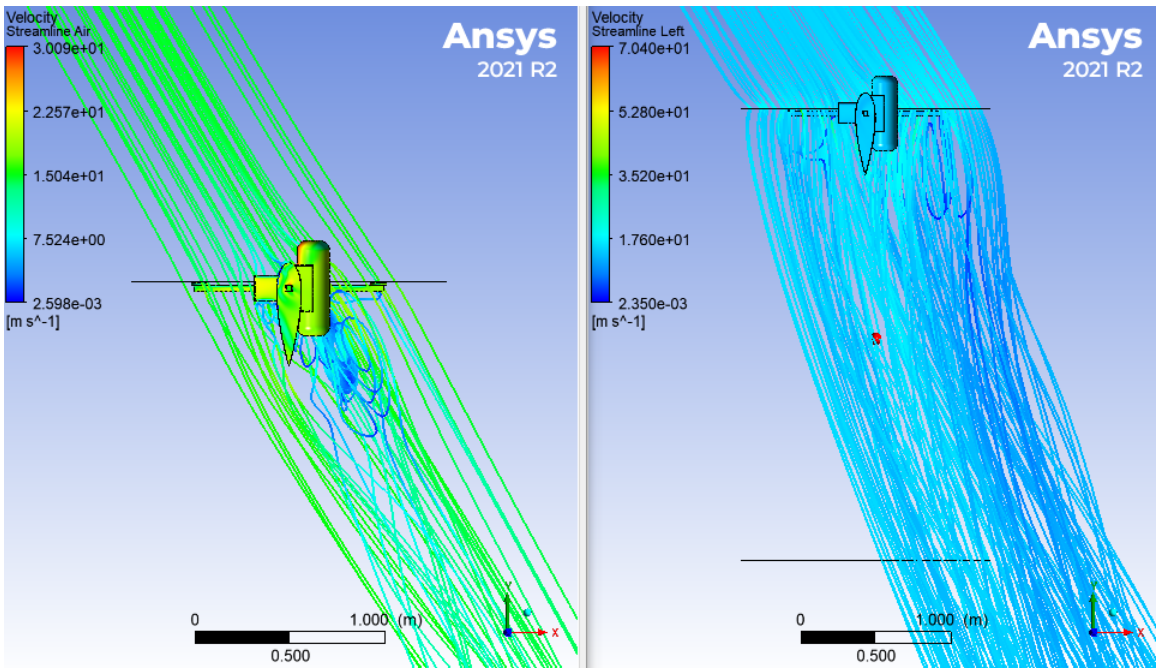

No Actuator Disks (left) and Actuator Disks (right)

Figure 63. Flying Wing in 15 m/s 30° ϵ Streamlines

3. Platform Comparison

Figure 64 compares the lift forces on both platforms from the external flow only models. The lift forces generated by the Flying Wing are all positive and the lift forces generated by the COTS platform are all nearly zero or negative. It is important to highlight that significantly different lift forces are only generates when the airspeed exceeds 4 m/s.

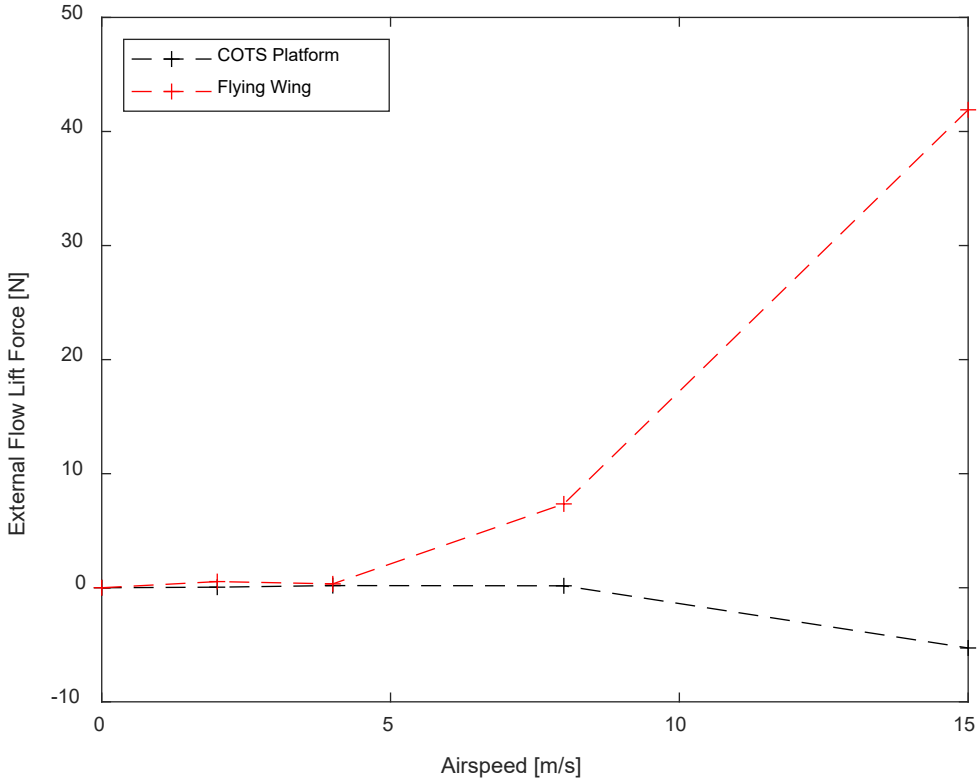

Figure 64. No Actuator Disks Lift

Figure 65 compares the lift forces on both platforms with models that had actuator disks. When the actuator flows are present, the differences between the Flying Wing and the COTS platform are more apparent. The difference is exaggerated due to the ground effect on the arms and motors; however, since both models had the same arm and motor shape, they are comparable. The COTS platform had negative lift in every stage of forward flight models. The Flying Wing had near zero or positive lift in every case modeled. The

positive lift could mean a reduction in induced velocity needed by the craft across all cases of forward flight modeled depending on the platform drag. Once again, the Flying Wing only produced significant lift at the higher airspeeds.

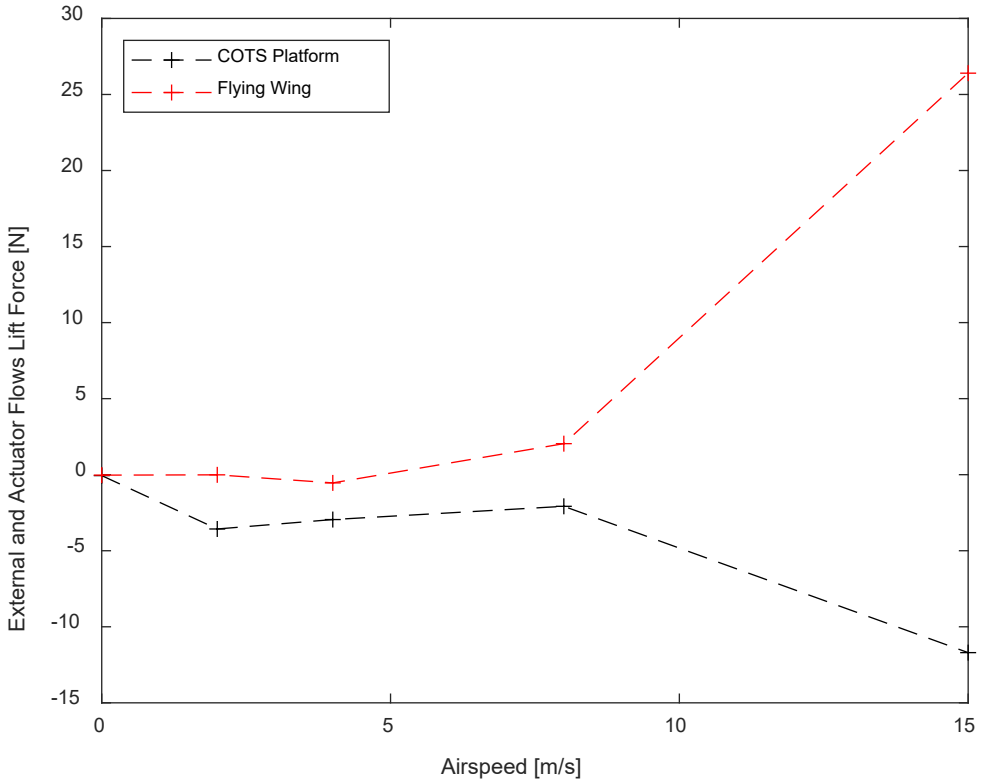

Figure 65. Actuator Disks Lift

Figure 66 compares the drag forces on both platforms from the external flow only models. The smaller surface area of the COTS platform produces a smaller drag force across all cases of forward flight modeled. The Flying Wing has more drag in general and may cause the lift advantages to be negated by the increased platform drag.

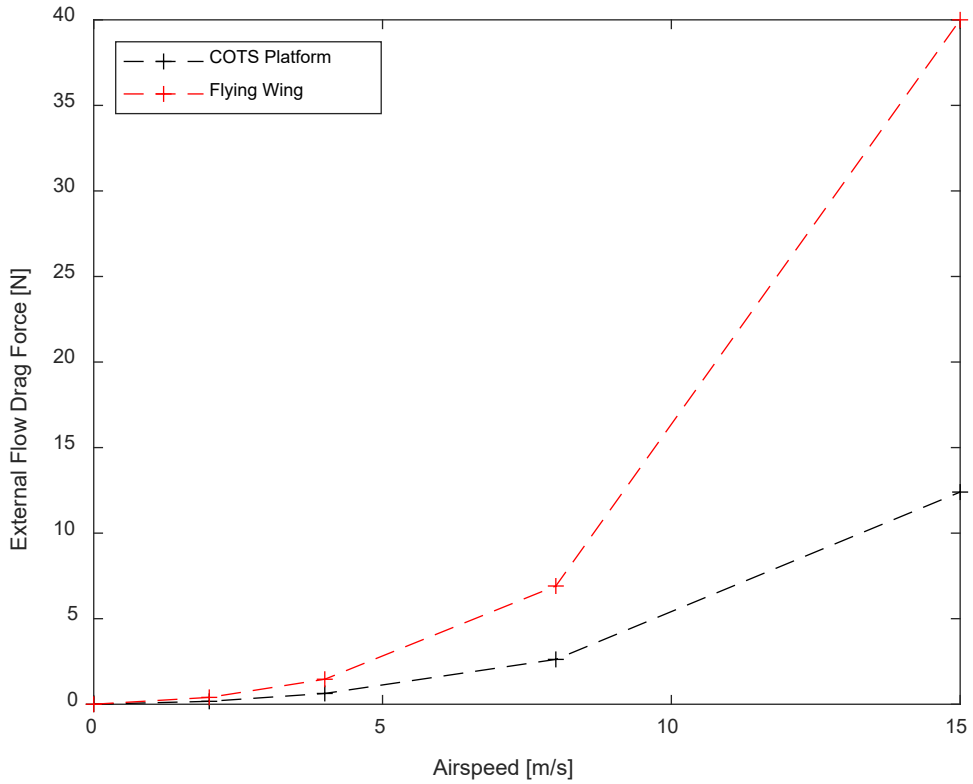

Figure 66. No Actuator Disks Drag

Figure 67 compares the drag forces for both platforms with models with actuator disks. The small surface area of the COTS platform still outperforms the Flying Wing in every case modeled. Both platforms show a reduction in drag from the hover case to the 2 m/s forward flight case. This is most likely due to the simulated ground effect seen across all models with actuator flows. As airspeed increases, the drag increases for both platforms as expected.

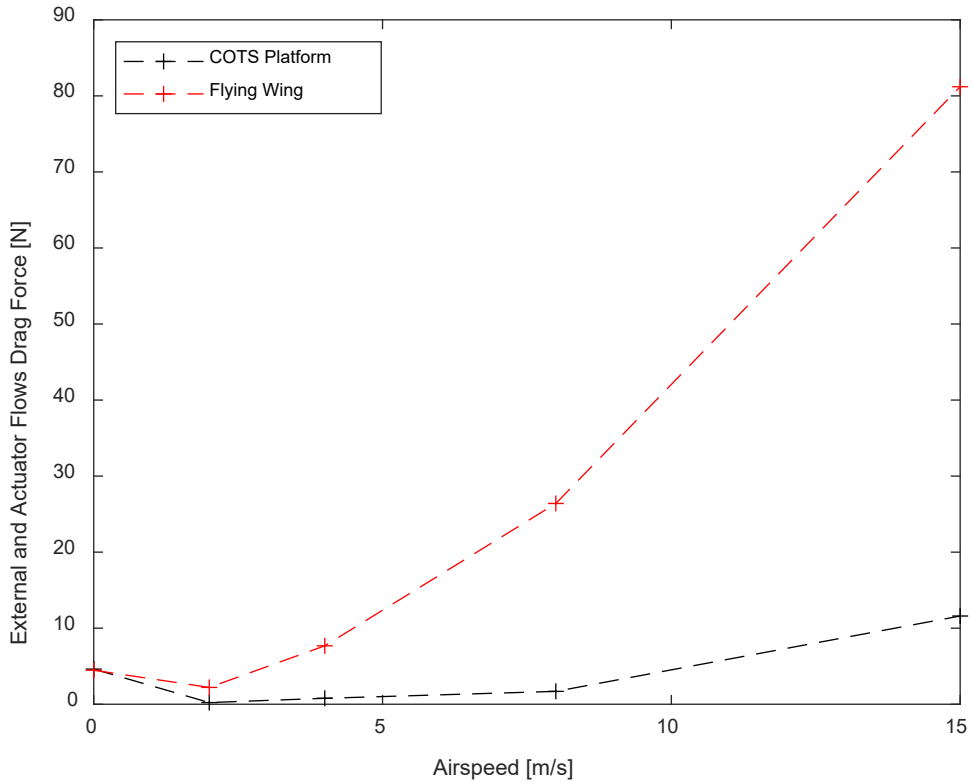

Figure 67. Actuator Disks Drag

Figure 68 shows the average thrust per disk needed by the platforms to maintain level forward flight. The Flying Wing requires significantly less thrust across the lower airspeed than the COTS platform. When the chord AoA reaches the maximum modeled, the amount of thrust needed by both platforms is approximately equal. This is mainly due to the increased drag seen by the Flying Wing at the high chord AoA. For the COTS platform, it is a result of the increased drag and negative lift force. Due to time constraints, a further study of the minimum seen at 4 m/s 8° chord AoA was not conducted to see if the advantages of the Flying Wing could be maintained across multiple airspeeds.

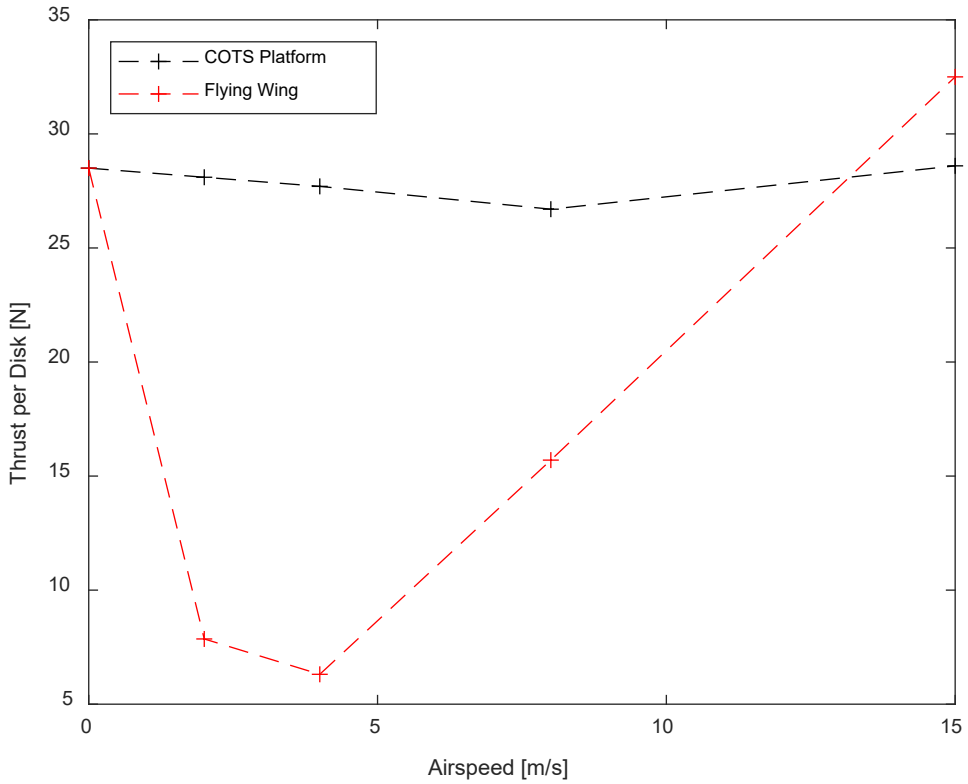

Figure 68. Predicted Disk Thrust

V. CONCLUSION

In conclusion, across the lower chord AoA the Flying Wing models appeared to outperform the COTS platform, albeit, for non-equilibrium conditions. This result supports the hypothesis that designing VTOL craft for forward flight can increase craft endurance. Further modeling and experimentation are needed to further explore this potential advantage. At the maximum chord AoA modeled, the platforms are approximately equal with the smaller surface area of the COTS platform giving it the slight edge over the flying wing.

The models with actuator flows are believed to be biased by the high pressures seen on the arms and motors across all cases of flight modeled. Imposing a velocity boundary condition so close to a surface may not be the best boundary condition. A pressure jump boundary condition may be a better boundary condition to specify at the disks. In addition, the high crossflow seen in the COTS models cause large differences between calculated and produced thrust. All models need some adjustment to better match the expected thrust to ensure full equilibrium is attained. The location of the peak radius was not varied across any of the models. This assumption is most likely incorrect due to the differences between the expected and produced thrusts.

THIS PAGE INTENTIONALLY LEFT BLANK

VI. FUTURE WORK

A further investigation into the vertical and forward flight results of both designs should be conducted to reduce the mismatch between calculated and produced thrust.

Experimental data collection and verification of the predicted COTS platform performance should be conducted. The velocity profile obtained by Richmond's CFD analysis of the propeller should be performed.

For fixed pitch propellers, pitch speed should be included in the model, at least as a limiting case when setting the peak velocity through the actuator disk.

A mesh refinement study of the modeled crafts should be performed. Only a mesh refinement study of the disk in free space was performed in conjunction with this thesis.

Different polynomial distributions for the axial and radial directions of the induced velocity should be investigated to better match the actual velocity profiles. Two additional polynomial profiles were proposed in this thesis for the axial direction based on obtained data. Simulation and experimental data for the radial direction needs to be collected. Varying different boundary conditions for the polynomials should also be investigated as only the peak radius was varied in this thesis.

Different designs like a clean wing, different airfoil, introduction of control surfaces, different propeller configuration, or retracting propellers should also be modeled to see if any further improvements could be made to the Flying Wing.

THIS PAGE INTENTIONALLY LEFT BLANK

APPENDIX A. POLYNOMIAL VELOCITY DISTRIBUTION MATLAB CODE

Copy and paste the code below into a new MATLAB script. To change the polynomial distribution, change value of the lower-case variables. To change the data overlay, input the values desired into vectors V and X. Non-dimensionalize V and X by dividing V and X by their respective maximum values.

```
% 4th Degree Axial Polynomial
clear
clc

syms Ro Rp V0p V0
K = [1,  0,    0,      0,      0,  V0   %Velocity at disk center
    0,  1,    0,      0,      0, V0p   %Acceleration at disk center
    1, Ro, Ro^2,   Ro^3,   Ro^4,   0   %Velocity at disk edge
    0,  1, 2*Rp, 3*Rp^2, 4*Rp^3,   0   %Acceleration at Rp
    1, Rp, Rp^2,   Rp^3,   Rp^4,   1]; %Peak Velocity

Coefs = rref(K);

v0  = 0;
v0p = 0;
rp  = 0.5223;

A1sym = Coefs(1,6);
A1 = double(subs(A1sym,{Ro,Rp,V0,V0p},{1,rp,v0,v0p}));
A2sym = Coefs(2,6);
A2 = double(subs(A2sym,{Ro,Rp,V0,V0p},{1,rp,v0,v0p}));
A3sym = Coefs(3,6);
A3 = double(subs(A3sym,{Ro,Rp,V0,V0p},{1,rp,v0,v0p}));
A4sym = Coefs(4,6);
A4 = double(subs(A4sym,{Ro,Rp,V0,V0p},{1,rp,v0,v0p}));
A5sym = Coefs(5,6);
A5 = double(subs(A5sym,{Ro,Rp,V0,V0p},{1,rp,v0,v0p}));

% Better Fit 4th Degree Axial Polynomial

v0p2 = 2.5;
rp2 = 0.59;

B1 = double(subs(A1sym,{Ro,Rp,V0,V0p},{1,rp2,v0,v0p2}));
B2 = double(subs(A2sym,{Ro,Rp,V0,V0p},{1,rp2,v0,v0p2}));
B3 = double(subs(A3sym,{Ro,Rp,V0,V0p},{1,rp2,v0,v0p2}));
B4 = double(subs(A4sym,{Ro,Rp,V0,V0p},{1,rp2,v0,v0p2}));
B5 = double(subs(A5sym,{Ro,Rp,V0,V0p},{1,rp2,v0,v0p2}));

% 5th Degree Axial Polynomial
```

```
syms Ro Rp Ri V0p V0
K = [1,  0,    0,      0,       0,       0,  V0   %Velocity at disk center
    0,  1,    0,      0,       0,       0, V0p   %Acceleration at disk center
    1, Ro, Ro^2,   Ro^3,    Ro^4,    Ro^5,   0   %Velocity at disk edge
    0,  1, 2*Rp, 3*Rp^2,  4*Rp^3,  5*Rp^4,   0   %Acceleration at Rp
    1, Rp, Rp^2,   Rp^3,    Rp^4,    Rp^5,   1   %Peak Velocity
    0,  0,    2,   6*Ri, 12*Ri^2, 20*Ri^3,   0]; %Inflection Radius

Coefs = rref(K);

v03  = 0;
v0p3 = 0;
rp3  = 0.59;
ri = 0.175;

C1sym = Coefs(1,7);
C1 = double(subs(C1sym,{Ro,Rp,Ri,V0,V0p},{1,rp3,ri,v03,v0p3}));
C2sym = Coefs(2,7);
C2 = double(subs(C2sym,{Ro,Rp,Ri,V0,V0p},{1,rp3,ri,v03,v0p3}));
C3sym = Coefs(3,7);
C3 = double(subs(C3sym,{Ro,Rp,Ri,V0,V0p},{1,rp3,ri,v03,v0p3}));
C4sym = Coefs(4,7);
C4 = double(subs(C4sym,{Ro,Rp,Ri,V0,V0p},{1,rp3,ri,v03,v0p3}));
C5sym = Coefs(5,7);
C5 = double(subs(C5sym,{Ro,Rp,Ri,V0,V0p},{1,rp3,ri,v03,v0p3}));
C6sym = Coefs(6,7);
C6 = double(subs(C6sym,{Ro,Rp,Ri,V0,V0p},{1,rp3,ri,v03,v0p3}));

dr = 1/99;
for n=1:100
   r(n) = dr*(n-1);
   v(n) = -(A1 + A2*r(n) + A3*r(n)^2 + A4*r(n)^3 + A5*r(n)^4);
   vr(n) = v(n)*n*dr;
   b(n) = -(B1 + B2*r(n) + B3*r(n)^2 + B4*r(n)^3 + B5*r(n)^4);
   c(n) = -(C1 + C2*r(n) + C3*r(n)^2 + C4*r(n)^3 + C5*r(n)^4 + C6*r(n)^5);
end
xlabel('r/Ro [m / m]')
ylabel('v/Vp [m/s / m/s]')
V = [0 0.3305 3.0053 5.8715 6.3791 6.7719 6.9083 6.5300 5.7802 4.8422...
    4.0899 1.0697 0]'./-6.9083;
X = [0 0.035 0.07 0.105 0.14 0.175 0.21 0.245 0.28 0.315 0.3325 0.35...
   0.355]'./.355;
figure(1)
plot(r,v,r,b,r,c,X,V,'k+--')
xlabel('r/Ro [m / m]')
ylabel('v/Vp [m/s / m/s]')
legend('Utilized Axial Polynomial','4th Degree Polynomial Fit',...
      '5th Degree Polynomial Fit','CFX Propellor Modeling Data',...
      'Location','north')
hold off
figure(2)
plot(r,vr)
hold on
xlabel('r/Ro [m / m]')
```

```
ylabel('v/Vp [m/s / m/s]')
legend('Radial Polynomial','Location','north')
hold off
```

THIS PAGE INTENTIONALLY LEFT BLANK

APPENDIX B. EXPRESSIONS, EXPERT PARAMETERS, AND MONITOR POINTS

Copy the text below and paste in notepad. Save the notepad file in a location that is easily found. All expressions, expert parameters, and monitor points used in this thesis are defined in the file. Figure 69 shows how to import the saved file into Ansys CFX as a CCL file in setup window:

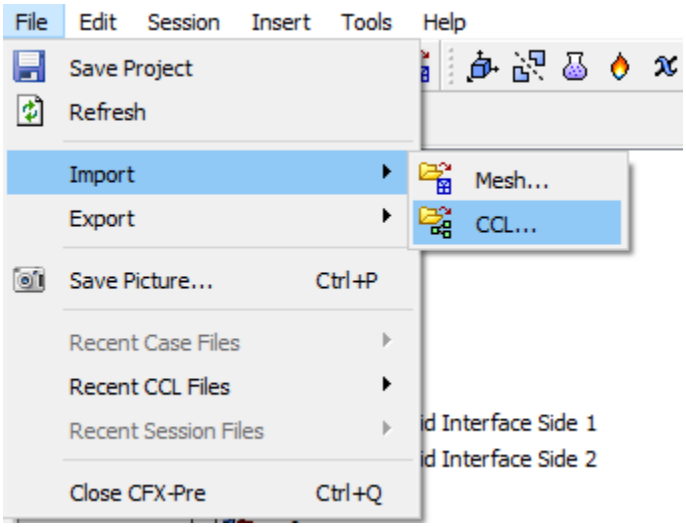

Figure 69. Example Ansys Menu Navigation

```
# State file created:  2022/06/07 09:06:29
# Build 21.2 2021–05-14T23:10:23.832818

LIBRARY:
 CEL:
  EXPRESSIONS:
   AoA = 82 [deg]
   C1 = V0
   C2 = V0p
   C3 = -(4*Ro^3*Rp + 3*Ro^4*V0 + Rp^4*V0 - 3*Ro^4 - 3*Ro^3*Rp^2*V0p - \
    4*Ro^3*Rp*V0 + Ro*Rp^4*V0p + 2*Ro^4*Rp*V0p)/(Ro^2*(Ro^2*Rp^2 - \
    2*Ro*Rp^3 + Rp^4))
   C4 = (2*Ro^4*V0 + 2*Rp^4*V0 - 2*Ro^4 + 4*Ro^2*Rp^2 - 4*Ro^2*Rp^2*V0 - \
    3*Ro^2*Rp^3*V0p + 2*Ro*Rp^4*V0p + Ro^4*Rp*V0p)/(Ro^2*Rp*(Ro^2*Rp^2 -
\
```

```
      2*Ro*Rp^3 + Rp^4))
    C5 = -(3*Ro^2*Rp + 2*Ro^3*V0 + Rp^3*V0 - 2*Ro^3 - 2*Ro^2*Rp^2*V0p - \
      3*Ro^2*Rp*V0 + Ro*Rp^3*V0p + Ro^3*Rp*V0p)/(Ro^2*(Ro^2*Rp^3 - \
      2*Ro*Rp^4 + Rp^5))
    DA = pi*Ro^2
    Drag = -force_y()@Wall*sin(AoA)+force_x()@Wall *cos(AoA)
    ExpT = ((m*g-Lift)*cos(AoA)+Drag*sin(AoA))/3
    Lift = force_y()@Wall*cos(AoA)+force_x()@Wall*sin(AoA)
    QoVp = (C1/2*Ro^2+C2/3*Ro^3+C3/4*Ro^4+C4/5*Ro^5+C5/6*Ro^6)*2*pi
    Rad = sqrt(x^2+z^2)
    RadC = sqrt(x^2+(z+1.6[m])^2)
    RadL = sqrt((x+0.47[m])^2+(z+1.0625[m])^2)
    RadR = sqrt((x-0.47[m])^2+(z+1.0625[m])^2)
    Ro = 0.355 [m]
    Rp = 0.5223*Ro
    Thrust = force_y()@Left Disk+force_y()@Right Disk+force_y()@Center Disk
    V0 = 0
    V0p = 0 [m^-1]
    Vh = sqrt(ExpT/(2*rho*DA))
    Vi = (C1+C2*Rad+C3*Rad^2+C4*Rad^3+C5*Rad^4)*Vp
    ViC = (C1+C2*RadC+C3*RadC^2+C4*RadC^3+C5*RadC^4)*Vp
    ViL = (C1+C2*RadL+C3*RadL^2+C4*RadL^3+C5*RadL^4)*Vp
    ViR = (C1+C2*RadR+C3*RadR^2+C4*RadR^3+C5*RadR^4)*Vp
    Vin = 4 [m/s]
    Vo = -Vperp/2+sqrt(Vperp^2/4+Vh^2)
    Vp = Vu*DA/QoVp
    Vpara = Vin*cos(AoA)
    Vperp = Vin*sin(AoA)
    Vu = Vh^2/sqrt(Vpara^2+(Vperp+Vo)^2)
    m = 8.25 [kg]
    rho = areaAve(Density)@Top
  END
 END
END
FLOW: Flow Analysis 1
 OUTPUT CONTROL:
  MONITOR OBJECTS:
    MONITOR BALANCES:
      Option = Full
    END
    MONITOR FORCES:
      Option = Full
    END
    MONITOR PARTICLES:
      Option = Full
```

```
    END
    MONITOR POINT: Monitor Point Drag
      Coord Frame = Coord 0
      Expression Value = Drag
      Option = Expression
    END
    MONITOR POINT: Monitor Point Lift
      Coord Frame = Coord 0
      Expression Value = Lift
      Option = Expression
    END
    MONITOR POINT: Monitor Point Thrust
      Coord Frame = Coord 0
      Expression Value = Thrust
      Option = Expression
    END
    MONITOR RESIDUALS:
      Option = Full
    END
    MONITOR TOTALS:
      Option = Full
    END
  END
  RESULTS:
    File Compression Level = Default
    Option = Standard
  END
END
SOLVER CONTROL:
  Turbulence Numerics = First Order
  ADVECTION SCHEME:
    Option = High Resolution
  END
  CONVERGENCE CONTROL:
    Length Scale Option = Conservative
    Maximum Number of Iterations = 100
    Minimum Number of Iterations = 1
    Timescale Control = Auto Timescale
    Timescale Factor = 1.0
  END
  CONVERGENCE CRITERIA:
    Residual Target = 0.000000000000001
    Residual Type = RMS
  END
  DYNAMIC MODEL CONTROL:
```

```
    Global Dynamic Model Control = On
   END
   INTERRUPT CONTROL:
    Option = Any Interrupt
    CONVERGENCE CONDITIONS:
     Option = Default Conditions
    END
   END
  END
  EXPERT PARAMETERS:
   topology estimate factor = 1.2
   topology estimate factor zif = 1.2
  END
 END
 COMMAND FILE:
  Version = 21.2
 END
```

APPENDIX C. DISK IN FREE SPACE ANSYS REPORT

Below are the ANSYS CFX workbook settings and details for a disk in free space:

Date
2022/05/10 12:16:59

VIII. Contents

IX. 1. File Report

Table 1. File Information for CFX

Case	CFX
File Path	C:\Users\zachary.ceroli\Documents\Ceroli\Ansys\Act Disk Hover_files\dp0\CFX\CFX\Fluid Flow CFX_010.res
File Date	07 April 2022
File Time	12:54:28 PM
File Type	CFX5
File Version	21.2

X. 2. Mesh Report

Table 2. Mesh Information for CFX

Domain	Nodes	Elements
Default Domain	4518639	10808121

XI. 3. Physics Report

Table 3. Domain Physics for CFX

Domain - Default Domain

Type	Fluid
Location	Act, Fluid Volume
Materials	
Air at 25 C	
Fluid Definition	Material Library
Morphology	Continuous Fluid
Settings	

Buoyancy Model Non Buoyant
Domain Motion Stationary
Reference Pressure 1.0000e+0 [atm]
Heat Transfer Model Isothermal
Fluid Temperature 2.5000e+1 [C]
Turbulence Model SST
Turbulent Wall Functions Automatic
Domain Interface - Default Fluid Fluid Interface
Boundary List1 Default Fluid Fluid Interface Side 1
Boundary List2 Default Fluid Fluid Interface Side 2
Interface Type Fluid Fluid
Settings
Interface Models General Connection
Mass And Momentum Conservative Interface Flux
Mesh Connection Automatic

Table 4. Boundary Physics for CFX
Domain Boundaries
Default Domain Boundary - Default Fluid Fluid Interface Side 1
Type INTERFACE
Location Act Bottom, Act Cyl
Settings
Mass And Momentum Conservative Interface Flux
Turbulence Conservative Interface Flux
Boundary - Default Fluid Fluid Interface Side 2
Type INTERFACE
Location Cyl, Cyl Bottom
Settings
Mass And Momentum Conservative Interface Flux
Turbulence Conservative Interface Flux
Boundary - Disk
Type OPENING
Location Act Disk, Disk
Settings
Flow Regime Subsonic
Mass And Momentum Cylindrical Velocity Components
Velocity Axial Component -Vi
Velocity Theta Component 0.0000e+0 [m s^-1]
Velocity r Component -Vi*Rad/Ro
Axis Definition Coordinate Axis
Rotation Axis Coord 0.2
Turbulence Medium Intensity and Eddy Viscosity Ratio
Boundary - Left
Type OPENING

Location Left
Settings
Flow Regime Subsonic
Mass And Momentum Entrainment
Relative Pressure 0.0000e+0 [Pa]
Turbulence Zero Gradient
Boundary - Openings
Type OPENING
Location Back, Bottom, Front, Right
Settings
Flow Regime Subsonic
Mass And Momentum Entrainment
Relative Pressure 0.0000e+0 [Pa]
Turbulence Zero Gradient
Boundary - Top
Type OPENING
Location Top
Settings
Flow Regime Subsonic
Mass And Momentum Entrainment
Relative Pressure 0.0000e+0 [Pa]
Turbulence Zero Gradient

XII. 4. User Data

THIS PAGE INTENTIONALLY LEFT BLANK

APPENDIX D. RESULTS OF PEAK RADIUS VARIATION OF VELOCITY POLYNOMIALS

Below is the MATLAB code used to display the CFD results from varying peak radius location of the polynomial velocity distributions.

```
%% Resulting Thrust Graph
clear
clc
format short
%Peak Radius Location
Rp = [0.5, 0.51, 0.52, 0.53, 0.54, 0.55,...
          0.56, 0.57, 0.58, 0.59, 0.6,...
          0.61, 0.62, 0.63, 0.64, 0.65,...
          0.66, 0.67, 0.68, 0.69, 0.7,...
          0.71, 0.72, 0.73, 0.74, 0.75]';
T_Rp = [28.6103, 27.7459, 27.0945, 26.5934, 26.2015, 25.8929,...
                25.6477, 25.4527, 25.2965, 25.1720, 25.0729,...
                24.9949, 24.9355, 24.8934, 24.8673, 24.8561,...
                24.8593, 24.8778, 24.9122, 24.9646, 25.0379,...
                25.1375, 25.2697, 25.4425, 25.6678, 25.9652]';
Rp_v_T = fit(Rp, T_Rp, 'poly6');
Rp_I =@(x) Rp_v_T(x)-2.75*9.80665;
Ideal_Rp = fzero(Rp_I,0.51)
x = [0.5:0.001:0.75]';
Curve_Rp = Rp_v_T(x);
figure(3)
plot(Rp,T_Rp,'k+',x,Curve_Rp)
yline(2.75*9.80665)
legend('CFX Data','Curve Fit','Desired Thrust')
xlabel('Non-Dimensional Peak Radius Position (Rp/Ro)')
ylabel('CFX Thrust Output (N)')
annotation(figure(3),'textbox',...
   [0.324214285714286 0.726190476190476 0.181142857142857
0.0571428571428605],...
   'String',{'Desired Thrust'},...
   'FitBoxToText','off');
annotation(figure(3),'arrow',[0.323214285714286 0.208928571428571],...
   [0.726190476190476 0.571428571428572]);
```

THIS PAGE INTENTIONALLY LEFT BLANK

APPENDIX E. AXIAL VELOCITY MATLAB CODE

Below is the exported axial velocity distribution at the disk from the single disk in free space CFD simulations. Overlayed on top is the exported data is the CFD values for axial velocity provided by Alex Richmond [19].

```
Z = [0.00E+00 4.00E-04 8.01E-04 1.20E-03 1.60E-03 2.00E-03 2.40E-03 2.80E-03…
3.20E-03 3.60E-03 4.00E-03 4.40E-03 4.80E-03 5.21E-03 5.61E-03 6.01E-03…
6.41E-03 6.81E-03 7.21E-03 7.61E-03 8.01E-03 8.41E-03 8.81E-03 9.21E-03…
9.61E-03 1.00E-02 1.04E-02 1.08E-02 1.12E-02 1.16E-02 1.20E-02 1.24E-02…
1.28E-02 1.32E-02 1.36E-02 1.40E-02 1.44E-02 1.48E-02 1.52E-02 1.56E-02…
1.60E-02 1.64E-02 1.68E-02 1.72E-02 1.76E-02 1.80E-02 1.84E-02 1.88E-02…
1.92E-02 1.96E-02 2.00E-02 2.04E-02 2.08E-02 2.12E-02 2.16E-02 2.20E-02…
2.24E-02 2.28E-02 2.32E-02 2.36E-02 2.40E-02 2.44E-02 2.48E-02 2.52E-02…
2.56E-02 2.60E-02 2.64E-02 2.68E-02 2.72E-02 2.76E-02 2.80E-02 2.84E-02…
2.88E-02 2.92E-02 2.96E-02 3.00E-02 3.04E-02 3.08E-02 3.12E-02 3.16E-02…
3.20E-02 3.24E-02 3.28E-02 3.32E-02 3.36E-02 3.40E-02 3.44E-02 3.48E-02…
3.52E-02 3.56E-02 3.60E-02 3.64E-02 3.68E-02 3.72E-02 3.76E-02 3.80E-02…
3.84E-02 3.88E-02 3.92E-02 3.96E-02 4.00E-02 4.04E-02 4.08E-02 4.12E-02…
4.16E-02 4.20E-02 4.24E-02 4.28E-02 4.32E-02 4.36E-02 4.40E-02 4.44E-02…
4.48E-02 4.52E-02 4.56E-02 4.60E-02 4.64E-02 4.68E-02 4.72E-02 4.76E-02…
4.80E-02 4.84E-02 4.88E-02 4.92E-02 4.96E-02 5.01E-02 5.05E-02 5.09E-02…
5.13E-02 5.17E-02 5.21E-02 5.25E-02 5.29E-02 5.33E-02 5.37E-02 5.41E-02…
5.45E-02 5.49E-02 5.53E-02 5.57E-02 5.61E-02 5.65E-02 5.69E-02 5.73E-02…
5.77E-02 5.81E-02 5.85E-02 5.89E-02 5.93E-02 5.97E-02 6.01E-02 6.05E-02…
6.09E-02 6.13E-02 6.17E-02 6.21E-02 6.25E-02 6.29E-02 6.33E-02 6.37E-02…
6.41E-02 6.45E-02 6.49E-02 6.53E-02 6.57E-02 6.61E-02 6.65E-02 6.69E-02…
6.73E-02 6.77E-02 6.81E-02 6.85E-02 6.89E-02 6.93E-02 6.97E-02 7.01E-02…
7.05E-02 7.09E-02 7.13E-02 7.17E-02 7.21E-02 7.25E-02 7.29E-02 7.33E-02…
7.37E-02 7.41E-02 7.45E-02 7.49E-02 7.53E-02 7.57E-02 7.61E-02 7.65E-02…
7.69E-02 7.73E-02 7.77E-02 7.81E-02 7.85E-02 7.89E-02 7.93E-02 7.97E-02…
8.01E-02 8.05E-02 8.09E-02 8.13E-02 8.17E-02 8.21E-02 8.25E-02 8.29E-02…
8.33E-02 8.37E-02 8.41E-02 8.45E-02 8.49E-02 8.53E-02 8.57E-02 8.61E-02…
8.65E-02 8.69E-02 8.73E-02 8.77E-02 8.81E-02 8.85E-02 8.89E-02 8.93E-02…
8.97E-02 9.01E-02 9.05E-02 9.09E-02 9.13E-02 9.17E-02 9.21E-02 9.25E-02…
9.29E-02 9.33E-02 9.37E-02 9.41E-02 9.45E-02 9.49E-02 9.53E-02 9.57E-02…
9.61E-02 9.65E-02 9.69E-02 9.73E-02 9.77E-02 9.81E-02 9.85E-02 9.89E-02…
9.93E-02 9.97E-02 1.00E-01 1.01E-01 1.01E-01 1.01E-01 1.02E-01 1.02E-01…
1.03E-01 1.03E-01 1.03E-01 1.04E-01 1.04E-01 1.05E-01 1.05E-01 1.05E-01…
1.06E-01 1.06E-01 1.07E-01 1.07E-01 1.07E-01 1.08E-01 1.08E-01 1.09E-01…
1.09E-01 1.09E-01 1.10E-01 1.10E-01 1.11E-01 1.11E-01 1.11E-01 1.12E-01…
1.12E-01 1.13E-01 1.13E-01 1.13E-01 1.14E-01 1.14E-01 1.15E-01 1.15E-01…
1.15E-01 1.16E-01 1.16E-01 1.17E-01 1.17E-01 1.17E-01 1.18E-01 1.18E-01…
1.19E-01 1.19E-01 1.19E-01 1.20E-01 1.20E-01 1.21E-01 1.21E-01 1.21E-01…
1.22E-01 1.22E-01 1.23E-01 1.23E-01 1.23E-01 1.24E-01 1.24E-01 1.25E-01…
1.25E-01 1.25E-01 1.26E-01 1.26E-01 1.27E-01 1.27E-01 1.27E-01 1.28E-01…
1.28E-01 1.29E-01 1.29E-01 1.29E-01 1.30E-01 1.30E-01 1.31E-01 1.31E-01…
1.31E-01 1.32E-01 1.32E-01 1.33E-01 1.33E-01 1.33E-01 1.34E-01 1.34E-01…
1.35E-01 1.35E-01 1.35E-01 1.36E-01 1.36E-01 1.37E-01 1.37E-01 1.37E-01…
```

1.38E-01 1.38E-01 1.39E-01 1.39E-01 1.39E-01 1.40E-01 1.40E-01 1.41E-01…
1.41E-01 1.41E-01 1.42E-01 1.42E-01 1.43E-01 1.43E-01 1.43E-01 1.44E-01…
1.44E-01 1.45E-01 1.45E-01 1.45E-01 1.46E-01 1.46E-01 1.47E-01 1.47E-01…
1.47E-01 1.48E-01 1.48E-01 1.49E-01 1.49E-01 1.49E-01 1.50E-01 1.50E-01…
1.51E-01 1.51E-01 1.51E-01 1.52E-01 1.52E-01 1.53E-01 1.53E-01 1.53E-01…
1.54E-01 1.54E-01 1.55E-01 1.55E-01 1.55E-01 1.56E-01 1.56E-01 1.57E-01…
1.57E-01 1.57E-01 1.58E-01 1.58E-01 1.59E-01 1.59E-01 1.59E-01 1.60E-01…
1.60E-01 1.61E-01 1.61E-01 1.61E-01 1.62E-01 1.62E-01 1.63E-01 1.63E-01…
1.63E-01 1.64E-01 1.64E-01 1.65E-01 1.65E-01 1.65E-01 1.66E-01 1.66E-01…
1.67E-01 1.67E-01 1.67E-01 1.68E-01 1.68E-01 1.69E-01 1.69E-01 1.69E-01…
1.70E-01 1.70E-01 1.71E-01 1.71E-01 1.71E-01 1.72E-01 1.72E-01 1.73E-01…
1.73E-01 1.73E-01 1.74E-01 1.74E-01 1.75E-01 1.75E-01 1.75E-01 1.76E-01…
1.76E-01 1.77E-01 1.77E-01 1.77E-01 1.78E-01 1.78E-01 1.79E-01 1.79E-01…
1.79E-01 1.80E-01 1.80E-01 1.81E-01 1.81E-01 1.81E-01 1.82E-01 1.82E-01…
1.83E-01 1.83E-01 1.83E-01 1.84E-01 1.84E-01 1.85E-01 1.85E-01 1.85E-01…
1.86E-01 1.86E-01 1.87E-01 1.87E-01 1.87E-01 1.88E-01 1.88E-01 1.89E-01…
1.89E-01 1.89E-01 1.90E-01 1.90E-01 1.91E-01 1.91E-01 1.91E-01 1.92E-01…
1.92E-01 1.93E-01 1.93E-01 1.93E-01 1.94E-01 1.94E-01 1.95E-01 1.95E-01…
1.95E-01 1.96E-01 1.96E-01 1.97E-01 1.97E-01 1.97E-01 1.98E-01 1.98E-01…
1.99E-01 1.99E-01 1.99E-01 2.00E-01 2.00E-01 2.01E-01 2.01E-01 2.01E-01…
2.02E-01 2.02E-01 2.03E-01 2.03E-01 2.03E-01 2.04E-01 2.04E-01 2.05E-01…
2.05E-01 2.05E-01 2.06E-01 2.06E-01 2.07E-01 2.07E-01 2.07E-01 2.08E-01…
2.08E-01 2.09E-01 2.09E-01 2.09E-01 2.10E-01 2.10E-01 2.11E-01 2.11E-01…
2.11E-01 2.12E-01 2.12E-01 2.13E-01 2.13E-01 2.13E-01 2.14E-01 2.14E-01…
2.15E-01 2.15E-01 2.15E-01 2.16E-01 2.16E-01 2.17E-01 2.17E-01 2.17E-01…
2.18E-01 2.18E-01 2.19E-01 2.19E-01 2.19E-01 2.20E-01 2.20E-01 2.21E-01…
2.21E-01 2.21E-01 2.22E-01 2.22E-01 2.23E-01 2.23E-01 2.23E-01 2.24E-01…
2.24E-01 2.25E-01 2.25E-01 2.25E-01 2.26E-01 2.26E-01 2.27E-01 2.27E-01…
2.27E-01 2.28E-01 2.28E-01 2.29E-01 2.29E-01 2.29E-01 2.30E-01 2.30E-01…
2.31E-01 2.31E-01 2.31E-01 2.32E-01 2.32E-01 2.33E-01 2.33E-01 2.33E-01…
2.34E-01 2.34E-01 2.35E-01 2.35E-01 2.35E-01 2.36E-01 2.36E-01 2.37E-01…
2.37E-01 2.37E-01 2.38E-01 2.38E-01 2.39E-01 2.39E-01 2.39E-01 2.40E-01…
2.40E-01 2.41E-01 2.41E-01 2.41E-01 2.42E-01 2.42E-01 2.43E-01 2.43E-01…
2.43E-01 2.44E-01 2.44E-01 2.45E-01 2.45E-01 2.45E-01 2.46E-01 2.46E-01…
2.47E-01 2.47E-01 2.47E-01 2.48E-01 2.48E-01 2.49E-01 2.49E-01 2.49E-01…
2.50E-01 2.50E-01 2.51E-01 2.51E-01 2.51E-01 2.52E-01 2.52E-01 2.53E-01…
2.53E-01 2.53E-01 2.54E-01 2.54E-01 2.55E-01 2.55E-01 2.55E-01 2.56E-01…
2.56E-01 2.57E-01 2.57E-01 2.57E-01 2.58E-01 2.58E-01 2.59E-01 2.59E-01…
2.59E-01 2.60E-01 2.60E-01 2.61E-01 2.61E-01 2.61E-01 2.62E-01 2.62E-01…
2.63E-01 2.63E-01 2.63E-01 2.64E-01 2.64E-01 2.65E-01 2.65E-01 2.65E-01…
2.66E-01 2.66E-01 2.67E-01 2.67E-01 2.67E-01 2.68E-01 2.68E-01 2.69E-01…
2.69E-01 2.69E-01 2.70E-01 2.70E-01 2.71E-01 2.71E-01 2.71E-01 2.72E-01…
2.72E-01 2.73E-01 2.73E-01 2.73E-01 2.74E-01 2.74E-01 2.75E-01 2.75E-01…
2.75E-01 2.76E-01 2.76E-01 2.77E-01 2.77E-01 2.77E-01 2.78E-01 2.78E-01…
2.79E-01 2.79E-01 2.79E-01 2.80E-01 2.80E-01 2.81E-01 2.81E-01 2.81E-01…
2.82E-01 2.82E-01 2.83E-01 2.83E-01 2.83E-01 2.84E-01 2.84E-01 2.85E-01…
2.85E-01 2.85E-01 2.86E-01 2.86E-01 2.87E-01 2.87E-01 2.87E-01 2.88E-01…
2.88E-01 2.89E-01 2.89E-01 2.89E-01 2.90E-01 2.90E-01 2.91E-01 2.91E-01…
2.91E-01 2.92E-01 2.92E-01 2.93E-01 2.93E-01 2.93E-01 2.94E-01 2.94E-01…
2.95E-01 2.95E-01 2.95E-01 2.96E-01 2.96E-01 2.97E-01 2.97E-01 2.97E-01…
2.98E-01 2.98E-01 2.99E-01 2.99E-01 2.99E-01 3.00E-01 3.00E-01 3.01E-01…
3.01E-01 3.01E-01 3.02E-01 3.02E-01 3.03E-01 3.03E-01 3.04E-01 3.04E-01…
3.04E-01 3.05E-01 3.05E-01 3.06E-01 3.06E-01 3.06E-01 3.07E-01 3.07E-01…
3.08E-01 3.08E-01 3.08E-01 3.09E-01 3.09E-01 3.10E-01 3.10E-01 3.10E-01…

```
3.11E-01 3.11E-01 3.12E-01 3.12E-01 3.12E-01 3.13E-01 3.13E-01 3.14E-01…
3.14E-01 3.14E-01 3.15E-01 3.15E-01 3.16E-01 3.16E-01 3.16E-01 3.17E-01…
3.17E-01 3.18E-01 3.18E-01 3.18E-01 3.19E-01 3.19E-01 3.20E-01 3.20E-01…
3.20E-01 3.21E-01 3.21E-01 3.22E-01 3.22E-01 3.22E-01 3.23E-01 3.23E-01…
3.24E-01 3.24E-01 3.24E-01 3.25E-01 3.25E-01 3.26E-01 3.26E-01 3.26E-01…
3.27E-01 3.27E-01 3.28E-01 3.28E-01 3.28E-01 3.29E-01 3.29E-01 3.30E-01…
3.30E-01 3.30E-01 3.31E-01 3.31E-01 3.32E-01 3.32E-01 3.32E-01 3.33E-01…
3.33E-01 3.34E-01 3.34E-01 3.34E-01 3.35E-01 3.35E-01 3.36E-01 3.36E-01…
3.36E-01 3.37E-01 3.37E-01 3.38E-01 3.38E-01 3.38E-01 3.39E-01 3.39E-01…
3.40E-01 3.40E-01 3.40E-01 3.41E-01 3.41E-01 3.42E-01 3.42E-01 3.42E-01…
3.43E-01 3.43E-01 3.44E-01 3.44E-01 3.44E-01 3.45E-01 3.45E-01 3.46E-01…
3.46E-01 3.46E-01 3.47E-01 3.47E-01 3.48E-01 3.48E-01 3.48E-01 3.49E-01…
3.49E-01 3.50E-01 3.50E-01 3.50E-01 3.51E-01 3.51E-01 3.52E-01 3.52E-01…
3.52E-01 3.53E-01 3.53E-01 3.54E-01 3.54E-01 3.54E-01 3.55E-01 3.55E-01…
3.56E-01 3.56E-01 3.56E-01 3.57E-01 3.57E-01 3.58E-01 3.58E-01 3.58E-01…
3.59E-01 3.59E-01 3.60E-01 3.60E-01 3.60E-01 3.61E-01 3.61E-01 3.62E-01…
3.62E-01 3.62E-01 3.63E-01 3.63E-01 3.64E-01 3.64E-01 3.64E-01 3.65E-01…
3.65E-01 3.66E-01 3.66E-01 3.66E-01 3.67E-01 3.67E-01 3.68E-01 3.68E-01…
3.68E-01 3.69E-01 3.69E-01 3.70E-01 3.70E-01 3.70E-01 3.71E-01 3.71E-01…
3.72E-01 3.72E-01 3.72E-01 3.73E-01 3.73E-01 3.74E-01 3.74E-01 3.74E-01…
3.75E-01 3.75E-01 3.76E-01 3.76E-01 3.76E-01 3.77E-01 3.77E-01 3.78E-01…
3.78E-01 3.78E-01 3.79E-01 3.79E-01 3.80E-01 3.80E-01 3.80E-01 3.81E-01…
3.81E-01 3.82E-01 3.82E-01 3.82E-01 3.83E-01 3.83E-01 3.84E-01 3.84E-01…
3.84E-01 3.85E-01 3.85E-01 3.86E-01 3.86E-01 3.86E-01 3.87E-01 3.87E-01…
3.88E-01 3.88E-01 3.88E-01 3.89E-01 3.89E-01 3.90E-01 3.90E-01 3.90E-01…
3.91E-01 3.91E-01 3.92E-01 3.92E-01 3.92E-01 3.93E-01 3.93E-01 3.94E-01…
3.94E-01 3.94E-01 3.95E-01 3.95E-01 3.96E-01 3.96E-01 3.96E-01 3.97E-01…
3.97E-01 3.98E-01 3.98E-01 3.98E-01 3.99E-01 3.99E-01 4.00E-01 4.00E-01];
V_uni =[0.00E+00…
4.00E-04 8.01E-04 1.20E-03 1.60E-03 2.00E-03 2.40E-03 2.80E-03…
3.20E-03 3.60E-03 4.00E-03 4.40E-03 4.80E-03 5.21E-03 5.61E-03 6.01E-03…
6.41E-03 6.81E-03 7.21E-03 7.61E-03 8.01E-03 8.41E-03 8.81E-03 9.21E-03…
9.61E-03 1.00E-02 1.04E-02 1.08E-02 1.12E-02 1.16E-02 1.20E-02 1.24E-02…
1.28E-02 1.32E-02 1.36E-02 1.40E-02 1.44E-02 1.48E-02 1.52E-02 1.56E-02…
1.60E-02 1.64E-02 1.68E-02 1.72E-02 1.76E-02 1.80E-02 1.84E-02 1.88E-02…
1.92E-02 1.96E-02 2.00E-02 2.04E-02 2.08E-02 2.12E-02 2.16E-02 2.20E-02…
2.24E-02 2.28E-02 2.32E-02 2.36E-02 2.40E-02 2.44E-02 2.48E-02 2.52E-02…
2.56E-02 2.60E-02 2.64E-02 2.68E-02 2.72E-02 2.76E-02 2.80E-02 2.84E-02…
2.88E-02 2.92E-02 2.96E-02 3.00E-02 3.04E-02 3.08E-02 3.12E-02 3.16E-02…
3.20E-02 3.24E-02 3.28E-02 3.32E-02 3.36E-02 3.40E-02 3.44E-02 3.48E-02…
3.52E-02 3.56E-02 3.60E-02 3.64E-02 3.68E-02 3.72E-02 3.76E-02 3.80E-02…
3.84E-02 3.88E-02 3.92E-02 3.96E-02 4.00E-02 4.04E-02 4.08E-02 4.12E-02…
4.16E-02 4.20E-02 4.24E-02 4.28E-02 4.32E-02 4.36E-02 4.40E-02 4.44E-02…
4.48E-02 4.52E-02 4.56E-02 4.60E-02 4.64E-02 4.68E-02 4.72E-02 4.76E-02…
4.80E-02 4.84E-02 4.88E-02 4.92E-02 4.96E-02 5.01E-02 5.05E-02 5.09E-02…
5.13E-02 5.17E-02 5.21E-02 5.25E-02 5.29E-02 5.33E-02 5.37E-02 5.41E-02…
5.45E-02 5.49E-02 5.53E-02 5.57E-02 5.61E-02 5.65E-02 5.69E-02 5.73E-02…
5.77E-02 5.81E-02 5.85E-02 5.89E-02 5.93E-02 5.97E-02 6.01E-02 6.05E-02…
6.09E-02 6.13E-02 6.17E-02 6.21E-02 6.25E-02 6.29E-02 6.33E-02 6.37E-02…
6.41E-02 6.45E-02 6.49E-02 6.53E-02 6.57E-02 6.61E-02 6.65E-02 6.69E-02…
6.73E-02 6.77E-02 6.81E-02 6.85E-02 6.89E-02 6.93E-02 6.97E-02 7.01E-02…
7.05E-02 7.09E-02 7.13E-02 7.17E-02 7.21E-02 7.25E-02 7.29E-02 7.33E-02…
7.37E-02 7.41E-02 7.45E-02 7.49E-02 7.53E-02 7.57E-02 7.61E-02 7.65E-02…
7.69E-02 7.73E-02 7.77E-02 7.81E-02 7.85E-02 7.89E-02 7.93E-02 7.97E-02…
```

8.01E-02 8.05E-02 8.09E-02 8.13E-02 8.17E-02 8.21E-02 8.25E-02 8.29E-02…
8.33E-02 8.37E-02 8.41E-02 8.45E-02 8.49E-02 8.53E-02 8.57E-02 8.61E-02…
8.65E-02 8.69E-02 8.73E-02 8.77E-02 8.81E-02 8.85E-02 8.89E-02 8.93E-02…
8.97E-02 9.01E-02 9.05E-02 9.09E-02 9.13E-02 9.17E-02 9.21E-02 9.25E-02…
9.29E-02 9.33E-02 9.37E-02 9.41E-02 9.45E-02 9.49E-02 9.53E-02 9.57E-02…
9.61E-02 9.65E-02 9.69E-02 9.73E-02 9.77E-02 9.81E-02 9.85E-02 9.89E-02…
9.93E-02 9.97E-02 1.00E-01 1.01E-01 1.01E-01 1.01E-01 1.02E-01 1.02E-01…
1.03E-01 1.03E-01 1.03E-01 1.04E-01 1.04E-01 1.05E-01 1.05E-01 1.05E-01…
1.06E-01 1.06E-01 1.07E-01 1.07E-01 1.07E-01 1.08E-01 1.08E-01 1.09E-01…
1.09E-01 1.09E-01 1.10E-01 1.10E-01 1.11E-01 1.11E-01 1.11E-01 1.12E-01…
1.12E-01 1.13E-01 1.13E-01 1.13E-01 1.14E-01 1.14E-01 1.15E-01 1.15E-01…
1.15E-01 1.16E-01 1.16E-01 1.17E-01 1.17E-01 1.17E-01 1.18E-01 1.18E-01…
1.19E-01 1.19E-01 1.19E-01 1.20E-01 1.20E-01 1.21E-01 1.21E-01 1.21E-01…
1.22E-01 1.22E-01 1.23E-01 1.23E-01 1.23E-01 1.24E-01 1.24E-01 1.25E-01…
1.25E-01 1.25E-01 1.26E-01 1.26E-01 1.27E-01 1.27E-01 1.27E-01 1.28E-01…
1.28E-01 1.29E-01 1.29E-01 1.29E-01 1.30E-01 1.30E-01 1.31E-01 1.31E-01…
1.31E-01 1.32E-01 1.32E-01 1.33E-01 1.33E-01 1.33E-01 1.34E-01 1.34E-01…
1.35E-01 1.35E-01 1.35E-01 1.36E-01 1.36E-01 1.37E-01 1.37E-01 1.37E-01…
1.38E-01 1.38E-01 1.39E-01 1.39E-01 1.39E-01 1.40E-01 1.40E-01 1.41E-01…
1.41E-01 1.41E-01 1.42E-01 1.42E-01 1.43E-01 1.43E-01 1.43E-01 1.44E-01…
1.44E-01 1.45E-01 1.45E-01 1.45E-01 1.46E-01 1.46E-01 1.47E-01 1.47E-01…
1.47E-01 1.48E-01 1.48E-01 1.49E-01 1.49E-01 1.49E-01 1.50E-01 1.50E-01…
1.51E-01 1.51E-01 1.51E-01 1.52E-01 1.52E-01 1.53E-01 1.53E-01 1.53E-01…
1.54E-01 1.54E-01 1.55E-01 1.55E-01 1.55E-01 1.56E-01 1.56E-01 1.57E-01…
1.57E-01 1.57E-01 1.58E-01 1.58E-01 1.59E-01 1.59E-01 1.59E-01 1.60E-01…
1.60E-01 1.61E-01 1.61E-01 1.61E-01 1.62E-01 1.62E-01 1.63E-01 1.63E-01…
1.63E-01 1.64E-01 1.64E-01 1.65E-01 1.65E-01 1.65E-01 1.66E-01 1.66E-01…
1.67E-01 1.67E-01 1.67E-01 1.68E-01 1.68E-01 1.69E-01 1.69E-01 1.69E-01…
1.70E-01 1.70E-01 1.71E-01 1.71E-01 1.71E-01 1.72E-01 1.72E-01 1.73E-01…
1.73E-01 1.73E-01 1.74E-01 1.74E-01 1.75E-01 1.75E-01 1.75E-01 1.76E-01…
1.76E-01 1.77E-01 1.77E-01 1.77E-01 1.78E-01 1.78E-01 1.79E-01 1.79E-01…
1.79E-01 1.80E-01 1.80E-01 1.81E-01 1.81E-01 1.81E-01 1.82E-01 1.82E-01…
1.83E-01 1.83E-01 1.83E-01 1.84E-01 1.84E-01 1.85E-01 1.85E-01 1.85E-01…
1.86E-01 1.86E-01 1.87E-01 1.87E-01 1.87E-01 1.88E-01 1.88E-01 1.89E-01…
1.89E-01 1.89E-01 1.90E-01 1.90E-01 1.91E-01 1.91E-01 1.91E-01 1.92E-01…
1.92E-01 1.93E-01 1.93E-01 1.93E-01 1.94E-01 1.94E-01 1.95E-01 1.95E-01…
1.95E-01 1.96E-01 1.96E-01 1.97E-01 1.97E-01 1.97E-01 1.98E-01 1.98E-01…
1.99E-01 1.99E-01 1.99E-01 2.00E-01 2.00E-01 2.01E-01 2.01E-01 2.01E-01…
2.02E-01 2.02E-01 2.03E-01 2.03E-01 2.03E-01 2.04E-01 2.04E-01 2.05E-01…
2.05E-01 2.05E-01 2.06E-01 2.06E-01 2.07E-01 2.07E-01 2.07E-01 2.08E-01…
2.08E-01 2.09E-01 2.09E-01 2.09E-01 2.10E-01 2.10E-01 2.11E-01 2.11E-01…
2.11E-01 2.12E-01 2.12E-01 2.13E-01 2.13E-01 2.13E-01 2.14E-01 2.14E-01…
2.15E-01 2.15E-01 2.15E-01 2.16E-01 2.16E-01 2.17E-01 2.17E-01 2.17E-01…
2.18E-01 2.18E-01 2.19E-01 2.19E-01 2.19E-01 2.20E-01 2.20E-01 2.21E-01…
2.21E-01 2.21E-01 2.22E-01 2.22E-01 2.23E-01 2.23E-01 2.23E-01 2.24E-01…
2.24E-01 2.25E-01 2.25E-01 2.25E-01 2.26E-01 2.26E-01 2.27E-01 2.27E-01…
2.27E-01 2.28E-01 2.28E-01 2.29E-01 2.29E-01 2.29E-01 2.30E-01 2.30E-01…
2.31E-01 2.31E-01 2.31E-01 2.32E-01 2.32E-01 2.33E-01 2.33E-01 2.33E-01…
2.34E-01 2.34E-01 2.35E-01 2.35E-01 2.35E-01 2.36E-01 2.36E-01 2.37E-01…
2.37E-01 2.37E-01 2.38E-01 2.38E-01 2.39E-01 2.39E-01 2.39E-01 2.40E-01…
2.40E-01 2.41E-01 2.41E-01 2.41E-01 2.42E-01 2.42E-01 2.43E-01 2.43E-01…
2.43E-01 2.44E-01 2.44E-01 2.45E-01 2.45E-01 2.45E-01 2.46E-01 2.46E-01…
2.47E-01 2.47E-01 2.47E-01 2.48E-01 2.48E-01 2.49E-01 2.49E-01 2.49E-01…
2.50E-01 2.50E-01 2.51E-01 2.51E-01 2.51E-01 2.52E-01 2.52E-01 2.53E-01…

```
2.53E-01 2.53E-01 2.54E-01 2.54E-01 2.55E-01 2.55E-01 2.55E-01 2.56E-01…
2.56E-01 2.57E-01 2.57E-01 2.57E-01 2.58E-01 2.58E-01 2.59E-01 2.59E-01…
2.59E-01 2.60E-01 2.60E-01 2.61E-01 2.61E-01 2.61E-01 2.62E-01 2.62E-01…
2.63E-01 2.63E-01 2.63E-01 2.64E-01 2.64E-01 2.65E-01 2.65E-01 2.65E-01…
2.66E-01 2.66E-01 2.67E-01 2.67E-01 2.67E-01 2.68E-01 2.68E-01 2.69E-01…
2.69E-01 2.69E-01 2.70E-01 2.70E-01 2.71E-01 2.71E-01 2.71E-01 2.72E-01…
2.72E-01 2.73E-01 2.73E-01 2.73E-01 2.74E-01 2.74E-01 2.75E-01 2.75E-01…
2.75E-01 2.76E-01 2.76E-01 2.77E-01 2.77E-01 2.77E-01 2.78E-01 2.78E-01…
2.79E-01 2.79E-01 2.79E-01 2.80E-01 2.80E-01 2.81E-01 2.81E-01 2.81E-01…
2.82E-01 2.82E-01 2.83E-01 2.83E-01 2.83E-01 2.84E-01 2.84E-01 2.85E-01…
2.85E-01 2.85E-01 2.86E-01 2.86E-01 2.87E-01 2.87E-01 2.87E-01 2.88E-01…
2.88E-01 2.89E-01 2.89E-01 2.89E-01 2.90E-01 2.90E-01 2.91E-01 2.91E-01…
2.91E-01 2.92E-01 2.92E-01 2.93E-01 2.93E-01 2.93E-01 2.94E-01 2.94E-01…
2.95E-01 2.95E-01 2.95E-01 2.96E-01 2.96E-01 2.97E-01 2.97E-01 2.97E-01…
2.98E-01 2.98E-01 2.99E-01 2.99E-01 2.99E-01 3.00E-01 3.00E-01 3.01E-01…
3.01E-01 3.01E-01 3.02E-01 3.02E-01 3.03E-01 3.03E-01 3.04E-01 3.04E-01…
3.04E-01 3.05E-01 3.05E-01 3.06E-01 3.06E-01 3.06E-01 3.07E-01 3.07E-01…
3.08E-01 3.08E-01 3.08E-01 3.09E-01 3.09E-01 3.10E-01 3.10E-01 3.10E-01…
3.11E-01 3.11E-01 3.12E-01 3.12E-01 3.12E-01 3.13E-01 3.13E-01 3.14E-01…
3.14E-01 3.14E-01 3.15E-01 3.15E-01 3.16E-01 3.16E-01 3.16E-01 3.17E-01…
3.17E-01 3.18E-01 3.18E-01 3.18E-01 3.19E-01 3.19E-01 3.20E-01 3.20E-01…
3.20E-01 3.21E-01 3.21E-01 3.22E-01 3.22E-01 3.22E-01 3.23E-01 3.23E-01…
3.24E-01 3.24E-01 3.24E-01 3.25E-01 3.25E-01 3.26E-01 3.26E-01 3.26E-01…
3.27E-01 3.27E-01 3.28E-01 3.28E-01 3.28E-01 3.29E-01 3.29E-01 3.30E-01…
3.30E-01 3.30E-01 3.31E-01 3.31E-01 3.32E-01 3.32E-01 3.32E-01 3.33E-01…
3.33E-01 3.34E-01 3.34E-01 3.34E-01 3.35E-01 3.35E-01 3.36E-01 3.36E-01…
3.36E-01 3.37E-01 3.37E-01 3.38E-01 3.38E-01 3.38E-01 3.39E-01 3.39E-01…
3.40E-01 3.40E-01 3.40E-01 3.41E-01 3.41E-01 3.42E-01 3.42E-01 3.42E-01…
3.43E-01 3.43E-01 3.44E-01 3.44E-01 3.44E-01 3.45E-01 3.45E-01 3.46E-01…
3.46E-01 3.46E-01 3.47E-01 3.47E-01 3.48E-01 3.48E-01 3.48E-01 3.49E-01…
3.49E-01 3.50E-01 3.50E-01 3.50E-01 3.51E-01 3.51E-01 3.52E-01 3.52E-01…
3.52E-01 3.53E-01 3.53E-01 3.54E-01 3.54E-01 3.54E-01 3.55E-01 3.55E-01…
3.56E-01 3.56E-01 3.56E-01 3.57E-01 3.57E-01 3.58E-01 3.58E-01 3.58E-01…
3.59E-01 3.59E-01 3.60E-01 3.60E-01 3.60E-01 3.61E-01 3.61E-01 3.62E-01…
3.62E-01 3.62E-01 3.63E-01 3.63E-01 3.64E-01 3.64E-01 3.64E-01 3.65E-01…
3.65E-01 3.66E-01 3.66E-01 3.66E-01 3.67E-01 3.67E-01 3.68E-01 3.68E-01…
3.68E-01 3.69E-01 3.69E-01 3.70E-01 3.70E-01 3.70E-01 3.71E-01 3.71E-01…
3.72E-01 3.72E-01 3.72E-01 3.73E-01 3.73E-01 3.74E-01 3.74E-01 3.74E-01…
3.75E-01 3.75E-01 3.76E-01 3.76E-01 3.76E-01 3.77E-01 3.77E-01 3.78E-01…
3.78E-01 3.78E-01 3.79E-01 3.79E-01 3.80E-01 3.80E-01 3.80E-01 3.81E-01…
3.81E-01 3.82E-01 3.82E-01 3.82E-01 3.83E-01 3.83E-01 3.84E-01 3.84E-01…
3.84E-01 3.85E-01 3.85E-01 3.86E-01 3.86E-01 3.86E-01 3.87E-01 3.87E-01…
3.88E-01 3.88E-01 3.88E-01 3.89E-01 3.89E-01 3.90E-01 3.90E-01 3.90E-01…
3.91E-01 3.91E-01 3.92E-01 3.92E-01 3.92E-01 3.93E-01 3.93E-01 3.94E-01…
3.94E-01 3.94E-01 3.95E-01 3.95E-01 3.96E-01 3.96E-01 3.96E-01 3.97E-01…
3.97E-01 3.98E-01 3.98E-01 3.98E-01 3.99E-01 3.99E-01 4.00E-01 4.00E-01];
V_uni =[-5.36E+00-5.36E+00 -5.36E+00 -5.36E+00 -5.36E+00 -5.36E+00…
-5.36E+00 -5.36E+00 -5.36E+00 -5.36E+00 -5.36E+00 -5.36E+00 -5.36E+00…
-5.36E+00 -5.36E+00 -5.36E+00 -5.36E+00 -5.36E+00 -5.36E+00 -5.36E+00…
-5.36E+00 -5.36E+00 -5.36E+00 -5.36E+00 -5.36E+00 -5.36E+00 -5.36E+00…
-5.36E+00 -5.36E+00 -5.36E+00 -5.36E+00 -5.36E+00 -5.36E+00 -5.36E+00…
-5.36E+00 -5.36E+00 -5.36E+00 -5.36E+00 -5.36E+00 -5.36E+00 -5.36E+00…
-5.36E+00 -5.36E+00 -5.36E+00 -5.36E+00 -5.36E+00 -5.36E+00 -5.36E+00…
-5.36E+00 -5.36E+00 -5.36E+00 -5.36E+00 -5.36E+00 -5.36E+00 -5.36E+00…
```

```
-5.36E+00 -5.36E+00 -5.36E+00 -5.36E+00 -5.36E+00 -5.36E+00 -5.36E+00…
-5.36E+00 -5.36E+00 -5.36E+00 -5.36E+00 -5.36E+00 -5.36E+00 -5.36E+00…
-5.36E+00 -5.36E+00 -5.36E+00 -5.36E+00 -5.36E+00 -5.36E+00 -5.36E+00…
-5.36E+00 -5.36E+00 -5.36E+00 -5.36E+00 -5.36E+00 -5.36E+00 -5.36E+00…
-5.36E+00 -5.36E+00 -5.36E+00 -5.36E+00 -5.36E+00 -5.36E+00 -5.36E+00…
-5.36E+00 -5.36E+00 -5.36E+00 -5.36E+00 -5.36E+00 -5.36E+00 -5.36E+00…
-5.36E+00 -5.36E+00 -5.36E+00 -5.36E+00 -5.36E+00 -5.36E+00 -5.36E+00…
-5.36E+00 -5.36E+00 -5.36E+00 -5.36E+00 -5.36E+00 -5.36E+00 -5.36E+00…
-5.36E+00 -5.36E+00 -5.36E+00 -5.36E+00 -5.36E+00 -5.36E+00 -5.36E+00…
-5.36E+00 -5.36E+00 -5.36E+00 -5.36E+00 -5.36E+00 -5.36E+00 -5.36E+00…
-5.36E+00 -5.36E+00 -5.36E+00 -5.36E+00 -5.36E+00 -5.36E+00 -5.36E+00…
-5.36E+00 -5.36E+00 -5.36E+00 -5.36E+00 -5.36E+00 -5.36E+00 -5.36E+00…
-5.36E+00 -5.36E+00 -5.36E+00 -5.36E+00 -5.36E+00 -5.36E+00 -5.36E+00…
-5.36E+00 -5.36E+00 -5.36E+00 -5.36E+00 -5.36E+00 -5.36E+00 -5.36E+00…
-5.36E+00 -5.36E+00 -5.36E+00 -5.36E+00 -5.36E+00 -5.36E+00 -5.36E+00…
-5.36E+00 -5.36E+00 -5.36E+00 -5.36E+00 -5.36E+00 -5.36E+00 -5.36E+00…
-5.36E+00 -5.36E+00 -5.36E+00 -5.36E+00 -5.36E+00 -5.36E+00 -5.36E+00…
-5.36E+00 -5.36E+00 -5.36E+00 -5.36E+00 -5.36E+00 -5.36E+00 -5.36E+00…
-5.36E+00 -5.36E+00 -5.36E+00 -5.36E+00 -5.36E+00 -5.36E+00 -5.36E+00…
-5.36E+00 -5.36E+00 -5.36E+00 -5.36E+00 -5.36E+00 -5.36E+00 -5.36E+00…
-5.36E+00 -5.36E+00 -5.36E+00 -5.36E+00 -5.36E+00 -5.36E+00 -5.36E+00…
-5.36E+00 -5.36E+00 -5.36E+00 -5.36E+00 -5.36E+00 -5.36E+00 -5.36E+00…
-5.36E+00 -5.36E+00 -5.36E+00 -5.36E+00 -5.36E+00 -5.36E+00 -5.36E+00…
-5.36E+00 -5.36E+00 -5.36E+00 -5.36E+00 -5.36E+00 -5.36E+00 -5.36E+00…
-5.36E+00 -5.36E+00 -5.36E+00 -5.36E+00 -5.36E+00 -5.36E+00 -5.36E+00…
-5.36E+00 -5.36E+00 -5.36E+00 -5.36E+00 -5.36E+00 -5.36E+00 -5.36E+00…
-5.36E+00 -5.36E+00 -5.36E+00 -5.36E+00 -5.36E+00 -5.36E+00 -5.36E+00…
-5.36E+00 -5.36E+00 -5.36E+00 -5.36E+00 -5.36E+00 -5.36E+00 -5.36E+00…
-5.36E+00 -5.36E+00 -5.36E+00 -5.36E+00 -5.36E+00 -5.36E+00 -5.36E+00…
-5.36E+00 -5.36E+00 -5.36E+00 -5.36E+00 -5.36E+00 -5.36E+00 -5.36E+00…
-5.36E+00 -5.36E+00 -5.36E+00 -5.36E+00 -5.36E+00 -5.36E+00 -5.36E+00…
-5.36E+00 -5.36E+00 -5.36E+00 -5.36E+00 -5.36E+00 -5.36E+00 -5.36E+00…
-5.36E+00 -5.36E+00 -5.36E+00 -5.36E+00 -5.36E+00 -5.36E+00 -5.36E+00…
-5.36E+00 -5.36E+00 -5.36E+00 -5.36E+00 -5.36E+00 -5.36E+00 -5.36E+00…
-5.36E+00 -5.36E+00 -5.36E+00 -5.36E+00 -5.36E+00 -5.36E+00 -5.36E+00…
-5.36E+00 -5.36E+00 -5.36E+00 -5.36E+00 -5.36E+00 -5.36E+00 -5.36E+00…
-5.36E+00 -5.36E+00 -5.36E+00 -5.36E+00 -5.36E+00 -5.36E+00 -5.36E+00…
-5.36E+00 -5.36E+00 -5.36E+00 -5.36E+00 -5.36E+00 -5.36E+00 -5.36E+00…
-5.36E+00 -5.36E+00 -5.36E+00 -5.36E+00 -5.36E+00 -5.36E+00 -5.36E+00…
-5.36E+00 -5.36E+00 -5.36E+00 -5.36E+00 -5.36E+00 -5.36E+00 -5.36E+00…
-5.36E+00 -5.36E+00 -5.36E+00 -5.36E+00 -5.36E+00 -5.36E+00 -5.36E+00…
-5.36E+00 -5.36E+00 -5.36E+00 -5.36E+00 -5.36E+00 -5.36E+00 -5.36E+00…
-5.36E+00 -5.36E+00 -5.36E+00 -5.36E+00 -5.36E+00 -5.36E+00 -5.36E+00…
-5.36E+00 -5.36E+00 -5.36E+00 -5.36E+00 -5.36E+00 -5.36E+00 -5.36E+00…
-5.36E+00 -5.36E+00 -5.36E+00 -5.36E+00 -5.36E+00 -5.36E+00 -5.36E+00…
-5.36E+00 -5.36E+00 -5.36E+00 -5.36E+00 -5.36E+00 -5.36E+00 -5.36E+00…
-5.36E+00 -5.36E+00 -5.36E+00 -5.36E+00 -5.36E+00 -5.36E+00 -5.36E+00…
-5.36E+00 -5.36E+00 -5.36E+00 -5.36E+00 -5.36E+00 -5.36E+00 -5.36E+00…
-5.36E+00 -5.36E+00 -5.36E+00 -5.36E+00 -5.36E+00 -5.36E+00 -5.36E+00…
-5.36E+00 -5.36E+00 -5.36E+00 -5.36E+00 -5.36E+00 -5.36E+00 -5.36E+00…
-5.36E+00 -5.36E+00 -5.36E+00 -5.36E+00 -5.36E+00 -5.36E+00 -5.36E+00…
-5.36E+00 -5.36E+00 -5.36E+00 -5.36E+00 -5.36E+00 -5.36E+00 -5.36E+00…
-5.36E+00 -5.36E+00 -5.36E+00 -5.36E+00 -5.36E+00 -5.36E+00 -5.36E+00…
-5.36E+00 -5.36E+00 -5.36E+00 -5.36E+00 -5.36E+00 -5.36E+00 -5.36E+00…
```

```
-5.36E+00 -5.36E+00 -5.36E+00 -5.36E+00 -5.36E+00 -5.36E+00 -5.36E+00…
-5.36E+00 -5.36E+00 -5.36E+00 -5.36E+00 -5.36E+00 -5.36E+00 -5.36E+00…
-5.36E+00 -5.36E+00 -5.36E+00 -5.36E+00 -5.36E+00 -5.36E+00 -5.36E+00…
-5.36E+00 -5.36E+00 -5.36E+00 -5.36E+00 -5.36E+00 -5.36E+00 -5.36E+00…
-5.36E+00 -5.36E+00 -5.36E+00 -5.36E+00 -5.36E+00 -5.36E+00 -5.36E+00…
-5.36E+00 -5.36E+00 -5.36E+00 -5.36E+00 -5.36E+00 -5.36E+00 -5.36E+00…
-5.36E+00 -5.36E+00 -5.36E+00 -5.36E+00 -5.36E+00 -5.36E+00 -5.36E+00…
-5.36E+00 -5.36E+00 -5.36E+00 -5.36E+00 -5.36E+00 -5.36E+00 -5.36E+00…
-5.36E+00 -5.36E+00 -5.36E+00 -5.36E+00 -5.36E+00 -5.36E+00 -5.36E+00…
-5.36E+00 -5.36E+00 -5.36E+00 -5.36E+00 -5.36E+00 -5.36E+00 -5.36E+00…
-5.36E+00 -5.36E+00 -5.36E+00 -5.36E+00 -5.36E+00 -5.36E+00 -5.36E+00…
-5.36E+00 -5.36E+00 -5.36E+00 -5.36E+00 -5.36E+00 -5.36E+00 -5.36E+00…
-5.36E+00 -5.36E+00 -5.36E+00 -5.36E+00 -5.36E+00 -5.36E+00 -5.36E+00…
-5.36E+00 -5.36E+00 -5.36E+00 -5.36E+00 -5.36E+00 -5.36E+00 -5.36E+00…
-5.36E+00 -5.36E+00 -5.36E+00 -5.36E+00 -5.36E+00 -5.36E+00 -5.36E+00…
-5.36E+00 -5.36E+00 -5.36E+00 -5.36E+00 -5.36E+00 -5.36E+00 -5.36E+00…
-5.36E+00 -5.36E+00 -5.36E+00 -5.36E+00 -5.36E+00 -5.36E+00 -5.36E+00…
-5.36E+00 -5.36E+00 -5.36E+00 -5.36E+00 -5.36E+00 -5.36E+00 -5.36E+00…
-5.36E+00 -5.36E+00 -5.36E+00 -5.36E+00 -5.36E+00 -5.36E+00 -5.36E+00…
-5.36E+00 -5.36E+00 -5.36E+00 -5.36E+00 -5.36E+00 -5.36E+00 -5.36E+00…
-5.36E+00 -5.36E+00 -5.36E+00 -5.36E+00 -5.36E+00 -5.36E+00 -5.36E+00…
-5.36E+00 -5.36E+00 -5.36E+00 -5.36E+00 -5.36E+00 -5.36E+00 -5.36E+00…
-5.36E+00 -5.36E+00 -5.36E+00 -5.36E+00 -5.36E+00 -5.36E+00 -5.36E+00…
-5.36E+00 -5.36E+00 -5.36E+00 -5.36E+00 -5.36E+00 -5.36E+00 -5.36E+00…
-5.36E+00 -5.36E+00 -5.36E+00 -5.36E+00 -5.36E+00 -5.36E+00 -5.36E+00…
-5.36E+00 -5.36E+00 -5.36E+00 -5.36E+00 -5.36E+00 -5.36E+00 -5.36E+00…
-5.36E+00 -5.36E+00 -5.36E+00 -5.36E+00 -5.36E+00 -5.36E+00 -5.36E+00…
-5.36E+00 -5.36E+00 -5.36E+00 -5.36E+00 -5.36E+00 -5.36E+00 -5.36E+00…
-5.36E+00 -5.36E+00 -5.36E+00 -5.36E+00 -5.36E+00 -5.36E+00 -5.36E+00…
-5.36E+00 -5.36E+00 -5.36E+00 -5.36E+00 -5.36E+00 -5.36E+00 -5.36E+00…
-5.36E+00 -5.36E+00 -5.36E+00 -5.36E+00 -5.36E+00 -5.36E+00 -5.36E+00…
-5.36E+00 -5.36E+00 -5.36E+00 -5.36E+00 -5.36E+00 -5.36E+00 -5.36E+00…
-5.36E+00 -5.36E+00 -5.36E+00 -5.36E+00 -5.36E+00 -5.36E+00 -5.36E+00…
-5.36E+00 -5.36E+00 -5.36E+00 -5.36E+00 -5.36E+00 -5.36E+00 -5.36E+00…
-5.36E+00 -5.36E+00 -5.36E+00 -5.36E+00 -5.36E+00 -5.36E+00 -5.36E+00…
-5.36E+00 -5.36E+00 -5.36E+00 -5.36E+00 -5.36E+00 -5.36E+00 -5.36E+00…
-5.36E+00 -5.36E+00 -5.36E+00 -5.36E+00 -5.35E+00 -5.35E+00 -5.35E+00…
-5.35E+00 -5.35E+00 -5.35E+00 -5.35E+00 -5.35E+00 -5.35E+00 -5.35E+00…
-5.35E+00 -5.35E+00 -5.35E+00 -5.35E+00 -5.35E+00 -5.35E+00 -5.35E+00…
-5.35E+00 -5.35E+00 -5.35E+00 -5.35E+00 -5.35E+00 -5.35E+00 -5.35E+00…
-5.35E+00 -5.35E+00 -5.35E+00 -5.35E+00 -5.35E+00 -5.35E+00 -5.35E+00…
-5.35E+00 -5.35E+00 -5.35E+00 -5.35E+00 -5.35E+00 -5.35E+00 -5.35E+00…
-5.35E+00 -5.35E+00 -5.35E+00 -5.35E+00 -5.35E+00 -5.35E+00 -5.35E+00…
-5.35E+00 -5.35E+00 -5.35E+00 -5.35E+00 -5.35E+00 -5.35E+00 -5.35E+00…
-5.35E+00 -5.35E+00 -5.35E+00 -5.35E+00 -5.35E+00 -5.35E+00 -5.35E+00…
-5.35E+00 -5.35E+00 -5.35E+00 -5.35E+00 -5.35E+00 -5.35E+00 -5.35E+00…
-5.35E+00 -5.35E+00 -5.35E+00 -5.35E+00 -5.35E+00 -5.35E+00 -5.35E+00…
-5.34E+00 -5.34E+00 -5.34E+00 -5.34E+00 -5.34E+00 -5.34E+00 -5.34E+00…
-5.34E+00 -5.34E+00 -5.34E+00 -5.34E+00 -5.34E+00 -5.34E+00 -5.34E+00…
-5.34E+00 -5.34E+00 -5.34E+00 -5.34E+00 -5.34E+00 -5.34E+00 -5.34E+00…
-5.34E+00 -5.34E+00 -5.34E+00 -5.34E+00 -5.34E+00 -5.34E+00 -5.34E+00…
-5.34E+00 -5.34E+00 -5.34E+00 -5.33E+00 -5.33E+00 -5.33E+00 -5.33E+00…
-5.33E+00 -5.33E+00 -5.33E+00 -5.33E+00 -5.33E+00 -5.33E+00 -5.33E+00…
-5.33E+00 -5.33E+00 -5.33E+00 -5.33E+00 -5.33E+00 -5.33E+00 -5.33E+00…
```

```
-5.33E+00 -5.33E+00 -5.32E+00 -5.32E+00 -5.32E+00 -5.32E+00 -5.32E+00…
-5.32E+00 -5.32E+00 -5.32E+00 -5.32E+00 -5.32E+00 -5.32E+00 -5.32E+00…
-5.32E+00 -5.32E+00 -5.32E+00 -5.31E+00 -5.31E+00 -5.31E+00 -5.31E+00…
-5.31E+00 -5.31E+00 -5.31E+00 -5.31E+00 -5.31E+00 -5.31E+00 -5.31E+00…
-5.30E+00 -5.30E+00 -5.30E+00 -5.30E+00 -5.30E+00 -5.30E+00 -5.30E+00…
-5.30E+00 -5.30E+00 -5.30E+00 -5.29E+00 -5.29E+00 -5.29E+00 -5.29E+00…
-5.29E+00 -5.29E+00 -5.29E+00 -5.28E+00 -5.28E+00 -5.28E+00 -5.28E+00…
-5.28E+00 -5.28E+00 -5.27E+00 -5.27E+00 -5.26E+00 -5.26E+00 -5.26E+00…
-5.25E+00 -5.25E+00 -5.25E+00 -5.24E+00 -5.24E+00 -5.24E+00 -5.23E+00…
-5.20E+00 -5.17E+00 -5.13E+00 -5.09E+00 -5.06E+00 -5.02E+00 -4.99E+00…
-4.95E+00 -4.92E+00 -4.88E+00 -4.84E+00 -4.81E+00 -4.77E+00 4.03E+00…
4.13E+00 4.24E+00 4.34E+00 4.44E+00 4.55E+00 4.65E+00 4.76E+00 4.86E+00…
4.96E+00 5.07E+00 5.05E+00 5.01E+00 4.98E+00 4.94E+00 4.90E+00 4.86E+00…
4.82E+00 4.77E+00 4.73E+00 4.68E+00 4.64E+00 4.59E+00 4.56E+00 4.49E+00…
4.41E+00 4.32E+00 4.24E+00 4.17E+00 4.11E+00 4.04E+00 3.98E+00 3.91E+00…
3.84E+00 3.77E+00 3.70E+00 3.63E+00 3.56E+00 3.49E+00 3.42E+00 3.33E+00…
3.26E+00 3.22E+00 3.19E+00 3.14E+00 3.10E+00 3.05E+00 3.00E+00 2.95E+00…
2.90E+00 2.85E+00 2.80E+00 2.75E+00 2.70E+00 2.65E+00 2.62E+00 2.59E+00…
2.55E+00 2.52E+00 2.48E+00 2.44E+00 2.41E+00 2.38E+00 2.35E+00 2.32E+00…
2.28E+00 2.25E+00 2.22E+00 2.19E+00 2.15E+00 2.12E+00 2.09E+00 2.06E+00…
2.04E+00 2.02E+00 2.00E+00 1.98E+00 1.96E+00 1.93E+00 1.91E+00 1.88E+00…
1.86E+00 1.83E+00 1.81E+00 1.79E+00 1.76E+00 1.74E+00 1.72E+00 1.70E+00…
1.68E+00 1.66E+00 1.64E+00 1.62E+00 1.60E+00 1.58E+00 1.57E+00 1.55E+00…
1.53E+00 1.52E+00 1.51E+00 1.50E+00 1.49E+00 1.47E+00 1.46E+00 1.45E+00…
1.44E+00 1.43E+00 1.42E+00 1.40E+00 1.39E+00 1.38E+00 1.37E+00 1.36E+00];
figure(4)
plot(Z./0.355,V_uni)
hold on
xlabel('Radius [m]')
ylabel('Axial Velocity [m/s]')
V_polyax = [-3.69E-02 -3.66E-02 -3.64E-02…
-3.82E-02 -4.09E-02 -4.36E-02 -4.62E-02 -4.89E-02 -5.16E-02 -5.42E-02…
-5.69E-02 -5.95E-02 -6.21E-02 -6.48E-02 -6.74E-02 -7.00E-02 -7.26E-02…
-7.52E-02 -7.78E-02 -8.11E-02 -8.66E-02 -9.22E-02 -9.78E-02 -1.03E-01…
-1.10E-01 -1.17E-01 -1.25E-01 -1.33E-01 -1.40E-01 -1.48E-01 -1.56E-01…
-1.64E-01 -1.72E-01 -1.80E-01 -1.87E-01 -1.95E-01 -2.03E-01 -2.12E-01…
-2.24E-01 -2.36E-01 -2.48E-01 -2.59E-01 -2.71E-01 -2.83E-01 -2.95E-01…
-3.07E-01 -3.19E-01 -3.31E-01 -3.43E-01 -3.55E-01 -3.67E-01 -3.79E-01…
-3.91E-01 -4.04E-01 -4.17E-01 -4.32E-01 -4.47E-01 -4.66E-01 -4.85E-01…
-5.05E-01 -5.25E-01 -5.45E-01 -5.64E-01 -5.84E-01 -6.04E-01 -6.24E-01…
-6.43E-01 -6.63E-01 -6.83E-01 -7.03E-01 -7.22E-01 -7.42E-01 -7.62E-01…
-7.82E-01 -8.02E-01 -8.21E-01 -8.41E-01 -8.61E-01 -8.81E-01 -9.02E-01…
-9.24E-01 -9.46E-01 -9.68E-01 -9.91E-01 -1.01E+00 -1.04E+00 -1.06E+00…
-1.08E+00 -1.11E+00 -1.13E+00 -1.16E+00 -1.18E+00 -1.20E+00 -1.23E+00…
-1.25E+00 -1.27E+00 -1.30E+00 -1.32E+00 -1.34E+00 -1.37E+00 -1.39E+00…
-1.42E+00 -1.44E+00 -1.46E+00 -1.49E+00 -1.51E+00 -1.54E+00 -1.57E+00…
-1.59E+00 -1.62E+00 -1.64E+00 -1.67E+00 -1.69E+00 -1.72E+00 -1.74E+00…
-1.77E+00 -1.79E+00 -1.82E+00 -1.84E+00 -1.87E+00 -1.90E+00 -1.92E+00…
-1.95E+00 -1.98E+00 -2.01E+00 -2.03E+00 -2.06E+00 -2.09E+00 -2.12E+00…
-2.15E+00 -2.17E+00 -2.20E+00 -2.23E+00 -2.26E+00 -2.29E+00 -2.31E+00…
-2.34E+00 -2.37E+00 -2.40E+00 -2.43E+00 -2.45E+00 -2.48E+00 -2.51E+00…
-2.54E+00 -2.57E+00 -2.60E+00 -2.63E+00 -2.66E+00 -2.69E+00 -2.72E+00…
-2.75E+00 -2.78E+00 -2.81E+00 -2.84E+00 -2.87E+00 -2.89E+00 -2.92E+00…
-2.95E+00 -2.98E+00 -3.01E+00 -3.04E+00 -3.07E+00 -3.10E+00 -3.13E+00…
```

-3.16E+00 -3.19E+00 -3.22E+00 -3.25E+00 -3.28E+00 -3.31E+00 -3.35E+00…
-3.38E+00 -3.41E+00 -3.44E+00 -3.47E+00 -3.50E+00 -3.53E+00 -3.56E+00…
-3.59E+00 -3.62E+00 -3.65E+00 -3.68E+00 -3.71E+00 -3.74E+00 -3.77E+00…
-3.80E+00 -3.84E+00 -3.87E+00 -3.90E+00 -3.93E+00 -3.96E+00 -3.99E+00…
-4.02E+00 -4.05E+00 -4.09E+00 -4.12E+00 -4.15E+00 -4.18E+00 -4.21E+00…
-4.24E+00 -4.27E+00 -4.30E+00 -4.34E+00 -4.37E+00 -4.40E+00 -4.43E+00…
-4.46E+00 -4.49E+00 -4.52E+00 -4.55E+00 -4.58E+00 -4.61E+00 -4.64E+00…
-4.68E+00 -4.71E+00 -4.74E+00 -4.77E+00 -4.80E+00 -4.83E+00 -4.86E+00…
-4.89E+00 -4.92E+00 -4.95E+00 -4.98E+00 -5.01E+00 -5.04E+00 -5.07E+00…
-5.10E+00 -5.13E+00 -5.16E+00 -5.19E+00 -5.22E+00 -5.25E+00 -5.28E+00…
-5.31E+00 -5.34E+00 -5.37E+00 -5.40E+00 -5.43E+00 -5.46E+00 -5.49E+00…
-5.52E+00 -5.55E+00 -5.58E+00 -5.61E+00 -5.64E+00 -5.67E+00 -5.70E+00…
-5.73E+00 -5.76E+00 -5.79E+00 -5.81E+00 -5.84E+00 -5.87E+00 -5.90E+00…
-5.93E+00 -5.96E+00 -5.99E+00 -6.02E+00 -6.05E+00 -6.07E+00 -6.10E+00…
-6.13E+00 -6.16E+00 -6.19E+00 -6.22E+00 -6.25E+00 -6.27E+00 -6.30E+00…
-6.33E+00 -6.36E+00 -6.38E+00 -6.41E+00 -6.44E+00 -6.47E+00 -6.49E+00…
-6.52E+00 -6.55E+00 -6.58E+00 -6.60E+00 -6.63E+00 -6.66E+00 -6.68E+00…
-6.71E+00 -6.74E+00 -6.76E+00 -6.79E+00 -6.81E+00 -6.84E+00 -6.87E+00…
-6.89E+00 -6.92E+00 -6.94E+00 -6.97E+00 -7.00E+00 -7.02E+00 -7.05E+00…
-7.07E+00 -7.10E+00 -7.12E+00 -7.15E+00 -7.17E+00 -7.20E+00 -7.22E+00…
-7.25E+00 -7.27E+00 -7.30E+00 -7.32E+00 -7.34E+00 -7.37E+00 -7.39E+00…
-7.41E+00 -7.44E+00 -7.46E+00 -7.49E+00 -7.51E+00 -7.53E+00 -7.55E+00…
-7.58E+00 -7.60E+00 -7.62E+00 -7.64E+00 -7.67E+00 -7.69E+00 -7.71E+00…
-7.73E+00 -7.75E+00 -7.78E+00 -7.80E+00 -7.82E+00 -7.84E+00 -7.86E+00…
-7.88E+00 -7.90E+00 -7.93E+00 -7.95E+00 -7.97E+00 -7.99E+00 -8.01E+00…
-8.03E+00 -8.05E+00 -8.07E+00 -8.09E+00 -8.11E+00 -8.13E+00 -8.15E+00…
-8.16E+00 -8.18E+00 -8.20E+00 -8.22E+00 -8.24E+00 -8.26E+00 -8.28E+00…
-8.29E+00 -8.31E+00 -8.33E+00 -8.35E+00 -8.37E+00 -8.38E+00 -8.40E+00…
-8.42E+00 -8.43E+00 -8.45E+00 -8.47E+00 -8.48E+00 -8.50E+00 -8.52E+00…
-8.53E+00 -8.55E+00 -8.57E+00 -8.58E+00 -8.60E+00 -8.61E+00 -8.63E+00…
-8.64E+00 -8.66E+00 -8.67E+00 -8.69E+00 -8.70E+00 -8.71E+00 -8.73E+00…
-8.74E+00 -8.76E+00 -8.77E+00 -8.78E+00 -8.80E+00 -8.81E+00 -8.82E+00…
-8.84E+00 -8.85E+00 -8.86E+00 -8.87E+00 -8.88E+00 -8.90E+00 -8.91E+00…
-8.92E+00 -8.93E+00 -8.94E+00 -8.96E+00 -8.97E+00 -8.98E+00 -8.99E+00…
-9.00E+00 -9.01E+00 -9.02E+00 -9.03E+00 -9.04E+00 -9.05E+00 -9.06E+00…
-9.07E+00 -9.08E+00 -9.08E+00 -9.09E+00 -9.10E+00 -9.11E+00 -9.12E+00…
-9.13E+00 -9.14E+00 -9.14E+00 -9.15E+00 -9.16E+00 -9.17E+00 -9.17E+00…
-9.18E+00 -9.19E+00 -9.20E+00 -9.20E+00 -9.21E+00 -9.21E+00 -9.22E+00…
-9.23E+00 -9.23E+00 -9.24E+00 -9.24E+00 -9.25E+00 -9.25E+00 -9.26E+00…
-9.26E+00 -9.27E+00 -9.27E+00 -9.27E+00 -9.28E+00 -9.28E+00 -9.29E+00…
-9.29E+00 -9.29E+00 -9.30E+00 -9.30E+00 -9.30E+00 -9.30E+00 -9.31E+00…
-9.31E+00 -9.31E+00 -9.31E+00 -9.31E+00 -9.32E+00 -9.32E+00 -9.32E+00…
-9.32E+00 -9.32E+00 -9.32E+00 -9.32E+00 -9.32E+00 -9.32E+00 -9.32E+00…
-9.32E+00 -9.32E+00 -9.32E+00 -9.32E+00 -9.32E+00 -9.32E+00 -9.32E+00…
-9.32E+00 -9.31E+00 -9.31E+00 -9.31E+00 -9.31E+00 -9.30E+00 -9.30E+00…
-9.30E+00 -9.30E+00 -9.29E+00 -9.29E+00 -9.29E+00 -9.28E+00 -9.28E+00…
-9.28E+00 -9.27E+00 -9.27E+00 -9.26E+00 -9.26E+00 -9.25E+00 -9.25E+00…
-9.24E+00 -9.24E+00 -9.23E+00 -9.23E+00 -9.22E+00 -9.21E+00 -9.21E+00…
-9.20E+00 -9.20E+00 -9.19E+00 -9.18E+00 -9.18E+00 -9.17E+00 -9.16E+00…
-9.15E+00 -9.14E+00 -9.14E+00 -9.13E+00 -9.12E+00 -9.11E+00 -9.10E+00…
-9.10E+00 -9.09E+00 -9.08E+00 -9.07E+00 -9.06E+00 -9.05E+00 -9.04E+00…
-9.03E+00 -9.02E+00 -9.01E+00 -9.00E+00 -8.99E+00 -8.98E+00 -8.97E+00…
-8.96E+00 -8.95E+00 -8.93E+00 -8.92E+00 -8.91E+00 -8.90E+00 -8.89E+00…
-8.87E+00 -8.86E+00 -8.85E+00 -8.84E+00 -8.82E+00 -8.81E+00 -8.80E+00…

-8.78E+00 -8.77E+00 -8.76E+00 -8.74E+00 -8.73E+00 -8.72E+00 -8.70E+00…
-8.69E+00 -8.67E+00 -8.66E+00 -8.64E+00 -8.63E+00 -8.61E+00 -8.60E+00…
-8.58E+00 -8.57E+00 -8.55E+00 -8.53E+00 -8.52E+00 -8.50E+00 -8.48E+00…
-8.47E+00 -8.45E+00 -8.44E+00 -8.42E+00 -8.40E+00 -8.38E+00 -8.36E+00…
-8.35E+00 -8.33E+00 -8.31E+00 -8.29E+00 -8.28E+00 -8.26E+00 -8.24E+00…
-8.22E+00 -8.20E+00 -8.18E+00 -8.16E+00 -8.14E+00 -8.12E+00 -8.10E+00…
-8.09E+00 -8.07E+00 -8.05E+00 -8.02E+00 -8.00E+00 -7.98E+00 -7.96E+00…
-7.94E+00 -7.92E+00 -7.90E+00 -7.88E+00 -7.86E+00 -7.84E+00 -7.82E+00…
-7.79E+00 -7.77E+00 -7.75E+00 -7.73E+00 -7.71E+00 -7.69E+00 -7.66E+00…
-7.64E+00 -7.62E+00 -7.59E+00 -7.57E+00 -7.55E+00 -7.53E+00 -7.50E+00…
-7.48E+00 -7.46E+00 -7.43E+00 -7.41E+00 -7.38E+00 -7.36E+00 -7.34E+00…
-7.31E+00 -7.29E+00 -7.26E+00 -7.24E+00 -7.21E+00 -7.19E+00 -7.16E+00…
-7.14E+00 -7.11E+00 -7.09E+00 -7.06E+00 -7.04E+00 -7.01E+00 -6.99E+00…
-6.96E+00 -6.94E+00 -6.91E+00 -6.88E+00 -6.86E+00 -6.83E+00 -6.80E+00…
-6.78E+00 -6.75E+00 -6.72E+00 -6.70E+00 -6.67E+00 -6.64E+00 -6.62E+00…
-6.59E+00 -6.56E+00 -6.53E+00 -6.51E+00 -6.48E+00 -6.45E+00 -6.42E+00…
-6.40E+00 -6.37E+00 -6.34E+00 -6.31E+00 -6.28E+00 -6.25E+00 -6.23E+00…
-6.20E+00 -6.17E+00 -6.14E+00 -6.11E+00 -6.08E+00 -6.06E+00 -6.03E+00…
-6.00E+00 -5.97E+00 -5.94E+00 -5.91E+00 -5.88E+00 -5.85E+00 -5.82E+00…
-5.79E+00 -5.76E+00 -5.73E+00 -5.70E+00 -5.67E+00 -5.64E+00 -5.61E+00…
-5.58E+00 -5.55E+00 -5.52E+00 -5.49E+00 -5.46E+00 -5.43E+00 -5.40E+00…
-5.37E+00 -5.34E+00 -5.31E+00 -5.28E+00 -5.25E+00 -5.22E+00 -5.19E+00…
-5.16E+00 -5.13E+00 -5.10E+00 -5.07E+00 -5.03E+00 -5.00E+00 -4.97E+00…
-4.94E+00 -4.91E+00 -4.88E+00 -4.85E+00 -4.82E+00 -4.79E+00 -4.76E+00…
-4.72E+00 -4.69E+00 -4.66E+00 -4.63E+00 -4.60E+00 -4.57E+00 -4.54E+00…
-4.51E+00 -4.48E+00 -4.45E+00 -4.42E+00 -4.39E+00 -4.35E+00 -4.32E+00…
-4.29E+00 -4.26E+00 -4.23E+00 -4.20E+00 -4.17E+00 -4.14E+00 -4.11E+00…
-4.08E+00 -4.05E+00 -4.02E+00 -3.99E+00 -3.96E+00 -3.93E+00 -3.90E+00…
-3.87E+00 -3.84E+00 -3.81E+00 -3.78E+00 -3.75E+00 -3.72E+00 -3.69E+00…
-3.66E+00 -3.63E+00 -3.60E+00 -3.57E+00 -3.54E+00 -3.51E+00 -3.47E+00…
-3.44E+00 -3.41E+00 -3.38E+00 -3.35E+00 -3.32E+00 -3.29E+00 -3.26E+00…
-3.22E+00 -3.19E+00 -3.16E+00 -3.13E+00 -3.10E+00 -3.07E+00 -3.04E+00…
-3.01E+00 -2.98E+00 -2.95E+00 -2.92E+00 -2.89E+00 -2.86E+00 -2.83E+00…
-2.80E+00 -2.77E+00 -2.74E+00 -2.71E+00 -2.69E+00 -2.66E+00 -2.63E+00…
-2.60E+00 -2.57E+00 -2.54E+00 -2.52E+00 -2.49E+00 -2.46E+00 -2.44E+00…
-2.41E+00 -2.39E+00 -2.36E+00 -2.33E+00 -2.31E+00 -2.28E+00 -2.26E+00…
-2.23E+00 -2.20E+00 -2.18E+00 -2.15E+00 -2.13E+00 -2.10E+00 -2.08E+00…
-2.05E+00 -2.03E+00 -2.00E+00 -1.97E+00 -1.95E+00 -1.92E+00 -1.90E+00…
-1.87E+00 -1.85E+00 -1.82E+00 -1.79E+00 -1.77E+00 -1.74E+00 -1.71E+00…
-1.69E+00 -1.66E+00 -1.63E+00 -1.61E+00 -1.58E+00 -1.55E+00 -1.53E+00…
-1.50E+00 -1.47E+00 -1.44E+00 -1.41E+00 -1.38E+00 -1.35E+00 -1.32E+00…
-1.29E+00 -1.26E+00 -1.23E+00 -1.21E+00 -1.18E+00 -1.14E+00 -1.11E+00…
-1.08E+00 -1.05E+00 -1.01E+00 -9.79E-01 -9.46E-01 -9.13E-01 -8.79E-01…
-8.46E-01 -8.13E-01 -7.80E-01 -7.47E-01 -7.11E-01 -6.72E-01 -6.33E-01…
-5.94E-01 -5.54E-01 -5.15E-01 -4.76E-01 -4.37E-01 -3.98E-01 -3.59E-01…
-3.20E-01 -2.81E-01 -2.42E-01 -2.01E-01 -1.54E-01 -1.08E-01 -6.06E-02…
-1.37E-02 3.32E-02 8.01E-02 1.27E-01 1.74E-01 2.21E-01 2.68E-01 3.15E-01…
3.61E-01 4.08E-01 4.61E-01 5.15E-01 5.69E-01 6.23E-01 6.77E-01 7.31E-01…
7.85E-01 8.39E-01 8.93E-01 9.46E-01 1.00E+00 1.05E+00 1.11E+00 1.94E+00…
2.00E+00 2.06E+00 2.12E+00 2.18E+00 2.24E+00 2.30E+00 2.36E+00 2.42E+00…
2.48E+00 2.54E+00 2.57E+00 2.58E+00 2.60E+00 2.61E+00 2.63E+00 2.64E+00…
2.66E+00 2.67E+00 2.67E+00 2.68E+00 2.69E+00 2.70E+00 2.71E+00 2.71E+00…
2.71E+00 2.70E+00 2.70E+00 2.69E+00 2.68E+00 2.67E+00 2.67E+00 2.65E+00…
2.64E+00 2.63E+00 2.62E+00 2.61E+00 2.60E+00 2.58E+00 2.57E+00 2.55E+00…

```
2.54E+00 2.53E+00 2.52E+00 2.50E+00 2.49E+00 2.48E+00 2.46E+00 2.45E+00…
2.43E+00 2.42E+00 2.40E+00 2.39E+00 2.37E+00 2.35E+00 2.34E+00 2.33E+00…
2.31E+00 2.30E+00 2.28E+00 2.26E+00 2.25E+00 2.23E+00 2.22E+00 2.20E+00…
2.18E+00 2.17E+00 2.15E+00 2.13E+00 2.11E+00 2.09E+00 2.08E+00 2.06E+00…
2.04E+00 2.03E+00 2.01E+00 2.00E+00 1.98E+00 1.96E+00 1.95E+00 1.93E+00…
1.91E+00 1.90E+00 1.88E+00 1.86E+00 1.85E+00 1.83E+00 1.82E+00 1.80E+00…
1.79E+00 1.77E+00 1.76E+00 1.74E+00 1.72E+00 1.71E+00 1.69E+00 1.68E+00…
1.66E+00 1.65E+00 1.64E+00 1.62E+00 1.61E+00 1.60E+00 1.59E+00 1.57E+00…
1.56E+00 1.55E+00 1.54E+00 1.52E+00 1.51E+00 1.50E+00 1.49E+00 1.47E+00];
plot(Z./0.355,V_polyax)
V_polyboth = [-2.52E-01…
-2.53E-01 -2.53E-01 -2.53E-01 -2.53E-01 -2.54E-01 -2.54E-01 -2.55E-01…
-2.55E-01 -2.56E-01 -2.56E-01 -2.57E-01 -2.58E-01 -2.58E-01 -2.59E-01…
-2.60E-01 -2.60E-01 -2.61E-01 -2.62E-01 -2.63E-01 -2.66E-01 -2.70E-01…
-2.74E-01 -2.77E-01 -2.82E-01 -2.87E-01 -2.92E-01 -2.98E-01 -3.03E-01…
-3.09E-01 -3.15E-01 -3.21E-01 -3.27E-01 -3.33E-01 -3.39E-01 -3.45E-01…
-3.52E-01 -3.59E-01 -3.70E-01 -3.81E-01 -3.92E-01 -4.03E-01 -4.14E-01…
-4.25E-01 -4.36E-01 -4.48E-01 -4.59E-01 -4.70E-01 -4.82E-01 -4.93E-01…
-5.05E-01 -5.17E-01 -5.28E-01 -5.40E-01 -5.53E-01 -5.67E-01 -5.82E-01…
-5.99E-01 -6.16E-01 -6.34E-01 -6.52E-01 -6.69E-01 -6.87E-01 -7.04E-01…
-7.21E-01 -7.39E-01 -7.56E-01 -7.73E-01 -7.91E-01 -8.08E-01 -8.25E-01…
-8.42E-01 -8.60E-01 -8.77E-01 -8.94E-01 -9.11E-01 -9.28E-01 -9.45E-01…
-9.62E-01 -9.81E-01 -1.00E+00 -1.02E+00 -1.04E+00 -1.06E+00 -1.09E+00…
-1.11E+00 -1.13E+00 -1.15E+00 -1.17E+00 -1.19E+00 -1.22E+00 -1.24E+00…
-1.26E+00 -1.28E+00 -1.30E+00 -1.33E+00 -1.35E+00 -1.37E+00 -1.39E+00…
-1.42E+00 -1.44E+00 -1.46E+00 -1.49E+00 -1.51E+00 -1.54E+00 -1.56E+00…
-1.59E+00 -1.62E+00 -1.64E+00 -1.67E+00 -1.69E+00 -1.72E+00 -1.75E+00…
-1.77E+00 -1.80E+00 -1.82E+00 -1.85E+00 -1.87E+00 -1.90E+00 -1.93E+00…
-1.95E+00 -1.98E+00 -2.01E+00 -2.04E+00 -2.07E+00 -2.10E+00 -2.13E+00…
-2.16E+00 -2.19E+00 -2.22E+00 -2.25E+00 -2.28E+00 -2.31E+00 -2.34E+00…
-2.37E+00 -2.40E+00 -2.43E+00 -2.46E+00 -2.49E+00 -2.52E+00 -2.56E+00…
-2.59E+00 -2.62E+00 -2.65E+00 -2.68E+00 -2.72E+00 -2.75E+00 -2.78E+00…
-2.81E+00 -2.84E+00 -2.87E+00 -2.90E+00 -2.93E+00 -2.96E+00 -2.99E+00…
-3.02E+00 -3.05E+00 -3.08E+00 -3.11E+00 -3.14E+00 -3.17E+00 -3.21E+00…
-3.24E+00 -3.27E+00 -3.30E+00 -3.33E+00 -3.36E+00 -3.40E+00 -3.43E+00…
-3.46E+00 -3.49E+00 -3.52E+00 -3.55E+00 -3.57E+00 -3.60E+00 -3.63E+00…
-3.66E+00 -3.69E+00 -3.72E+00 -3.74E+00 -3.77E+00 -3.80E+00 -3.83E+00…
-3.86E+00 -3.89E+00 -3.92E+00 -3.95E+00 -3.98E+00 -4.02E+00 -4.05E+00…
-4.08E+00 -4.11E+00 -4.15E+00 -4.18E+00 -4.21E+00 -4.24E+00 -4.27E+00…
-4.30E+00 -4.33E+00 -4.36E+00 -4.39E+00 -4.42E+00 -4.45E+00 -4.48E+00…
-4.52E+00 -4.55E+00 -4.58E+00 -4.61E+00 -4.64E+00 -4.67E+00 -4.70E+00…
-4.74E+00 -4.77E+00 -4.80E+00 -4.84E+00 -4.87E+00 -4.90E+00 -4.93E+00…
-4.96E+00 -4.99E+00 -5.02E+00 -5.06E+00 -5.09E+00 -5.12E+00 -5.15E+00…
-5.18E+00 -5.21E+00 -5.24E+00 -5.27E+00 -5.30E+00 -5.33E+00 -5.36E+00…
-5.39E+00 -5.42E+00 -5.45E+00 -5.48E+00 -5.51E+00 -5.54E+00 -5.57E+00…
-5.60E+00 -5.63E+00 -5.66E+00 -5.69E+00 -5.72E+00 -5.75E+00 -5.78E+00…
-5.81E+00 -5.84E+00 -5.87E+00 -5.90E+00 -5.93E+00 -5.97E+00 -6.00E+00…
-6.03E+00 -6.06E+00 -6.09E+00 -6.12E+00 -6.15E+00 -6.18E+00 -6.21E+00…
-6.24E+00 -6.27E+00 -6.30E+00 -6.32E+00 -6.35E+00 -6.38E+00 -6.41E+00…
-6.44E+00 -6.47E+00 -6.50E+00 -6.53E+00 -6.55E+00 -6.58E+00 -6.61E+00…
-6.64E+00 -6.66E+00 -6.69E+00 -6.72E+00 -6.75E+00 -6.78E+00 -6.80E+00…
-6.83E+00 -6.86E+00 -6.89E+00 -6.91E+00 -6.94E+00 -6.97E+00 -6.99E+00…
-7.02E+00 -7.05E+00 -7.08E+00 -7.11E+00 -7.14E+00 -7.17E+00 -7.20E+00…
-7.22E+00 -7.25E+00 -7.28E+00 -7.31E+00 -7.34E+00 -7.37E+00 -7.39E+00…
```

-7.42E+00 -7.45E+00 -7.47E+00 -7.50E+00 -7.52E+00 -7.54E+00 -7.57E+00…
-7.59E+00 -7.61E+00 -7.64E+00 -7.66E+00 -7.68E+00 -7.71E+00 -7.73E+00…
-7.75E+00 -7.77E+00 -7.80E+00 -7.82E+00 -7.84E+00 -7.86E+00 -7.88E+00…
-7.91E+00 -7.93E+00 -7.95E+00 -7.98E+00 -8.00E+00 -8.02E+00 -8.05E+00…
-8.07E+00 -8.09E+00 -8.11E+00 -8.13E+00 -8.15E+00 -8.17E+00 -8.19E+00…
-8.21E+00 -8.23E+00 -8.25E+00 -8.27E+00 -8.29E+00 -8.31E+00 -8.33E+00…
-8.35E+00 -8.37E+00 -8.39E+00 -8.41E+00 -8.43E+00 -8.45E+00 -8.47E+00…
-8.48E+00 -8.50E+00 -8.52E+00 -8.54E+00 -8.56E+00 -8.57E+00 -8.59E+00…
-8.61E+00 -8.62E+00 -8.64E+00 -8.66E+00 -8.67E+00 -8.69E+00 -8.71E+00…
-8.72E+00 -8.74E+00 -8.76E+00 -8.77E+00 -8.79E+00 -8.80E+00 -8.82E+00…
-8.83E+00 -8.85E+00 -8.86E+00 -8.88E+00 -8.89E+00 -8.90E+00 -8.92E+00…
-8.93E+00 -8.94E+00 -8.96E+00 -8.97E+00 -8.99E+00 -9.00E+00 -9.01E+00…
-9.02E+00 -9.04E+00 -9.05E+00 -9.06E+00 -9.07E+00 -9.09E+00 -9.10E+00…
-9.11E+00 -9.12E+00 -9.13E+00 -9.14E+00 -9.15E+00 -9.16E+00 -9.17E+00…
-9.18E+00 -9.19E+00 -9.20E+00 -9.21E+00 -9.22E+00 -9.23E+00 -9.24E+00…
-9.25E+00 -9.26E+00 -9.27E+00 -9.28E+00 -9.29E+00 -9.29E+00 -9.30E+00…
-9.31E+00 -9.32E+00 -9.33E+00 -9.34E+00 -9.34E+00 -9.35E+00 -9.36E+00…
-9.36E+00 -9.37E+00 -9.38E+00 -9.39E+00 -9.39E+00 -9.40E+00 -9.40E+00…
-9.41E+00 -9.41E+00 -9.42E+00 -9.42E+00 -9.43E+00 -9.44E+00 -9.44E+00…
-9.44E+00 -9.45E+00 -9.45E+00 -9.46E+00 -9.46E+00 -9.46E+00 -9.47E+00…
-9.47E+00 -9.47E+00 -9.48E+00 -9.48E+00 -9.48E+00 -9.48E+00 -9.49E+00…
-9.49E+00 -9.49E+00 -9.49E+00 -9.49E+00 -9.49E+00 -9.49E+00 -9.50E+00…
-9.50E+00 -9.50E+00 -9.50E+00 -9.50E+00 -9.50E+00 -9.50E+00 -9.50E+00…
-9.50E+00 -9.50E+00 -9.49E+00 -9.49E+00 -9.49E+00 -9.49E+00 -9.49E+00…
-9.49E+00 -9.48E+00 -9.48E+00 -9.48E+00 -9.47E+00 -9.47E+00 -9.47E+00…
-9.47E+00 -9.46E+00 -9.46E+00 -9.45E+00 -9.45E+00 -9.45E+00 -9.44E+00…
-9.44E+00 -9.43E+00 -9.43E+00 -9.42E+00 -9.42E+00 -9.41E+00 -9.40E+00…
-9.40E+00 -9.39E+00 -9.39E+00 -9.38E+00 -9.37E+00 -9.37E+00 -9.36E+00…
-9.35E+00 -9.34E+00 -9.34E+00 -9.33E+00 -9.32E+00 -9.32E+00 -9.31E+00…
-9.30E+00 -9.29E+00 -9.28E+00 -9.27E+00 -9.26E+00 -9.25E+00 -9.24E+00…
-9.24E+00 -9.23E+00 -9.22E+00 -9.21E+00 -9.19E+00 -9.18E+00 -9.17E+00…
-9.16E+00 -9.15E+00 -9.14E+00 -9.13E+00 -9.12E+00 -9.11E+00 -9.10E+00…
-9.08E+00 -9.07E+00 -9.06E+00 -9.05E+00 -9.03E+00 -9.02E+00 -9.01E+00…
-8.99E+00 -8.98E+00 -8.96E+00 -8.95E+00 -8.93E+00 -8.92E+00 -8.90E+00…
-8.89E+00 -8.87E+00 -8.85E+00 -8.84E+00 -8.82E+00 -8.81E+00 -8.79E+00…
-8.78E+00 -8.76E+00 -8.75E+00 -8.73E+00 -8.71E+00 -8.70E+00 -8.68E+00…
-8.67E+00 -8.65E+00 -8.64E+00 -8.62E+00 -8.60E+00 -8.59E+00 -8.57E+00…
-8.55E+00 -8.54E+00 -8.52E+00 -8.50E+00 -8.49E+00 -8.47E+00 -8.45E+00…
-8.43E+00 -8.42E+00 -8.40E+00 -8.38E+00 -8.36E+00 -8.34E+00 -8.33E+00…
-8.31E+00 -8.29E+00 -8.27E+00 -8.25E+00 -8.23E+00 -8.21E+00 -8.19E+00…
-8.17E+00 -8.15E+00 -8.13E+00 -8.11E+00 -8.09E+00 -8.07E+00 -8.05E+00…
-8.03E+00 -8.01E+00 -7.99E+00 -7.97E+00 -7.95E+00 -7.93E+00 -7.90E+00…
-7.88E+00 -7.86E+00 -7.84E+00 -7.81E+00 -7.79E+00 -7.77E+00 -7.75E+00…
-7.73E+00 -7.70E+00 -7.68E+00 -7.66E+00 -7.63E+00 -7.61E+00 -7.59E+00…
-7.56E+00 -7.54E+00 -7.51E+00 -7.49E+00 -7.47E+00 -7.44E+00 -7.42E+00…
-7.39E+00 -7.37E+00 -7.34E+00 -7.32E+00 -7.29E+00 -7.27E+00 -7.24E+00…
-7.22E+00 -7.19E+00 -7.17E+00 -7.14E+00 -7.11E+00 -7.09E+00 -7.06E+00…
-7.03E+00 -7.01E+00 -6.98E+00 -6.96E+00 -6.93E+00 -6.90E+00 -6.87E+00…
-6.85E+00 -6.82E+00 -6.79E+00 -6.76E+00 -6.74E+00 -6.71E+00 -6.68E+00…
-6.65E+00 -6.63E+00 -6.60E+00 -6.57E+00 -6.54E+00 -6.51E+00 -6.48E+00…
-6.45E+00 -6.42E+00 -6.40E+00 -6.37E+00 -6.34E+00 -6.31E+00 -6.28E+00…
-6.25E+00 -6.22E+00 -6.19E+00 -6.16E+00 -6.13E+00 -6.10E+00 -6.07E+00…
-6.04E+00 -6.01E+00 -5.98E+00 -5.95E+00 -5.92E+00 -5.89E+00 -5.86E+00…
-5.83E+00 -5.80E+00 -5.77E+00 -5.74E+00 -5.71E+00 -5.67E+00 -5.64E+00…

```
-5.61E+00 -5.58E+00 -5.55E+00 -5.52E+00 -5.49E+00 -5.46E+00 -5.43E+00…
-5.40E+00 -5.36E+00 -5.33E+00 -5.30E+00 -5.27E+00 -5.24E+00 -5.21E+00…
-5.17E+00 -5.14E+00 -5.11E+00 -5.08E+00 -5.05E+00 -5.02E+00 -4.98E+00…
-4.95E+00 -4.92E+00 -4.89E+00 -4.86E+00 -4.83E+00 -4.79E+00 -4.76E+00…
-4.73E+00 -4.70E+00 -4.67E+00 -4.63E+00 -4.60E+00 -4.57E+00 -4.54E+00…
-4.50E+00 -4.47E+00 -4.44E+00 -4.41E+00 -4.38E+00 -4.34E+00 -4.31E+00…
-4.28E+00 -4.25E+00 -4.21E+00 -4.18E+00 -4.15E+00 -4.12E+00 -4.08E+00…
-4.05E+00 -4.02E+00 -3.99E+00 -3.95E+00 -3.92E+00 -3.89E+00 -3.86E+00…
-3.82E+00 -3.79E+00 -3.76E+00 -3.73E+00 -3.69E+00 -3.66E+00 -3.63E+00…
-3.59E+00 -3.56E+00 -3.53E+00 -3.50E+00 -3.46E+00 -3.43E+00 -3.40E+00…
-3.36E+00 -3.33E+00 -3.30E+00 -3.27E+00 -3.23E+00 -3.20E+00 -3.17E+00…
-3.13E+00 -3.10E+00 -3.07E+00 -3.03E+00 -3.00E+00 -2.97E+00 -2.93E+00…
-2.90E+00 -2.87E+00 -2.84E+00 -2.80E+00 -2.77E+00 -2.74E+00 -2.70E+00…
-2.67E+00 -2.64E+00 -2.60E+00 -2.57E+00 -2.54E+00 -2.50E+00 -2.47E+00…
-2.44E+00 -2.40E+00 -2.37E+00 -2.34E+00 -2.30E+00 -2.27E+00 -2.24E+00…
-2.20E+00 -2.17E+00 -2.14E+00 -2.11E+00 -2.07E+00 -2.04E+00 -2.01E+00…
-1.97E+00 -1.94E+00 -1.91E+00 -1.87E+00 -1.84E+00 -1.81E+00 -1.78E+00…
-1.74E+00 -1.71E+00 -1.68E+00 -1.65E+00 -1.61E+00 -1.58E+00 -1.55E+00…
-1.52E+00 -1.48E+00 -1.45E+00 -1.42E+00 -1.39E+00 -1.36E+00 -1.32E+00…
-1.29E+00 -1.26E+00 -1.23E+00 -1.20E+00 -1.16E+00 -1.13E+00 -1.10E+00…
-1.07E+00 -1.04E+00 -1.00E+00 -9.71E-01 -9.38E-01 -9.06E-01 -8.73E-01…
-8.40E-01 -8.08E-01 -7.75E-01 -7.43E-01 -7.10E-01 -6.77E-01 -6.45E-01…
-6.11E-01 -5.76E-01 -5.41E-01 -5.05E-01 -4.70E-01 -4.35E-01 -4.00E-01…
-3.65E-01 -3.30E-01 -2.95E-01 -2.60E-01 -2.25E-01 -1.90E-01 -1.52E-01…
-1.12E-01 -7.17E-02 -3.15E-02 8.72E-03 4.89E-02 8.91E-02 1.29E-01 1.70E-01…
2.10E-01 2.50E-01 2.90E-01 3.30E-01 3.73E-01 4.22E-01 4.72E-01 5.21E-01…
5.71E-01 6.20E-01 6.70E-01 7.20E-01 7.69E-01 8.19E-01 8.68E-01 9.18E-01…
9.67E-01 1.02E+00 1.08E+00 1.15E+00 1.22E+00 1.28E+00 1.35E+00 1.42E+00…
1.48E+00 1.55E+00 1.62E+00 1.69E+00 1.75E+00 1.82E+00 1.89E+00 3.45E+00…
3.52E+00 3.59E+00 3.65E+00 3.72E+00 3.78E+00 3.85E+00 3.91E+00 3.98E+00…
4.05E+00 4.11E+00 4.12E+00 4.12E+00 4.12E+00 4.11E+00 4.11E+00 4.11E+00…
4.11E+00 4.09E+00 4.08E+00 4.06E+00 4.05E+00 4.04E+00 4.03E+00 4.00E+00…
3.97E+00 3.93E+00  3.90E+003.86E+00 3.82E+00 3.78E+00 3.74E+00 3.70E+00…
3.66E+00 3.62E+00 3.58E+00 3.54E+00 3.50E+00 3.46E+00 3.41E+00 3.36E+00…
3.31E+00 3.28E+00 3.24E+00 3.21E+00 3.17E+00 3.13E+00 3.09E+00 3.05E+00…
3.01E+00 2.98E+00 2.93E+00 2.89E+00 2.85E+00 2.81E+00 2.77E+00 2.74E+00…
2.71E+00 2.68E+00 2.64E+00 2.60E+00 2.57E+00 2.54E+00 2.51E+00 2.47E+00…
2.44E+00 2.40E+00 2.37E+00 2.33E+00 2.30E+00 2.26E+00 2.23E+00 2.20E+00…
2.17E+00 2.15E+00 2.12E+00 2.09E+00 2.07E+00 2.04E+00 2.01E+00 1.98E+00…
1.96E+00 1.93E+00 1.90E+00 1.87E+00 1.85E+00 1.82E+00 1.80E+00 1.78E+00…
1.76E+00 1.74E+00 1.72E+00 1.69E+00 1.67E+00 1.65E+00 1.63E+00 1.61E+00…
1.59E+00 1.58E+00 1.56E+00 1.55E+00 1.53E+00 1.52E+00 1.51E+00 1.49E+00…
1.48E+00 1.47E+00 1.45E+00 1.44E+00 1.43E+00 1.41E+00 1.40E+00 1.39E+00];
plot(Z./0.355,V_polyboth)
V = -[0 0.3305 3.0053 5.8715 6.3791 6.7719 6.9083 6.5300 5.7802 4.8422...
    4.0899 1.0697 0]';
X = [0 0.035 0.07 0.105 0.14 0.175 0.21 0.245 0.28 0.315 0.3325 0.35...
   0.355]'./0.355;
plot(X,V,'k+--')
legend('Uniform','Poly Axial','Poly Axial & Radial','CFX Propeller Data',...
      'Location','northwest')
annotation(figure(4),'textbox',...
   [0.392071428571429 0.4 0.132928571428571 0.059523809523811],...
   'String',{'Peak Shift'},...
```

```
    'FitBoxToText','off');
annotation(figure(4),'arrow',[0.460714285714286 0.480357142857143],...
    [0.397619047619048 0.15]);
annotation(figure(4),'textbox',...
    [0.43 0.678571428571429 0.23 0.0642857142857155],...
    'String',{'Edge Discontinuity'},...
    'FitBoxToText','off');
annotation(figure(4),'arrow',[0.660714285714286 0.8125],...
    [0.703761904761905 0.735714285714286]);
```

APPENDIX F. COTS PLATFORM ANSYS REPORT

The settings and parameters used in the COTS platform modeling are provided below.

Date
2022/05/10 12:08:55

IX. Contents

X. 1. File Report

Table 1. File Information for CFX

Case	CFX
File Path	C:\Users\zachary.ceroli\Documents\Ceroli\Ansys\Hexacopter Hover_files\dp0\CFX\CFX\Fluid Flow CFX_002.res
File Date	08 May 2022
File Time	11:07:38 PM
File Type	CFX5
File Version	21.2

XI. 2. Mesh Report

Table 2. Mesh Information for CFX

Domain	Nodes	Elements
Default Domain	11090090	62622788

XII. 3. Physics Report

Table 3. Domain Physics for CFX

Domain - Default Domain

Type	Fluid
Location	Center Act, Fluid Volume, Left Act, Right Act
Materials	
Air at 25 C	
Fluid Definition	Material Library

Morphology	Continuous Fluid
Settings	
Buoyancy Model	Non Buoyant
Domain Motion	Stationary
Reference Pressure	1.0000e+0 [atm]
Heat Transfer Model	Isothermal
Fluid Temperature	2.5000e+1 [C]
Turbulence Model	SST
Turbulent Wall Functions	Automatic
Domain Interface - Default Fluid Fluid Interface	
Boundary List1	Default Fluid Fluid Interface Side 1
Boundary List2	Default Fluid Fluid Interface Side 2
Interface Type	Fluid Fluid
Settings	
Interface Models	General Connection
Mass And Momentum	Conservative Interface Flux
Mesh Connection	Automatic

Table 4. Boundary Physics for CFX

Domain	Boundaries
Default Domain	Boundary - Default Fluid Fluid Interface Side 1
Type	INTERFACE
Location	Center Act Bottom, Center Act Cyl, Left Act Bottom, Left Act Cyl, Right Act Bottom, Right Act Cyl
Settings	
Mass And Momentum	Conservative Interface Flux
Turbulence	Conservative Interface Flux
Boundary - Default Fluid Fluid Interface Side 2	
Type	INTERFACE
Location	Center Cyl, Center Cyl Bottom, Left Cyl, Left Cyl Bottom, Right Cyl, Right Cyl Bottom
Settings	
Mass And Momentum	Conservative Interface Flux
Turbulence	Conservative Interface Flux
Boundary - Center Disk	
Type	OPENING
Location	Upper Center Disk, Lower Center Disk
Settings	
Flow Regime	Subsonic
Mass And Momentum	Cylindrical Velocity Components
Velocity Axial Component	-ViC
Velocity Theta Component	0.0000e+0 [m s^-1]
Velocity r Component	-ViC*RadC/Ro
Axis Definition	Coordinate Axis

Rotation Axis Center.3
Turbulence Medium Intensity and Eddy Viscosity Ratio
Boundary - Left
Type OPENING
Location Left
Settings
Flow Regime Subsonic
Mass And Momentum Entrainment
Relative Pressure 0.0000e+0 [Pa]
Turbulence Medium Intensity and Eddy Viscosity Ratio
Boundary - Left Disk
Type OPENING
Location Lower Left Disk, Upper Left Disk
Settings
Flow Regime Subsonic
Mass And Momentum Cylindrical Velocity Components
Velocity Axial Component -ViL
Velocity Theta Component 0.0000e+0 [m s^-1]
Velocity r Component -ViL*RadL/Ro
Axis Definition Coordinate Axis
Rotation Axis Left.3
Turbulence Medium Intensity and Eddy Viscosity Ratio
Boundary - Openings
Type OPENING
Location Back, Bottom, Right
Settings
Flow Regime Subsonic
Mass And Momentum Entrainment
Relative Pressure 0.0000e+0 [Pa]
Turbulence Medium Intensity and Eddy Viscosity Ratio
Boundary - Right Disk
Type OPENING
Location Lower Right Disk, Upper Right Disk
Settings
Flow Regime Subsonic
Mass And Momentum Cylindrical Velocity Components
Velocity Axial Component -ViR
Velocity Theta Component 0.0000e+0 [m s^-1]
Velocity r Component -ViR*RadR/Ro
Axis Definition Coordinate Axis
Rotation Axis Right.3
Turbulence Medium Intensity and Eddy Viscosity Ratio
Boundary - Top
Type OPENING
Location Top

Settings
Flow Regime Subsonic
Mass And Momentum Entrainment
Relative Pressure 0.0000e+0 [Pa]
Turbulence Medium Intensity and Eddy Viscosity Ratio
Boundary - Symmetry
Type SYMMETRY
Location Symmetry
Settings
Boundary - Wall
Type WALL
Location Wall
Settings
Mass And Momentum No Slip Wall
Wall Roughness Smooth Wall

XIII. 4. User Data

APPENDIX G. FLYING WING ANSYS REPORT

The settings and parameters used in the Flying Wing modeling are provided below.

Date
2022/05/10 12:13:34

IX. Contents

X. 1. File Report

Table 1. File Information for CFX

Case	CFX
File Path	C:\Users\zachary.ceroli\Documents\Ceroli\Ansys\Airfoil Hover_files\dp0\CFX\CFX\Fluid Flow CFX_004.res
File Date	09 May 2022
File Time	11:50:57 AM
File Type	CFX5
File Version	21.2

XI. 2. Mesh Report

Table 2. Mesh Information for CFX

Domain	Nodes	Elements
Default Domain	14927885	65898330

XII. 3. Physics Report

Table 3. Domain Physics for CFX

Domain - Default Domain

Type	Fluid
Location	Center Act, Fluid Volume, Left Act, Right Act
Materials	
Air at 25 C	
Fluid Definition	Material Library
Morphology	Continuous Fluid
Settings	

Buoyancy Model Non Buoyant
Domain Motion Stationary
Reference Pressure 1.0000e+0 [atm]
Heat Transfer Model Isothermal
Fluid Temperature 2.5000e+1 [C]
Turbulence Model SST
Turbulent Wall Functions Automatic
Domain Interface - Default Fluid Fluid Interface
Boundary List1 Default Fluid Fluid Interface Side 1
Boundary List2 Default Fluid Fluid Interface Side 2
Interface Type Fluid Fluid
Settings
Interface Models General Connection
Mass And Momentum Conservative Interface Flux
Mesh Connection Automatic

Table 4. Boundary Physics for CFX
Domain Boundaries
Default Domain Boundary - Default Fluid Fluid Interface Side 1
Type INTERFACE
Location Center Act Bottom, Center Act Cyl, Left Act Bottom, Left Act Cyl, Right Act Bottom, Right Act Cyl
Settings
Mass And Momentum Conservative Interface Flux
Turbulence Conservative Interface Flux
Boundary - Default Fluid Fluid Interface Side 2
Type INTERFACE
Location Center Bottom, Center Cyl, Left Bottom, Left Cyl, Right Bottom, Right Cyl
Settings
Mass And Momentum Conservative Interface Flux
Turbulence Conservative Interface Flux
Boundary - Center Disk
Type OPENING
Location Center Disk, Center Act Disk
Settings
Flow Regime Subsonic
Mass And Momentum Cylindrical Velocity Components
Velocity Axial Component -ViC
Velocity Theta Component 0.0000e+0 [m s^-1]
Velocity r Component -ViC*RadC/Ro
Axis Definition Coordinate Axis
Rotation Axis Center.3
Turbulence Medium Intensity and Eddy Viscosity Ratio

Boundary - Left
Type OPENING
Location Left
Settings
Flow Regime Subsonic
Mass And Momentum Entrainment
Relative Pressure 0.0000e+0 [Pa]
Turbulence Zero Gradient
Boundary - Left Disk
Type OPENING
Location Left Disk, Left Act Disk
Settings
Flow Regime Subsonic
Mass And Momentum Cylindrical Velocity Components
Velocity Axial Component -ViL
Velocity Theta Component 0.0000e+0 [m s^-1]
Velocity r Component -ViL*RadL/Ro
Axis Definition Coordinate Axis
Rotation Axis Left.3
Turbulence Medium Intensity and Eddy Viscosity Ratio
Boundary - Openings
Type OPENING
Location Back, Bottom, Right
Settings
Flow Regime Subsonic
Mass And Momentum Entrainment
Relative Pressure 0.0000e+0 [Pa]
Turbulence Zero Gradient
Boundary - Right Disk
Type OPENING
Location Right Disk, Right Act Disk
Settings
Flow Regime Subsonic
Mass And Momentum Cylindrical Velocity Components
Velocity Axial Component -ViR
Velocity Theta Component 0.0000e+0 [m s^-1]
Velocity r Component -ViR*RadR/Ro
Axis Definition Coordinate Axis
Rotation Axis Right.3
Turbulence Medium Intensity and Eddy Viscosity Ratio
Boundary - Top
Type OPENING
Location Top
Settings
Flow Regime Subsonic

Mass And Momentum Entrainment
Relative Pressure 0.0000e+0 [Pa]
Turbulence Zero Gradient
Boundary - Symmetry
Type SYMMETRY
Location Symmetry
Settings
Boundary - Default Domain Default
Type WALL
Location F34.158, F740.866, F895.1015
Settings
Mass And Momentum No Slip Wall
Wall Roughness Smooth Wall
Boundary - Wall
Type WALL
Location Wall
Settings
Mass And Momentum No Slip Wall
Wall Roughness Smooth Wall

XIII. 4. User Data

APPENDIX H. FORWARD FLIGHT THRUST MATLAB CODE

Below is the CFD predicted thrust from the various forward flight test cases of both platforms and the graphing code used.

```
%% Forward Flight
clear
clc
% X-Axis Variable
Airspeed = [0 2 4 8 15];
% COTS Lift and Drag
COTS_Lift = [0 0.05 0.19 0.17 -5.28];
COTS_Drag = [0 0.17 0.63 2.62 12.4];
COTS_Lift_Rotor = [-0.06 -3.57 -2.95 -2.08 -11.7];
COTS_Drag_Rotor = [4.62 0.22 0.78 1.69 11.6];
figure(5)
plot(Airspeed,COTS_Lift,'b+--',Airspeed,COTS_Lift_Rotor,'bd--')
xlabel('Airspeed [m/s]')
ylabel('Lift [N]')
legend('No Actuator Disks Lift','Actuator Disks Lift')
figure(6)
plot(Airspeed,COTS_Drag,'r+--',Airspeed,COTS_Drag_Rotor,'rd--')
xlabel('Airspeed [m/s]')
ylabel('Drag [N]')
legend('No Actuator Disks Drag','Actuator Disks Drag','Location','northwest')
% Wing Lift and Drag
Wing_Lift = [0 0.54 0.34 7.35 41.9];
Wing_Drag = [0 0.40 1.46 6.91 40.0];
Wing_Lift_Rotor = [-0.03 -0.01 -0.54 2.04 26.4];
Wing_Drag_Rotor = [4.47 2.21 7.68 26.4 81.2];
figure(7)
plot(Airspeed,Wing_Lift,'b+--',Airspeed,Wing_Lift_Rotor,'bd--')
xlabel('Airspeed [m/s]')
ylabel('Lift [N]')
legend('No Actuator Disks Lift','Actuator Disks Lift','Location','northwest')
figure(8)
plot(Airspeed,Wing_Drag,'r+--',Airspeed,Wing_Drag_Rotor,'rd--')
xlabel('Airspeed [m/s]')
ylabel('Drag [N]')
legend('No Actuator Disks Drag','Actuator Disks Drag','Location','northwest')
% COTS CFD Predicted Thrust Results
COTS_Tot_Thrust = [85.5 84.3 83.1 80.1 85.8];
COTS_Disk_Thrust = [28.5 28.1 27.7 26.7 28.6];
figure(9)
yyaxis left
plot(Airspeed,COTS_Tot_Thrust,'k+--')
xlabel('Airspeed [m/s]')
ylabel('Total Thrust [N]')
yyaxis right
plot(Airspeed,COTS_Disk_Thrust,'k+--')
```

```
ylabel('Thrust per Disk [N]')
axis([0 16 80/3 86/3])
% Flying Wing CFD Predicted Thrust Results
Wing_Tot_Thrust = [85.5 23.6 18.9 47.1 97.5];
Wing_Disk_Thrust = [28.5 7.86 6.31 15.7 32.5];
figure(10)
yyaxis left
plot(Airspeed,Wing_Tot_Thrust, 'k+--')
xlabel('Airspeed [m/s]')
ylabel('Total Thrust [N]')
yyaxis right
plot(Airspeed,Wing_Disk_Thrust,'k+--')
ylabel('Thrust per Disk [N]')
axis([0 16 10/3 100/3])
% Comparisons
figure(11)
plot(Airspeed,COTS_Disk_Thrust,'k+--',Airspeed,Wing_Disk_Thrust,'r+--')
xlabel('Airspeed [m/s]')
ylabel('Thrust per Disk [N]')
legend('COTS Platform','Flying Wing','Location','northwest')
figure(12)
plot(Airspeed,COTS_Lift,'k+--',Airspeed,Wing_Lift,'r+--')
xlabel('Airspeed [m/s]')
ylabel('External Flow Lift Force [N]')
legend('COTS Platform','FLying Wing','Location','northwest')
figure(13)
plot(Airspeed,COTS_Lift_Rotor,'k+--',Airspeed,Wing_Lift_Rotor,'r+--')
xlabel('Airspeed [m/s]')
ylabel('External and Actuator Flows Lift Force [N]')
legend('COTS Platform','Flying Wing','Location','northwest')
figure(14)
plot(Airspeed,COTS_Drag,'k+--',Airspeed,Wing_Drag,'r+--')
xlabel('Airspeed [m/s]')
ylabel('External Flow Drag Force [N]')
legend('COTS Platform','Flying Wing','Location','northwest')
figure(15)
plot(Airspeed,COTS_Drag_Rotor,'k+--',Airspeed,Wing_Drag_Rotor,'r+--')
xlabel('Airspeed [m/s]')
ylabel('External and Actuator Flows Drag Force [N]')
legend('COTS Platform','Flying Wing','Location','northwest')
```

LIST OF REFERENCES

[1] George, R., 5 February 2015, "Defense Department Energy Use Falls to Lowest Level Since at Least 1975," U.S. Energy Information Administration, accessed October 2021, Available: https://www.eia.gov/todayinenergy/detail.php?id=19871..

[2] Ciaravino, J. S., 2003, "Study of Hydrogen as an Aircraft Fuel," Master's Thesis, Naval Postgraduate School, Monterey, CA.

[3] Anderson, B. R., 2019, "Renewable Hydrogen Production, Compression, and Storage Autonomous System," Master's Thesis, Naval Postgraduate School, Monterey, CA.

[4] Hardt, E. J., 2021, "Hydrogen Fuel Operation for Gas Turbine Engines," Master's Thesis, Naval Postgraduate School, Monterey, CA.

[5] Fosson, E. A., 2017, "Design and Analysis of a Hydrogen Compression and Storage Station," Master's Thesis, Naval Postgraduate School, Monterey, CA.

[6] HES Energy Systems, 07 November 2019, "Navy Accepts First-of-its-kind Hydrogen Powered UAS.," accessed October 2021, Available: https://www.hes.sg/nps..

[7] HES Energy Solutions, 08 November 2018, "Hycopter Long Endurance Hydrogen Electric Drone," accessed December 2021, Available: https://www.hes.sg/_files/ugd/3029f7_9e97b045de0e4c5b9790a63a46a2bb28.pdf.

[8] Yang, S., 2020 "Study of the Power Required for Flight of the Aqua-Quad (Solar-Powered Quad-Rotor Unmanned Aerial System)," Master's Thesis, Naval Postgraduate School, Monterey, CA.

[9] Gossett, D. H., 2000, "Investigation of cross flow fan propulsion for lightweight VTOL aircraft," Master's Thesis, Naval Postgraduate School, Monterey, CA.

[10] Kohlman, D, 1981, *Introduction To V/STOL Airplanes*, Iowa State University Press, Ames, IA.

[11] Campbell, J., 1962, *Aircraft*, The MacMillan Company, New York, NY.

[12] Schneider, J., 1984, *Rotary-Wing V/STOL: Development of the Tiltrotor*, Smithsonian Institution Press, Washington, D.C.,

[13] O'Brien, M. A., 1992, "The V-22 Osprey: a case analysis," Master's Thesis, Naval Postgraduate School, Monterey, CA.

[14] Taylor, W. E., 1996, "Civil tiltrotor (CTR) applications: a dependence on Defense development and procurement of the MV-22 Osprey," Master's Thesis, Naval Postgraduate School, Monterey, CA.

[15] Mislick, G. K., 1988, "A comparative analysis of tilt rotor aircraft versus helicopters using simulator results.," Master's Thesis, Naval Postgraduate School, Monterey, CA.

[16] Johnson, W., 1980, "Vertical Flight I," *Helicopter Theory*, Princeton University Press, Princeton, NJ.

[17] Princeton University, 02 March 2022 "Bernoulli's Equation," Princeton University Press, accessed March 2022, Available: https://www.princeton.edu/~asmits/Bicycle_web/Bernoulli.html.

[18] Johnson, W., 1980, "Forward Flight I," *Helicopter Theory*, Princeton University Press, Princeton, NJ.

[19] Richmond, A. K., 2022, "Numerical Modeling of Fluid Behavior Around a Hovering Drone Rotor," Master's Thesis, Naval Postgraduate School, Monterey, CA.

[20] National Aeronautics and Space Administration, 13 May 2021, "Shape Effects on Drag," accessed Jan 2022, Available: https://www.grc.nasa.gov/WWW/k-12/airplane/shaped.html.

[21] Sogukpinar, H., 2017, "Numerical Simulation of 4-Digit Inclined NACA 00XX Airfoils to Find Optimum Angle of Attack for Airplane Wing," *Uludag University Journal of the Faculty of Engineering,* vol. 22, no. 1, pp. 169–178, Bursa, Turkey.

[22] UIUC Applied Aerodynamics Group, 01 January 2022, "UIUC Airfoil Coordinates Database," University of Illinois at Urbana-Champaign, accessed March 2022, Available: https://m-selig.ae.illinois.edu/ads/coord_database.html.

INITIAL DISTRIBUTION LIST

1. Defense Technical Information Center
   Ft. Belvoir, Virginia

2. Dudley Knox Library
   Naval Postgraduate School
   Monterey, California